FERROMAGNET/SEMICONDUCTOR BASED SPINTRONIC DEVICES

by

Dipankar Saha

A dissertation submitted in partial fulfillment
of the requirements for the degree of
Doctor of Philosophy
(Electrical Engineering)
in The University of Michigan
2009

Doctoral Committee:

Professor Pallab Bhattacharya, Chair
Professor Roberto Merlin
Professor Jasprit Singh
Assistant Professor Wei Lu

© Dipankar Saha 2009
All Rights Reserved

To my parents, Lakshman Saha and Bina Saha

ACKNOWLEDGEMENTS

I am grateful to numerous people for their support and contributions. This journey would not have been possible without their constant help and encouragements. First, I would like thank my advisor Prof. Pallab Bhattacharya, who remains a constant source of inspiration throughout my work. His persistent efforts to look for new things and achieve new heights have motivated me to do a lot of things which were otherwise impossible. His constant encouragements have kept me going and have helped me to keep focus without losing sight during the times of failure. I have learnt a great many things which have helped me to build character, which will be of great use in my future endeavors. I am also grateful to my other committee members – Prof. Roberto Merlin, Prof. Jasprit Singh, and Prof. Wei Lu – for contributing their time and providing insightful suggestions and comments to improve the quality of this work.

I would like to express my deep gratitude to my mentor Dr. Michael Holub. He has been very helpful from the very first day of my research work. His help has been instrumental in many of the achievements described in this thesis. I am very thankful to Debashish Basu for his constant support during the latter part of my work. Both Dr. Michael Holub and Debashish Basu have provided me with immense moral support all through my work. They also grew all the samples using MBE for my work. I would also like to thank Dr. Swapnajit Chakravarty and Dr. Jonghyun Shin for helping me with the learning of device fabrication and very helpful discussions.

This thesis has been greatly enhanced by the collaborative efforts of researchers with Purdue University. Prof. Supriyo Datta and his students, Dr. Sayeef Salahuddin and Lutfe Siddiqui deserve special thanks for their insights toward the realization of the MnAs/GaAs spin-valve and the spin capacitor. There are many other graduate students with whom I may not have collaborated directly but whose assistance and mentorship is appreciated. I thank Dr. Xiaohua Su, Dr. Zetian Mi, Dr. Jun Yang, Zhung Wu, Guan Huang, Chung Chiang Wu, Jeremy Moore, Meng Zhang, Wei Guo, Junseok Huo, Chi-sen Lee, Hyun Kum, Emine Cagin, Willie Bowen, Yu-Ching Liao and Weiming Wang for their support.

Many data presented in this thesis was acquired using equipment from other faculty members. This thesis would not have been possible without their generosity. I would like to acknowledge Dr. Chris Kojiro for his help with the Quantum Design SQUID magnetometer located in the Department of Chemistry. Prof. Roberto Merlin and his graduate student, Paul Jacobs, deserve my thanks for use of and assistance with their magneto-optical cryostat, which was vital to the characterization of the spin-polarized VCSELs.

The excellent technical support of the Michigan Nanofabrication Facility staff is also greatly appreciated. My special thanks to Edward Tang, Dennis Schweiger, Gregory Allion, and Brian VanDerElzen for their immense help with the device fabrication and characterization tools. I thank Judi Scramlin, Melanie Caughey, Lisa Vogel, Denise Oscar, Susan Abraham, Laura Jarels, Gary Huskey, Deb Swartz, Frances Doman, Nadine Wang, and Beth Stalnaker for administrative support throughout my graduate career. I wish to acknowledge the Department of Electrical Engineering and Computer Science, University of Michigan Rackham Graduate School for providing fellowships and Prof. Pallab Bhattacharya to support my graduate education, and

the Office of Naval Research and Army Research for funding this research.

Finally, I could not have completed this work without constant encouragement from my friends and family. I am grateful for the love and support of my parents, Lakshman and Bina Saha, and my sisters, Aparna and Suparna Saha, and my brother, Ranajit Saha. Special thanks is owed to Dipanjan Basu, Priyanka Dutta, Mosin Mondal, Ayan Paul, Sarbani Ray, and Ananda Sankar Roy for their love, encouragement, and friendship.

TABLE OF CONTENTS

DEDICATION ii

ACKNOWLEDGEMENTS iii

LIST OF FIGURES ix

LIST OF TABLES xvi

LIST OF APPENDICES xvii

LIST OF ACRONYMS xviii

ABSTRACT xx

CHAPTER

I. Introduction 1

1.1 Beyond Moore's Law 1
1.2 Spintronics 3
1.2.1 Magnetic Tunnel Junctions and Tunneling Magnetoresistance . . . 4
1.2.2 Giant Magnetoresistance 6
1.2.3 Current Driven Magnetization Reversal: Spin-Torque Effect 6
1.2.4 Spin Injection and Detection in Nonmagnetic Metals 8
1.2.5 Spin Injection and Detection in Semiconductors 8
1.3 Background 10
1.3.1 Spin Injection 11
1.3.2 Spin Relaxation 14
1.3.3 Spin Detection 17
1.4 Thesis Organization 23

II. Epitaxially Grown MnAs/GaAs Lateral Spin-Valves 25

2.1 Introduction 25
2.2 Origin of Magnetoresistance 26
2.3 Growth and Fabrication of Spin-Valves 27
2.4 MnAs/GaAs Tunnel Barrier Characteristics 30
2.5 Magnetoresistance of Spin-Valves 31
2.6 Characteristics of Control Devices 33
2.7 Characteristics of Magnetoresistance 35
2.8 Spin-Selectivity of Tunnel Barrier and Channel Spin Polarization 37
2.9 Conclusion 37

III. Amplification of Spin-Current Polarization 39

3.1 Introduction . . . 39
3.2 Design of a Spin-Current Amplifier . . . 40
3.3 Device Growth and Fabrication . . . 44
3.4 Spin-Valve Characteristics . . . 46
3.5 Spin-Current Amplifier Characteristics . . . 47
3.6 Modeling of Spin-Current Amplifiers . . . 47
3.7 Amplifier Gain Characteristics . . . 51
3.8 Conclusion . . . 52

IV. Two Dimensional Spin Diffusion in Multi-Terminal Lateral Spin-Valves . . . 53

4.1 Introduction . . . 53
4.2 Origin of Two Dimensional Spin Diffusion . . . 54
4.3 Growth and Fabrication of Multi-Terminal Spin-Valves . . . 54
4.4 Characterization of Multi-Terminal Spin-Valves . . . 55
4.5 Modeling of Two Dimensional Spin Diffusion . . . 58
4.6 Enhancement of Spin Polarization . . . 59
4.7 Conclusion . . . 61

V. Electrically Driven Spin-Dynamics of Paramagnetic Impurities: A Spin Capacitor . . . 64

5.1 Introduction . . . 64
5.2 Growth and Fabrication . . . 66
5.3 Transient Characterization of Devices . . . 68
5.4 Origin of Transient Current . . . 69
5.5 Modeling of Spin Dynamics . . . 72
5.6 Determination of Spin Relaxation Time Constant . . . 73
5.7 Conclusion . . . 75

VI. Electrically Injected InAs/GaAs Quantum Dot Spin Laser . . . 76

6.1 Introduction . . . 76
6.2 Growth and Fabrication . . . 78
6.3 Threshold Current Reduction and Output Circular Polarization . . . 79
6.4 Modeling of QD spin-VCSEL . . . 83
6.5 Conclusion . . . 84

VII. Optical Polarization Modulation and Gain Anisotropy in an Electrically Injected Spin Laser . . . 85

7.1 Introduction . . . 85
7.2 Analytical Determination of Laser Ouput Parameters and Gain Anisotropy . 87
7.3 Role of Spin Diffusion on Output Polarization . . . 90
7.4 Device Growth and Fabrication . . . 92
7.5 Polarization Modulation and Threshold Current Reduction . . . 93
7.6 Conclusion . . . 95

VIII. A Monolithically Integrated Magneto-Opto-Electronic Circuit . . . 96

8.1 Introduction . . . 96
8.2 A Magneto-Electronic Switch Based on MOEIC . . . 97
8.3 Principle of Operation . . . 98
8.4 Growth and Fabrication . . . 100

8.5 Characteristics of Circuit Elements . . . 101
8.6 Circuit Operation of MOEIC . . . 104
8.7 Conclusion . . . 105

IX. Conclusion . . . 107

9.1 Summary of Present Work . . . 107
9.1.1 Epitaxially Grown MnAs/GaAs Lateral Spin-Valves . . . 107
9.1.2 Amplification of Spin-Current Polarization . . . 108
9.1.3 Two Dimensional Spin Diffusion in Multi-Terminal Lateral Spin-Valves . . . 108
9.1.4 Electrically Driven Spin-Dynamics of Paramagnetic Impurities: A Spin Capacitor . . . 109
9.1.5 Electrically Injected InAs/GaAs Quantum Dot Spin Laser . . . 109
9.1.6 Optical Polarization Modulation and Gain Anisotropy in an Electrically Injected Spin Laser . . . 110
9.1.7 A Monolithically Integrated Magneto-Opto-Electronic Circuit . . . 110
9.2 Suggestions for Future Work . . . 111
9.2.1 Spin Based Read/Write Memory . . . 111
9.2.2 Spin Based Memory Array . . . 114
9.2.3 Light Sources with Large Polarization Injection . . . 116
9.2.4 Room Temperature Edge Emitting Spin Laser . . . 118

APPENDICES . . . **121**

BIBLIOGRAPHY . . . **145**

LIST OF FIGURES

Figure

1.1 Moore's law for memory chips and microprocessors plotted on a semi-logarithmic scale, which has the effect of making nonlinear exponential curves appear linear. The uppermost purple curve is the Moore projection based on data up to 1975 [Source: Intel Corporation]. 2

1.2 The resistance of a magnetic tunnel junction. 5

1.3 The resistance change due to magnetization reversal of the Co layer from spin-torque effect. 7

1.4 Non-local measurement of spin-accumulation in a multi-terminal all-metal spin-valve. 8

1.5 Modulation of the output signal V/I due to spin precession as a function of a perpendicular magnetic field $B_\perp$. 9

1.6 (a) Schematic representation of the spin dependent density-of-states (DOS) and occupation of the d states in a ferromagnetic metal. (b) Unpolarized DOS of the free electron like s states in a nonmagnetic metal. (c) Spin polarization in a nonmagnetic semiconductor/metal: the induced magnetization. The non-equilibrium population of the spin-up and spin-down states is caused by the injection of spin polarized current. 12

1.7 Four important mechanisms of spin relaxation in semiconductors. (a) The Elliott-Yafet mechanism, in which the electrons scattering off impurities or phonons has a tiny chance to flip its spin at each scattering; (b) the D'yakonov-Perel' mechanism in which electron spins precess along a magnetic field which depends on the momentum. At each scattering the direction and the frequency of the precession changes randomly; (c) the Bir-Aronov-Pikus mechanism, in which electrons exchange spins with holes (circles), which then lose spins very fast due to the Elliott-Yafet mechanism; (d) if electrons wave functions (dashed circles) are confined over a certain region with many nuclear spins, the hyperfine coupling causes spin relaxation and dephasing. 15

1.8 Spin relaxation time in n-type GaAs as a function of (a) donor density at low temperatures (<5 K) and (b) temperature. 18

1.9 Electric dipole allowed radiative interband transitions and corresponding optical polarization for the cases of (a) bulk material with degenerate heavy- and light-hole bands and (b) a quantum well in which epitaxial strain and quantum confinement have lifted the heavy- and light-hole band degeneracy. 19

1.10 A four terminal nonlocal geometry for spin accumulation measurement. 20

1.11 Resistor model of ferromagnet/insulator/semiconductor tunnel junction. The ferromagnetic voltage probe is weakly coupled to the spin-up and spin-down electron population in the semiconductor region. The short-circuiting resistance $2R_N$ represent the spin relaxation due to the nonmagnetic voltage probe strongly coupled to the semiconductor. 21

1.12 Measurement geometry for spin precession measurement and the oscillatory modulation of spin signal. 22

2.1 A schematic of the two-channel model for a conventional lateral spin-valve. 26

2.2 A schematic cross section of a MnAs/GaAs lateral spin valve. Analyzer and polarizer are formed by pattering them on MnAs. The vertical n-doping profile in the channel is also shown. 28

2.3 An SEM image of a 0.5 μm channel length lateral spin-valve. 30

2.4 Zero-bias normalized resistance as a function of temperature for the MnAs/GaAs (FM/NM) tunnel junction. The measured conductance as a function of bias and the corresponding parabolic fit are shown in the inset. 31

2.5 Magnetoresistance and resistance changes at 10 K as a function of applied magnetic field for a 0.5 μm channel length conventional spin valve biased at 5.5 mA. The spin valve is shown schematically in the inset. The legend indicates the length-to-width aspect ratio for the polarizer/analyzer. Open and closed symbols represent the cases of descending and ascending magnetic fields, respectively. 32

2.6 Polarizer and analyzer magnetization characteristics. (a) Hysteresis loop of the contact pads and (b) simulated magnetic domain patterns for a MnAs/GaAs spin valve at different positions along the hysteresis. A zoomed view of the domain patterns near the channel is shown for each case. The inset to (a) shows a schematic depiction of the simulated spin valve with a 10×5 μm^2 analyzer (A) and 50×5 μm^2 polarizer (P). 33

2.7 Resistance change as a function of applied magnetic field for a 1 μm channel length nonlocal spin valve. Top- and side-view schematics of the nonlocal spin valve are shown in the inset. Open and closed symbols represent the cases of descending and ascending magnetic fields, respectively. 34

2.8 Magnetoresistance and resistance changes due to stray effects of a single MnAs strip contact, which is shown schematically in the inset. 35

2.9 Magnetoresistance characteristics. (a) Peak magnetoresistance vs channel length measured at 10 K, (b) peak magnetoresistance vs temperature for a 1 μm spin-valve with applied biases of $I_B = 1.5$, 3.5, and 5.5 mA. The lines represent a linear least squares fit to the data. 36

3.1 The two-channel model for the spin polarization amplifier, which is a dual-drain lateral spin-valve. The polarizer and analyzer are magnetized in opposite directions. 41

3.2 Schematic diagram of a spin polarization amplifier (not to scale). All three contacts S, D1 and D2 have magnetic easy axes along the $\hat{y}$ direction (GaAs [011] direction). The center of contact pad D2 is also the center of the effective channel L_{chan}. A fixed current bias I_{bias} establishes the spin-up and spin-down electrochemical potentials in the channel. The drain2 voltage V_{D2} controls the spin-current in contact pad D2. 41

3.3 The magnetization directions of the three ferromagnetic contact pads S, D1 and D2 as the magnetic field B is swept in both directions. Each group of three arrows (left to right) represents the magnetization directions of S, D2 and D1 contact pads, respectively. The distinct states of magnetizations M1-M4 and the corresponding I_{D2} values for each state are shown for $-B$ to $+B$ sweep. A non-zero drain2 current I_{D2} flows in state M3. 43

3.4 Doping profile in the GaAs channel and GaAs/MnAs transition layer. The zero of the x-axis is the top surface of the semi-insulating GaAs (001) substrate. This confirms the graded doping and the heavily doped GaAs region beneath MnAs, necessary for the Schottky tunnel contact. 44

3.5 An SEM image of the spin-current amplifier after delineating source, drain1 and drain2 contacts by wet etching. 45

3.6 The magnetoresistance of a MnAs/GaAs lateral non-local spin-valve (circles) and drain2 current I_{D2} of a spin polarization amplifier (squares) as a function of applied magnetic field B at 10 K. The filled (open) symbols correspond to $-B$ to $+B$ ($+B$ to $-B$) sweep. The polarizer and analyzer dimensions of the MnAs/GaAs lateral spin-valve are same as that of S and D1 contact pads of the spin polarization amplifier, respectively. The peak values are normalized to unity. The overlap confirms that the peak I_{D2} coincides with the peak anti-parallel alignment between S and D1. . . 46

3.7 (a) Current I_{D2} as a function of magnetic field B for different I_{bias} with V_{D2} set to their corresponding null values (V_{null}) at 10 K; (b) current I_{D2} as a function of magnetic field B for different temperatures T with I_{bias} =100 μA and $V_{D2} = V_{null}$. The filled (open) symbols corresponds to $-B$ to $+B$ ($+B$ to $-B$) sweep. 48

3.8 (a) The peak drain2 current I_{D2} as a function of I_{bias} in state M3. The solid circles represent measured data at 10 K and the solid line represents the theoretically calculated values based on Eqn. 3.8. The spin diffusion length λ_{sf} is found to be 7 μm at 10 K. The spin-up and spin-down currents flow in opposite directions in contact pad D2, yielding spin polarization gain greater than unity; (b) estimated spin diffusion length as a function of temperature. 50

3.9 The anti-symmetric (symmetric) electrochemical potential difference ($\Delta\mu$) between spin-up and spin-down electrons in the channel when S and D1 contact magnetizations are parallel (anti-parallel) for two different temperatures T and I_{bias}. $\Delta\mu$ decreases in the channel at higher temperature due to enhanced spin relaxation. It increases at the source/channel interface ($x = 0$) for higher I_{bias} due to enhanced spin-splitting. 50

3.10 Dual control of the spin polarization gain. The open (closed) symbols represent negative (positive) gain. (a) Spin polarization gain as a function of V_{D2} for varying I_{bias} at 10 K. The gain increases with increasing I_{bias}; (b) spin polarization gain as a function of I_{bias} for varying V_{D2} at 10 K. A constant offset voltage, $V_0 = 19.565$ mV is subtracted from each of the V_{D2} values. The gain curves exhibit singularities along the V_{D2} and I_{bias} axes when a pure spin-current flows through contact pad D2 ($I_{D2} = 0$). 51

4.1 Schematic cross section of a typical three terminal device with $W = 2$ μm. The central terminal selectively collects electron with a particular spin through the voltage source V_c. 55

4.2 Hysteresis characteristics of source and drain contact pads as determined from low temperature MOKE measurements. 56

4.3 Measured collector terminal current I_C vs applied magnetic field H for a $W = 2$ μm device biased at $V_C = V_{null}$. Data are shown for both ferromagnetic and non-magnetic central contact C. 56

4.4 Measured I_C as a function of collector terminal voltage V_C at 10 K for the same device. The line shows the theoretically estimated values for I_C under the same experimental conditions. A schematic of a potential multi-terminal spin-based memory device is shown in the inset. 57

4.5 Estimated current spin polarization (left y axis) and enhancement factor (right y axis) vs measured I_C at 10 K. 60

4.6 (a) Enhancement factor ξ vs normalized collector current I_C/W for various width devices at 10 K; (b) ξ vs device widths W for various levels of normalized carrier extraction I_C/W at 10 K. 61

4.7 Deviation from equilibrium electrochemical potential difference between spin-up and spin-down electrons are plotted for (a) $W = 2$ μm and (b) $W = 16$ μm devices at 10 K. 62

5.1 Schematic cross-section (not to scale) of a typical Mn-doped spin-valve. The channel region is n-type and it is lightly co-doped with Mn impurities. The arrows indicate the initial unpolarized Mn impurities. 65

5.2 The doping densities of silicon (n-doping) and Mn versus channel depth are shown. Mn atoms behave as acceptors and partially compensate the n-doping. Inset shows the SQUID measurement on (Si,Mn) doped channel region grown on semi-insulating GaAs(001) substrate. The absence of remanent magnetization indicates lack of ferromagnetism in the channel region. 67

5.3 MOKE measurements (left y axis) on analyzer and polarizer contact pads, and magnetoresistance measurements on the Mn-doped spin-valves (right y axis) versus applied magnetic field at 10 K. The magnetoresistance data show two peaks which correspond to the antiparallel magnetization alignment of analyzer and polarizer contact pads. The MR loop closely follows the hysteresis of the analyzer contact pad. The arrows indicate the magnetic field sweep directions for the hysteresis plots. Contact pad magnetization data are shown for sweep (1)-(6). The MR loop is shown for sweep (1),(2),(4)-(6). 68

5.4 The measured transient current through the device as a function of time with (a) anti-parallel and (b) parallel magnetization of analyzer and polarizer contacts. The current is initially large before it saturates to a lower value for the anti-parallel configuration. No significant change is observed for the parallel configuration; (c) magnetoresistance, $MR = (I_P\text{-}I_{AP})/I_{AP}$ as a function of time. The solid-lines show $MR(t)$ as determined from the model using appropriate model parameters. An external trigger is generated at $t = 0$. There is a delay of ∼150 ns for the voltage source and the electrometer to respond to this trigger, which leads to the the shift in the origin for the time axis by the same amount. 70

5.5 Equivalent circuit diagram of the SCT structure: g_γ, g_{so}, $G_{\uparrow(\downarrow),P}$, $G_{\uparrow(\downarrow),A}$, g_α, g_β, r,$\mu_{\uparrow(\downarrow)}$, and, I_{sf} are spin-flip conductance due to Mn impurity, spin-flip conductance independent of Mn impurity, polarizer conductance for up(down)-spin, analyzer conductance for spin-up(down) electrons, majority-spin tunnel conductance, minority-spin tunnel conductance, polarizer to analyzer area ratio, average chemical potential for spin-up(down) channel electrons, and, total spin-flip current respectively. The current source $I_\gamma \propto \int dE\{f_\uparrow(1-f_\downarrow)+f_\downarrow(1-f_\uparrow)\}(F_\uparrow - F_\downarrow)$, where, $f_{\uparrow(\downarrow)}$ and $F_{\uparrow(\downarrow)}$ are the average energy (E) distribution of spin-up(down) electrons having chemical potential $\mu_{\uparrow(\downarrow)}$ and fraction of impurities having up(down)-spin respectively. 71

5.6 (a) Estimated spin-flip current as a function of time, for $T = 10$ and 15 K. The spin-capacitive effect is reduced at higher temperatures due to enhanced spin-relaxation from native GaAs lattice atoms; (b) *charging* of Mn paramagnetic spin as a function of time. 74

6.1 Schematic cross section of an InAs QD spin-VCSEL heterostructure with (a) magnetic and (b) nonmagnetic n-contact grown by molecular-beam epitaxy (MBE). . . 78

6.2 Measured degree of output circular polarization vs magnetic field for a 15 μm mesa diameter MnAs spin-VCSEL (circle) and control VCSEL (square) measured at 200 K are shown. The spin-VCSEL polarization closely follows the out-of-plane magnetization curve for MnAs. 80

6.3 Threshold current reduction vs magnetic field for a 15 μm mesa diameter MnAs spin-VCSEL measured at 200 K. Inset shows the measured light-current characteristics. 81

6.4 (a) Emission intensity enhancement vs normalized current (I/I_{th}) measured for different magnetic fields; (b) variation in threshold current reduction ($\Delta I_{th}/I_{th}$) vs normalized current (I/I_{th}) measured at a magnetic field of 3.1 T. 82

6.5 (a) Calculated threshold current reduction vs pump-current spin polarization for spin relaxation time $\tau_{sf} = 75$ ps; (b) calculated variation of the spin polarization values in the barrier and in the QDs vs normalized current. 84

7.1 Heterostructure of GaAs-based spin-VCSEL grown by molecular beam epitaxy. The active (gain) region consists of 10 periods of self-organized InAs/GaAs quantum dots placed in a GaAs -cavity. The top distributed Bragg reflector (DBR) mirror consists of 5 pairs of ZnSe/MgF_2 deposited by PVD. The ferromagnetic MnAs/$Al_{0.1}Ga_{0.9}As$ tunnel injector contact is regrown selectively on GaAs after a mesa-etch stop, as shown in the figure. 86

7.2 Schematic representation of the variation of carriers spin polarization with distance from ferromagnetic contact (MnAs) in VCSEL in accordance with the spin diffusion equation. The barrier (cavity) is at distance x_1 and the quantum dot region is at distance x_2. The spin polarization decreases with increasing pump current. In the barrier and quantum dots the polarization decreases from $P_{spin,1}$ to $P_{spin,2}$ and Π_{S1} to Π_{S2}, respectively. 87

7.3 Calculated variation of gain anisotropy parameter with normalized pump current. . 90

7.4 Calculated and measured modulation of output circular polarization of InAs/GaAs QD spin-VCSEL as a function of normalized pump current at different magnetic fields. 91

7.5 Calculated and measured reduction of threshold current with magnetic field applied perpendicular (hard axis) to the plane of the MnAs contact. The inset shows the calculated and measured percentage reduction of threshold current with field. . . . 92

7.6 Measured modulation index versus pump current. The calculated values are shown for currents at and above threshold. 94

8.1 A schematic of the magneto-opto-electronic integrated circuit. A magnetic field changes the resistance of the spin-valve. The magnetoresistance is amplified by the cascaded transconductance HEMT amplifier to a large change in drain-to-source current which modulates the light intensity of the LED. The resistors R_1 and R_2 are used to correctly bias the cascaded HEMT amplifier in the linear region. 99

8.2 A schematic of the MOEIC heterostructure grown by MBE. The heterostructure consists of epitaxially grown layers for the MnAs/GaAs lateral spin-valve, the GaAs/$Al_{0.2}Ga_{0.8}As$ multi-quantum-well LED and the $Al_{0.2}Ga_{0.8}As/In_{0.2}Ga_{0.8}As$ pseudomorphic HEMT separated by undoped GaAs buffer layers. 101

8.3 (a) A schematic and (b) a micro-photograph of the fabricated MOEIC (before the final interconnection and metallization step). The resistors R_1 and R_2 are delineated on undoped GaAs buffer layers by physical vapor deposition and lift-off technique. 102

8.4 (a) The spin-valve shows two magnetoresistance peaks corresponding to the case when the polarizer and the analyzer are magnetized in opposite directions. The magnetoresistance decreases with increasing temperature due to decreasing spin-relaxation time; (b) non-local voltage as a function of perpendicular magnetic field in a spin-valve. The spin precesses due to Hanle effect which leads to the change in spin accumulation. The asymmetry is due to a small misalignment of the sample and presence of a small axial magnetic field. 103

8.5 (a) Transconductance g_m of the HEMT as a function of gate-to-source voltage. It reaches peak at V_{GS} = -0.9 V; (c) transconductance of the HEMT as a function temperature. It increases with decreasing temperature due to increasing mobility. 104

8.6 (a) LED light output and terminal voltage as a function of bias current; (b) light output versus bias current of the LED as a function of temperature. The quantum efficiency increases with decreasing temperature, hence, the slope increases. 105

8.7 MOEIC characteristics. Modulation of LED light intensity as a function of magnetic field. The light intensity modulation shows exactly the same magnetic field dependence as the spin-valve characteristics. The magnetoresistance amplification is determined to be ~20 in the region of operation. The MOEIC acts as a magneto-electronic switch which varies LED light intensity in response to an external magnetic field. 106

9.1 A schematic of the proposed spin-based memory device. The two large ferromagnetic contact pads act as source and drain, which create an electrochemical potential splitting in the anti-parallel configuration. The central ferromagnetic contact pads on the channel region act as memory bits. 111

9.2 A typical hysteresis of a sputtered thin FeGaB film on GaAs. The coercivity is very small ~1-2 Oe 113

9.3 Read operation of the memory bits. The current flowing through through '0' (I_2 and I_4) and '1' (I_1 and I_3) have different signs. 114

9.4 A schematic of the proposed spin-based memory array. The memory is arranged in a 4×4 array with monolithically integrated address and read/write circuits. . . . 115

9.5 A schematic of the light source with large polarization injection 117

9.6 current through the Ti/Au non-magnetic central contact. The current is large when source and drain are magnetized in opposite directions. 118

9.7 A schematic of the proposed edge emitting laser with an InP based lattice matched system. The top n-contact injects spin-polarized carriers into the InGaAs active region. 119

9.8 (a) A schematic of the edge-emitting laser for electrical switching of output polarization; (b) hysteresis characteristics of the n-contact pads. 120

C.1 Variation of $n_\uparrow$ as a function of $(\mu_\uparrow - E_c)$ determined from Eqn. C.13, where E_c is the conduction band edge. The solid line depicts a least-square linear fit to the calculated values. 129

E.1 A schematic of the MOEIC heterostructure grown by MBE. Each epitaxial layer is labelled with a number from the top. 141

E.2 Micro-photographs of the MOEIC after each fabrication step. 144

LIST OF TABLES

Table

1.1 Emerging Research Logic Devices 3

6.1 Quantum dot parameters at 200 K used to analyze spin laser performance characteristics 83

LIST OF APPENDICES

Appendix

A. Two-Channel Model for a Spin-Valve . . . 122

B. Modeling of a Spin-Current Amplifier . . . 124

C. Spin-Dynamics in a Spin-Capacitor . . . 127

C.1 Relation between Spin-Flip current and Spin-Carrier Density . . . 127
C.2 Time Dependent Spin Diffusion Equation . . . 128
C.3 Relation between Carrier Density and Fermi Level . . . 129

D. Modeling of Polarization Modulation . . . 131

D.1 Definition of Laser Parameters . . . 131
D.2 Coupled Laser Rate Equations . . . 132
D.3 Transport of Spin-Polarized Carriers in a Laser . . . 132
D.4 Definition of Spin Polarization . . . 133
D.5 Operation of a Spin Laser . . . 134
D.6 Barrier Spin Polarization and QD Spin Polarization . . . 134
D.7 Threshold Current without Magnetic Field . . . 137
D.8 Threshold Current with Magnetic Field . . . 138
D.9 Output Circular Polarization . . . 138
D.10 Amplification of Spin Polarization . . . 138

E. Fabrication Steps for MOEIC . . . 140

LIST OF ACRONYMS

Acronym

3D three-dimensional

ac alternating current

ALU arithmetic logic unit

AMR anisotropic magnetoresistance

BEP beam equivalent pressure

CIP current in plane

CPP current perpendicular to plane

CW continuous wave

DBR distributed Bragg reflector

DNP dynamic nuclear polarization

DP D'Yakonov-Perel'

FM ferromagnetic

GMR giant magnetoresistance

HEMT high electron mobility transistor

IC integrated circuit

ITRS International Technology Roadmap for Semiconductors

LED light-emitting diode

LT low temperature

MBE molecular-beam epitaxy

MEMS micro-electro-mechanical systems

MOEIC magneto-opto-electronic integrated circuit

MOKE Magneto-Optic-Kerr-Effect

MOS metal-oxide-semiconductor

MR magnetoresistance

NEGF Non-equilibrium Green's Function

NM non-magnetic

PECVD plasma enhanced chemical vapor deposition

PEM photoelastic modulator

PVD physical vapor deposition

RIE reactive ion etching

RHEED reflection high-energy electron diffraction

SEM scanning electron microscope

SI semi-insulating

SIMS secondary ion mass spectroscopy

spin-VCSEL spin-polarized vertical-cavity surface-emitting-laser

SQUID superconducting quantum interference device

TMR tunneling magnetoresistance

QD quantum dot

QW quantum well

VCSEL vertical-cavity surface-emitting laser

ABSTRACT

FERROMAGNET/SEMICONDUCTOR BASED SPINTRONIC DEVICES

by
Dipankar Saha

Chair: Pallab Bhattacharya

Spintronics is an emerging field which is great interest for its potential to provide high-speed and low-power novel devices and eventually replace and/or complement conventional silicon-based metal-oxide-semiconductor (MOS) devices. Spin-based optoelectronic devices provide improved laser performance and polarized light sources for secure communication. Spintronics has therefore received a lot of interest with the potential for conventional and novel applications. Spintronics has been investigated both in all-metal and semiconductor based platforms. Spin-based ferromagnet/semiconductor heterojunction devices are particularly attractive compared to all-metal spintronic devices due to the versatility and the long electron spin coherence time in semiconductors. Here we have investigated semiconductor based spintronic devices for logic, memory and communication applications.

We have demonstrated electrical injection and detection of spin in a MnAs/GaAs lateral spin valve. A peak magnetoresistance of 3.6% at 10 K and 1.1% at 125 K have been measured in these devices. Spin polarization in semiconductors is usually very small and difficult to detect. We have therefore theoretically designed and

experimentally demonstrated a spin-current amplifier to alleviate this problem. A spin polarization of 100% has been measured at 150 K in these devices. We have emphasized the importance of finite sizes of ferromagnetic contact pads in terms of two-dimensional spin-diffusion in lateral spintronic devices, which enhances spin-polarization. We have discovered a new phenomenon observing electrically driven spin-dynamics of paramagnetic impurities. We have demonstrated a spin-capacitor using this novel phenomenon.

In this study we have also demonstrated a spin-polarized quantum dot spin-laser which is a fundamental spin-based optoelectronic device. An output circular polarization of 8% and threshold current reduction of 14% have been measured at 200 K. We have also demonstrated electrical modulation of output circular polarization in a spin-VCSEL. We have highlighted the importance of spin-transport in spin-lasers by analytically solving carrier-photon coupled laser rate equations. We have finally demonstrated Magneto-Opto-Electronic Integrated Circuit (MOEIC), which monolithically integrates a spin-valve (magnetic), a LED (optoelectronic) and a cascaded HEMT amplifier (electronic), acting as a magneto-electronic switch. The operation of the MOEIC has been experimentally characterized.

CHAPTER I

Introduction

1.1 Beyond Moore's Law

Moore's law describes an important trend in the microelectronics semiconductor industry. Since the invention of the first integrated circuit in 1958, the number of transistors on a single die has grown exponentially, doubling approximately every two years. The trend was first observed by Intel co-founder Gordon. E. Moore [1]. Moore's law has been true for almost half a century and the progress is not expected to stop in the near future. Fig. 1.1 shows a plot of the Moore's law for memory chips and microprocessors. The y-axis is plotted on a logarithmic-scale. A linear trend in the plot indicates an exponential growth in the number of transistors per die. The factor of *two* increase in every two-years (generation/node) comes mainly from the shrinking of critical feature sizes of devices. The dimension of the devices is reduced by a factor of $\sqrt{2}$ in both the x and y in-plane directions. As the die size is kept fixed, there is a factor of $(\sqrt{2})^2 = 2$ increase in the number of the transistors for the same active area. A decrease in the feature sizes brings in additional benefits: high speed, low power, more functionalities, lower cost per transistor etc. Almost every measure of the capabilities of digital electronic devices is linked to Moore's law: processing speed, memory capacity, even the number and size of pixels in digital cameras. All

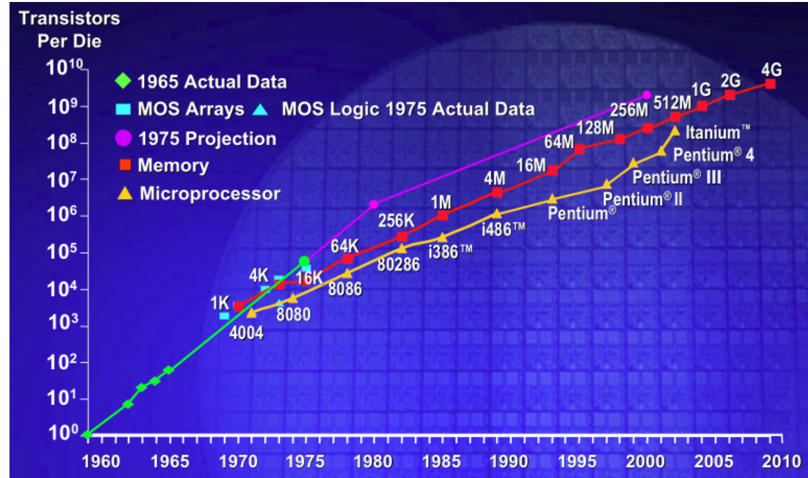

Figure 1.1: Moore's law for memory chips and microprocessors plotted on a semi-logarithmic scale, which has the effect of making nonlinear exponential curves appear linear. The uppermost purple curve is the Moore projection based on data up to 1975 [Source: Intel Corporation].

of these are improving at (roughly) exponential rates as well.

As Moore's Law gained acceptance, it served more as a goal and driver for the microelectronics industry than a simple observation. Semiconductor industries try to keep up with the shrinking of the device feature sizes so that Moore's law remains valid as long as possible. The continuous shrinking has led to a lot of technological problems, which are shown as red bricks in the International Technology Roadmap for Semiconductors (ITRS) [2]. The reliable operation of the devices depend on a large number of factors; and it has led to a lot of innovations in the area of microelectronics fabrication technology to circumvent these problems. In spite of the discoveries enhancing the technological capabilities, it is envisioned that conventional MOS devices are soon going to reach the fundamental physical limit, where they will seize to work if the feature sizes are further reduced. Several emerging research areas have been identified in ITRS , that will allow improvement of the device performances and Moore's law will continue to be valid (Table 1.1) [2]. Spintronics is one of the potential candidates in this area which has received a lot of attention recently. While

Table 1.1: Emerging Research Logic Devices

	Scalability	Performance	Energy Efficiency	Gain	Operational Reliability	Operational Temperature***	CMOS Technological Compatibility**	CMOS Architectural Compatibility*
1D Structures	2.4	2.2	2.5	2.3	2.0	2.5	1.8	2.3
Channel Replacement Materials	2.0	2.9	2.3	2.4	1.9	2.3	1.8	2.5
Single Electron Transistors	2.4	1.1	2.3	1.2	1.3	1.4	1.6	1.5
Molecular Devices	2.5	1.5	2.2	1.5	1.3	1.8	1.6	1.7
Ferromagnetic Devices	1.2	1.3	1.7	1.5	2.0	2.1	1.2	1.3
Spin Transistors	1.7	1.4	2.3	1.7	1.4	1.3	1.3	1.3

an interesting subject on its own, it has immense potential to produce high packing density, low power and high speed devices.

1.2 Spintronics

In a conventional *charge* based device, a potential difference is created between a source and a sink. Electrons flow down the potential hill from the source and are collected by the sink. The channel conductance is primarily modulated by changing the number of carriers in the channel. In addition to charge, an electron has *spin* as

one of the degrees of freedom, which was discovered by Stern and Gerlach in 1922. As a quantum mechanical system, the electron spin is usually represented by a two component vector, called spinor,

$$\begin{pmatrix} S_{\uparrow} \\ S_{\downarrow} \end{pmatrix} \tag{1.1}$$

where the top and bottom components, both complex numbers, represent the amplitude probability to be in the *spin-up* and *spin-down* states, with reference to a predefined direction in space [3]. Any spatial spin direction may be depicted by appropriately choosing $S_{\uparrow}$ and $S_{\downarrow}$ and maintaining the normalization condition, $S_{\uparrow}S_{\uparrow}^{*} + S_{\downarrow}S_{\downarrow}^{*} = 1$. For instance, once the x and y axes are fixed, spins in the positive x, y, and z direction are written in the basis of spin up/down in the z direction as,

$$+\hat{x} \rightarrow \frac{1}{\sqrt{2}}\begin{pmatrix} 1 \\ 1 \end{pmatrix}, \qquad +\hat{y} \rightarrow \frac{1}{\sqrt{2}}\begin{pmatrix} 1 \\ i \end{pmatrix}, \qquad +\hat{z} \rightarrow \frac{1}{\sqrt{2}}\begin{pmatrix} 1 \\ 0 \end{pmatrix} \tag{1.2}$$

Spin-electronic (spintronic) devices exploit properties of electron spin for useful applications.

Spintronic devices can be broadly classified as two-terminal and three-terminal devices. The two-terminal (source/polarizer and drain/analyzer) devices are mainly the magnetoresistive devices, where the resistance between the two terminal changes for various orientations of the magnetization directions of the two contacts. The three-terminal (multi-terminal) devices has additional contact(s) in addition to the source and drain terminals, which allow manipulation of spin-transport. Here, we discuss some of the basic spintronic components from a historical perspective.

1.2.1 Magnetic Tunnel Junctions and Tunneling Magnetoresistance

The first study of spin polarized tunneling was done by Tedrow and Mersevey on $Al/Al_2O_3/Fe$ tunnel junctions [4]. Julliere later reported studies on Fe/Ge/Co junc-

tions [5], in which the magnetic orientation of the two ferromagnets in a two-terminal geometry could be varied independently, owing to the different switching fields of the two ferromagnets. The device conductance depends on the relative alignment of the two ferromagnetic (Fe and Co) contacts. In the antiparallel orientation, majority electrons of source are minority electrons in the drain, and do not have available states to tunnel into. The conductance (G_{AP}) is therefore low in this case. For a similar reason, the conductance (G_P) is higher when source and drain are magnetized in the same direction. The tunneling magnetoresistance (TMR) is defined as,

$$TMR = \frac{G_P - G_{AP}}{G_{AP}} = \frac{2P_S P_D}{1 - P_S P_D} \tag{1.3}$$

where P_S and P_D are the polarizations of the source and the drain, respectively. The polarization is a function of density of states of the ferromagnets and transmission probabilities at the junctions. The typical magnetoresistance behavior of a $Co/Al_2O_3/Ni_{80}Fe_{20}$TMR device is shown in Fig. 1.2 [6]. The magnetoresistance

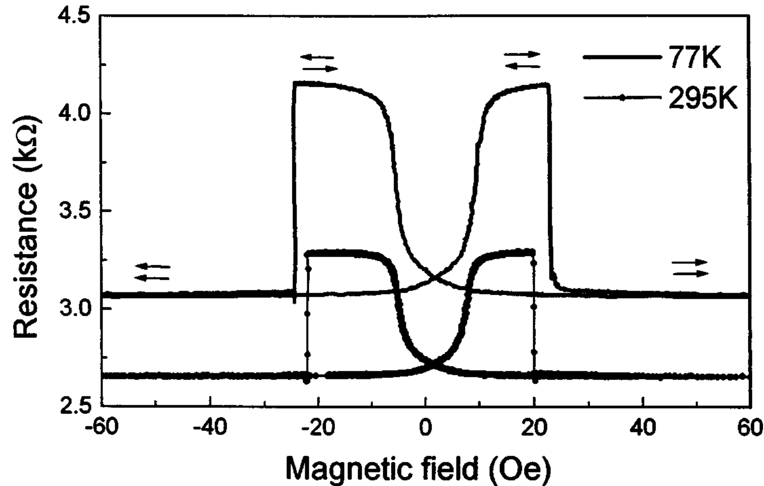

Figure 1.2: The resistance of a magnetic tunnel junction.

decreases with increasing temperature due to spin-magnon scattering which reduces P_S and P_D.

1.2.2 Giant Magnetoresistance

Giant magnetoresistance (GMR) refers to the resistance of two terminal devices consisting of non-magnetic layers interleaved by ferromagnetic layers. The discovery of giant magnetoresistance has led to research in the all-metal spintronic devices for memory applications. The GMR devices are broadly classified in two categories: current in plane (CIP) [7] and current perpendicular to plane (CPP) [8]. The classification is based on the direction of current flow parallel (CIP) or perpendicular (CPP) to the metal layers. The resistance change of GMR devices is much larger than that of the TMR devices and the CPP geometry shows a larger change in magnetoresistance than its CIP counterpart. The magnetoresistance characteristics of GMR devices are similar to the TMR devices. In both the geometries, the resistance depends on whether the ferromagnetic layers are aligned parallel or antiparallel with respect to each other. The physical origin of magnetoresistance in GMR devices is due to the spin dependent scattering of conduction electrons at the ferromagnet/non-magnet interfaces and the bulk ferromagnets.

1.2.3 Current Driven Magnetization Reversal: Spin-Torque Effect

The spin of a free electron gives rise to a magnetic moment, opposite to the spin direction, of magnitude,

$$m = \frac{g_0}{2}\mu_B \tag{1.4}$$

where g_0 is the electron g-factor and μ_B is the Bohr magneton. The g-factor is,

$$g_0 = 2\left(1 + \frac{\alpha}{2\pi} + ...\right) \approx 2.0023. \tag{1.5}$$

The value of 2 comes from the Dirac equation. The remaining part comes from the anomalous contribution proportional to the fine structure constant, $\alpha = e^2/\hbar c 4\pi\epsilon_0$.

The electron g-factor in semiconductors can be very different from the free electron case. In simple metals, the electron g-factor is very near to the free electron value, however it can be very large (~ 50) or very small (~ 0.5) in semiconductors.

If a current $\mathbf{I}_S$ of spin polarized electrons is injected into a ferromagnet, it induces a torque

$$\boldsymbol{\tau} = \mathbf{m} \times \mathbf{I}_S \times \mathbf{m} \tag{1.6}$$

on the ferromagnet that can change the direction of magnetization. This spin-torque effect was theoretically proposed by Berger [9] and Slonczewski [10]. The effect was confirmed later by several experimental demonstrations [11, 12] on pillar like structures. Fig. 1.3 shows such a measurement taken with 1200 Oe applied in plane

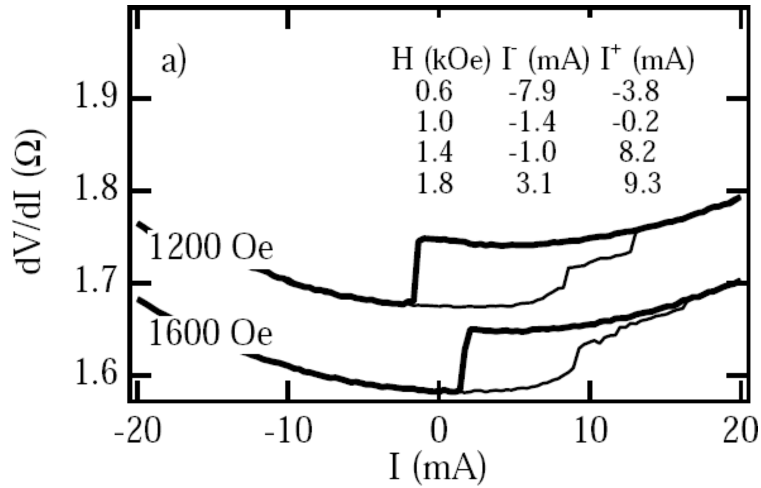

Figure 1.3: The resistance change due to magnetization reversal of the Co layer from spin-torque effect.

magnetic field [11]. The initial parallel alignment gives a smaller resistance value. As the current increases the magnetization of the thin Co layer changes in the other direction. The two ferromagnetic contacts gradually become magnetized in opposite directions, which lead to an decrease in the conductance, and hence the resistance dV/dI increases.

1.2.4 Spin Injection and Detection in Nonmagnetic Metals

The injection of spin polarized carriers into non-magnetic metals was first proposed by Aronov [13] and it was experimentally demonstrated by Johnson and Silsbee [14]. Figure 1.4 shows the geometry used by them to detect spin accumulation in

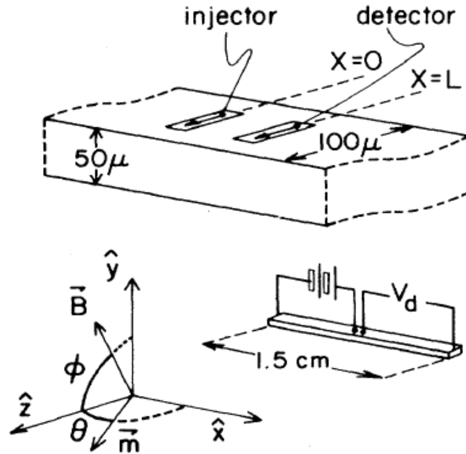

Figure 1.4: Non-local measurement of spin-accumulation in a multi-terminal all-metal spin-valve.

the non-magnetic metal. This geometry became very popular as *non-local* measurement of spin-accumulation, which alleviates spurious effects in the measurements due to ferromagnetic contacts. Jedema *et al.* provided further evidence for spin injection and detection in metals through precession measurements [15], also called Hanle effect: a magnetic field applied perpendicular to the spin, makes it precess at a constant angular velocity $\omega_L = g\mu_B|B|/\hbar$. Electrons traversing from injector to detector acquire a precession angle proportional to the traversal time. At the detector, the spin imbalance is expected to periodically reverse sign, as a function of $B_\perp$. A typical plot of such a measurement is shown in Fig. 1.5.

1.2.5 Spin Injection and Detection in Semiconductors

The spin transport length in semiconductors is much larger than that in metals. This generated a lot of interest for semiconductor spintronics. The spin transport

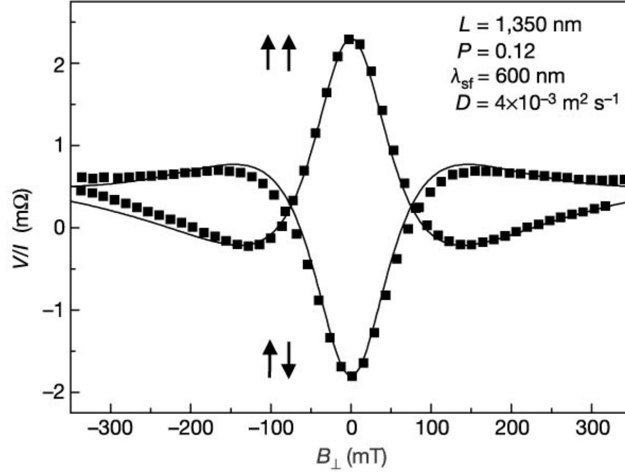

Figure 1.5: Modulation of the output signal V/I due to spin precession as a function of a perpendicular magnetic field $B_\perp$.

length for holes is usually very small. Therefore most of the semiconductor spintronic work has focused on spin polarized electrons. Several techniques have been developed to create an imbalance between spin-up and spin-down electrons in the semiconductors:

- Optical injection of spin polarized carriers by shining a circularly polarized light with wavelength tuned above the absorption edge of the semiconductors [16]. A population of spin polarized electron and holes are created in this process. The spin polarization of holes decay very fast, leaving a spin polarized electrons in the semiconductor. This method is particularly suitable for direct bandgap semiconductors. Optical generation of spin polarized carriers has revealed a wealth of information on spin transport. However, this method is unsuitable for practical applications.
- Electrical spin injection from ferromagnets into semiconductors is a better technique to inject spin polarized electrons in semiconductors. However, the conductivity mismatch between ferromagnetic metals and semiconductors limit enormously the injection and detection efficiencies [17]. One of the approach to

circumvent this problem is to inject electrons through a tunnel barrier [18]. Schottky tunnel barrier is a natural choice for semiconductors. Several devices have been demonstrated using ferromagnet/semiconductor Schottky tunnel barrier spin injectors and detectors [19–22].

- An alternative way of avoiding the conductivity mismatch problem is to use dilute magnetic semiconductors (DMS) [23]. However, most of the DMS ((Ga,Mn) As, (Be,Mn)Te etc.) work at low temperatures with Curie temperatures much below 300 K. They are not suitable for high temperature operation. Also, many DMS (like (Ga,Mn)As) inject spin polarized holes instead of electrons, which also limit their usage.
- Hot carrier injection is another way to circumvent the problem of conductivity mismatch. Using this method, electrical spin injection and detection, in the indirect bandgap semiconductor Si, have been demonstrated by Monsma *et al.* [24] and Appelbaum *et al.* [25]. However the magnitude of spin-current in this method is very small, which limits its usage.

1.3 Background

There are three common aspects to all semiconductor spintronic devices: spin injection, spin transport and spin detection [26]. All the devices described in this thesis involve electrical spin injection into the semiconductors. The spin detection is done optically in spin-based optoelectronic devices *e.g.* spin-LEDs and spin-lasers, and electrically in spin-based electronic devices *e.g.* spin-valves, spin-transistors, spin-capacitors *etc.* In spin-based optoelectronic devices, spin polarized electrons combine radiatively with unpolarized holes in an active gain medium emitting circularly polarized light. Whereas in a spin-based electronic device, injected spin polarized

carriers from the polarizer/source traverse towards the drain/analyzer and are electrically detected. The spin polarization of electrons decreases during its travel due to spin-relaxation from various spin-scattering mechanisms. Semiconductors with long spin-relaxation time are therefore desirable for useful applications. GaAs is the most studied material for spintronic devices, which has a long spin transport length (∼20-50 μm) at low temperatures and ∼1-2 μm near room temperature. Since current nanofabrication technology allows feature sizes less than a micron with little or no difficulty, GaAs is an appropriate host for spintronic devices. In addition, it is a direct bandgap material (compared to Si which is an indirect bandgap semiconductor), which makes it also suitable for optoelectronic devices. Another important aspect of spintronics is spin-manipulation which is exercised during spin transport to modify spin polarization to achieve desirable terminal (I–V) characteristics.

1.3.1 Spin Injection

In an equilibrium condition, the number of spin-up and spin-down electrons in the conduction band of a semiconductor are equal. The method of creating a non-equlibrium population between two states is termed as spin injection. The natural choice for injecting spin is to use ferromagnets which have unequal number of spin-up and spin-down electrons at the Fermi level, as schematically shown in Fig. 1.6(a) [27]. As the conductivities for the spin-up and spin-down electrons in a ferromagnetic metal are unequal, the charge current ($I_\uparrow + I_\downarrow$) in a ferromagnet is accompanied with a spin-current ($I_\uparrow - I_\downarrow$) which transports magnetization. When the electrons carrying the spin-current cross the ferromagnet/semiconductor interface the conductivities for both type of electrons become equal (Fig. 1.6(b)). This causes an imbalance between the number of spin-up and spin-down electrons in the semiconductor and their electrochemical potentials ($\mu_\uparrow$ and $\mu_\downarrow$) split up, as shown in Fig. 1.6(c). The difference

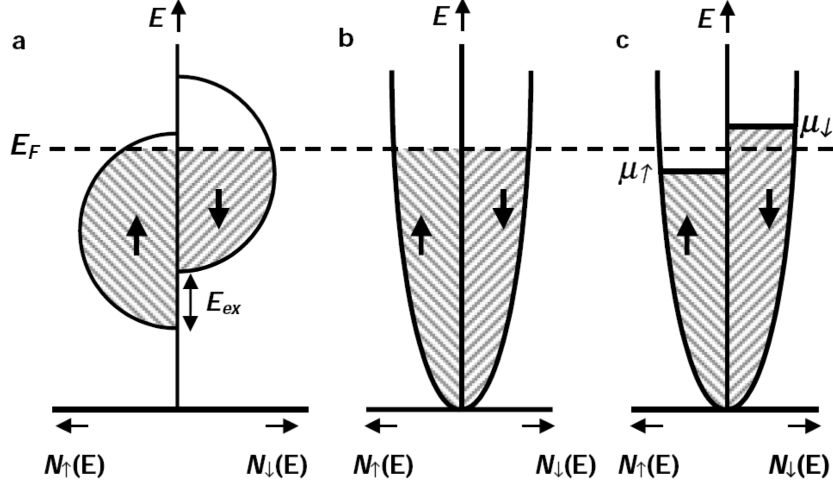

Figure 1.6: (a) Schematic representation of the spin dependent density-of-states (DOS) and occupation of the d states in a ferromagnetic metal. (b) Unpolarized DOS of the free electron like s states in a nonmagnetic metal. (c) Spin polarization in a nonmagnetic semiconductor/metal: the induced magnetization. The non-equilibrium population of the spin-up and spin-down states is caused by the injection of spin polarized current.

in electrochemical potentials, $\Delta\mu = (\mu_\uparrow - \mu_\downarrow)$ is also called spin-accumulation. The non-equilibrium electron spin polarization in the semiconductor is defined as,

$$\Pi_{inj} = \frac{n_\uparrow - n_\downarrow}{n_\uparrow + n_\downarrow} \tag{1.7}$$

where $n_\uparrow$ ($n_\downarrow$) is the number of spin-up (spin-down) electrons. The conductivity of the ferromagnetic metals is very large compared to the semiconductors. It can be shown that the spin polarization (neglecting spin relaxation) in the semiconductor region of a ferromagnet/semiconductor/ferromagnet sandwich structure is approximately given by [17],

$$\Pi_{inj} = K\frac{\sigma_{sc}}{\sigma_{fm}} \tag{1.8}$$

where K is a constant determined from details of the type of the materials and interfaces used, and σ_{sc} (σ_{fm}) is the conductivity of the semiconductor (ferromagnet). Hence, spin injection efficiency is directly proportional to the ratio of the conductivity of semiconductor to that of ferromagnet, which is very small. This effect is commonly known as “conductivity mismatch” problem.

It is proposed that putting a high resistance tunnel barrier between the ferromagnet and the semiconductor will alleviate this problem [18]. The spin injector is therefore designed to consist of ferromagnet/insulator/semiconductor heterostructure. The presence of tunnel barrier increases the efficiency of spin injection into the semiconductors. The tunnel barrier provides high spin dependent resistances bridging the ferromagnet and the semiconductor, and reduces the probability of electrons reflected back into the ferromagnet. In presence of a high resistance tunnel barrier, it can be shown that the spin polarization in the semiconductor is given by [18],

$$\Pi_{inj} = \frac{R_{\uparrow}^{TB} - R_{\downarrow}^{TB}}{R_{\uparrow}^{TB} + R_{\downarrow}^{TB}} \tag{1.9}$$

where $R_{\uparrow}^{TB}$ ($R_{\downarrow}^{TB}$) is the spin dependent tunnel resistance for spin-up (spin-down) electrons. The conductivity of the semiconductor is not important as long as the tunnel barrier resistance is much higher than that of the semiconductor. The physical mechanism of the spin filtering effect of the tunnel barrier is related to the transmission probabilities for the spin-up and spin-down electrons. A tunnel barrier is also used in magnetic tunnel junctions for TMR devices.

There have been several reports on spin injection into semiconductors using various ferromagnet, insulating tunnel barrier and semiconductor combinations. The magnitude of spin polarization measured in the semiconductor also varies widely. Fe and CoFe are the two most notable ferromagnetic metals which are reported to have high injection efficiencies into GaAs when used with AlO_x and MgO tunnel barriers. Spin polarization as large as 50-70% have been reported from these materials [28,29]. While dielectric materials can be used as tunnel barriers, Schottky tunnel barrier is a natural choice for semiconductors. Spin polarization injection using Fe/AlGaAs and Fe/GaAs Schottky tunnel barriers have also widely been reported [30–32]. Here, we have used ferromagnetic semimetal MnAs as the spin injector and MnAs/GaAs

Schottky tunnel barrier. We have determined a spin polarization of 31% in GaAs.

1.3.2 Spin Relaxation

Spin polarized carriers in a semiconductor do not retain the polarization for indefinite amount of time. The spin polarization becomes zero due to various spin relaxation mechanisms and the number of spin-up and spin-down electrons become equal and attain the equilibrium condition. The spin relaxation times are defined with the help of Bloch equations. To determine the spin relaxation times, a magnetic field $B_0\hat{z}$ and an oscillating field $\mathbf{B}_1(t)$ are applied to an ensemble of electrons with total spin $\mathbf{S}$. The time evolution of the three spin components are given by,

$$\frac{\partial S_x}{\partial t} = \gamma(\mathbf{S}\times\mathbf{B})_x - \frac{S_x}{T_2} \tag{1.10}$$

$$\frac{\partial S_y}{\partial t} = \gamma(\mathbf{S}\times\mathbf{B})_y - \frac{S_y}{T_2} \tag{1.11}$$

$$\frac{\partial S_z}{\partial t} = \gamma(\mathbf{S}\times\mathbf{B})_z - \frac{S_z - S_{0z}}{T_1} \tag{1.12}$$

where $\mathbf{B} = B_0\hat{z}+\mathbf{B}_1$ is the total field and γ is the gyromagnetic ratio, $\gamma = g\mu_B/\hbar$. The time T_1 is called the spin/longitudinal/spin-lattice relaxation time and T_2 is called the spin-dephasing/transverse/spin-spin relaxation time. The inverse of the spin relaxation time ($1/T_1$) gives the rate at which the spin along the static magnetic field decays to the equilibrium value. The spin system exchanges energy when a non-zero magnetic field is present and the initial and final state energies are different. T_2 determines the dephasing of the spin component transverse to the static field.

There are four spin relaxation mechanism of conduction electrons in semiconductors: Elliott-Yafet (EY), D'yakonov-Perel' (DP), Bir-Aronov-Pikus (BAP), and relaxation through hyperfine coupling with nuclear spins. The relative strength of different mechanisms depend on the particular material (*e.g.* semiconductor type, doping, defects, strain) and the operating conditions (*e.g.* temperature, magnetic

field, electric field, confinement). The spin scattering mechanisms are schematically shown in Fig. 1.7 [33].

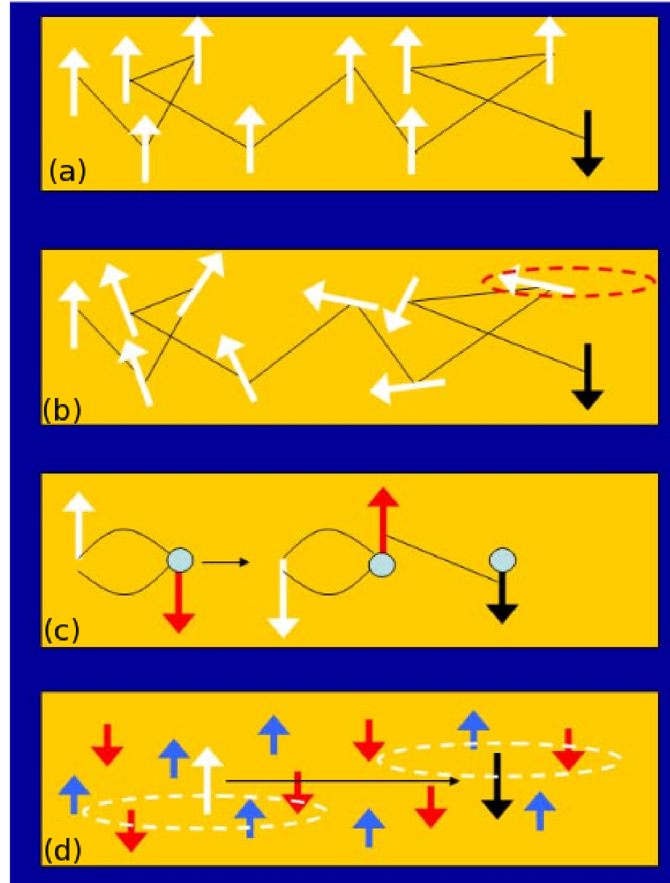

Figure 1.7: Four important mechanisms of spin relaxation in semiconductors. (a) The Elliott-Yafet mechanism, in which the electrons scattering off impurities or phonons has a tiny chance to flip its spin at each scattering; (b) the D'yakonov-Perel' mechanism in which electron spins precess along a magnetic field which depends on the momentum. At each scattering the direction and the frequency of the precession changes randomly; (c) the Bir-Aronov-Pikus mechanism, in which electrons exchange spins with holes (circles), which then lose spins very fast due to the Elliott-Yafet mechanism; (d) if electrons wave functions (dashed circles) are confined over a certain region with many nuclear spins, the hyperfine coupling causes spin relaxation and dephasing.

In the EY mechanism, the spin relaxes by momentum scattering off impurities or phonons. Electron states are mixtures of spin-up and spin-down states, due to spin-orbit coupling. The coupling is weak, and the states can still be called as spin-up and spin-down with respect to the quantization axis. Each momentum scattering gives a probability to flip the spin from up to down state, leading to spin relaxation.

The spin relaxes during the scattering and increased momentum scattering gives rise to increased spin scattering. The EY mechanism operates in semiconductors with and without a center inversion symmetry, although it is most prominent in the centrosymmetric ones (*e.g.* Si). The EY spin relaxation rate (τ_s^{EY}) for electrons with energy E is proportional to the electron momentum scattering rate (τ_p^{-1}), and is given by [34],

$$\frac{1}{\tau_s^{EY}}(E) = A\left(\frac{E}{E_g}\right)^2\left(\frac{\Delta}{E_g+\Delta}\right)^2\frac{1}{\tau_p(E)} \tag{1.13}$$

where A is dimensionless constant, Δ is the spin-orbit splitting of the valence band, and E_g is the bandgap of the semiconductor. The above equation indicates that EY mechanism is prevalent in small bandgap and large spin-orbit coupling semiconductors.

The DP mechanism is dominant in semiconductors without a center of symmetry, such as zinc-blende (*e.g.* GaAs) structures. In such semiconductors, the spin-orbit interaction manifests itself as an effective, momentum dependent magnetic field. An electron moving with one velocity feels one effective magnetic field along which the electron's spin precesses. As the electron is scattered by an impurity or a phonon, the electron changes its velocity and it feels a different (in both magnitude and direction) spin-orbit magnetic field. The precession axis and frequency changes randomly. The spin takes a random walk and spin-flip occurs if the spin manages to walk as far as the opposite direction. Unlike the EY mechanism, the spin relaxes in between the scattering events. The more the scattering events, the less is the spin relaxation. The DP relaxation rate is given by [35],

$$\frac{1}{\tau_s^{DP}(E)} = Q\alpha^2\frac{E^3}{\hbar^2 E_g}\tau_p(E) \tag{1.14}$$

The DP process dominates in middle bandgap semiconductors and at high temper-

atures for systems with sufficiently low hole densities.

The BAP mechanism dominates in p-doped semiconductors. Exchange interaction between electrons does not lead to spin relaxation as it preserves the total spin. However, in a p-doped semiconductor there will be exchange coupling with holes. A spin-up electron will exchange its spin with a spin-down hole. The total spin is preserved in the process. However, holes lose their spins very fast, since the valence bands are strongly spin mixed due to spin-orbit coupling. The EY mechanism then leads to very fast spin relaxation of holes. Holes then act as a reservoir for spin. Spin polarized carriers will dump their spin into this reservoir, in which the spin polarization quickly becomes zero [36]. The BAP relaxation rate increases with the degree of electron and hole spatial overlap, which increases at lower temperatures and for larger confining potentials, as in the case of QWs and QDs.

In the presence of nuclear spins, hyperfine interaction is capable of spin-flips. This interaction will be motionally narrowed for itinerant electrons. Electrons will move past through nuclei with random spins and the resultant effect will be negligible. However for quantum confined electrons (*e.g.* electrons in QDs), the electron wave function will spread over a region containing many nuclear spins. The hyperfine interaction can therefore flip electron spin causing spin dephasing.

Optical orientation time-resolved Faraday rotation spectroscopy have both been used to measure the spin relaxation time in bulk n-type GaAs [16, 37]. A summary of the studies is given in Fig. 1.8.

1.3.3 Spin Detection

Spin polarization in a semiconductor can be detected optically or electrically. The optical detection technique is used in spin-LEDs and spin-lasers, while the spin-based electronic devices use electrical detection.

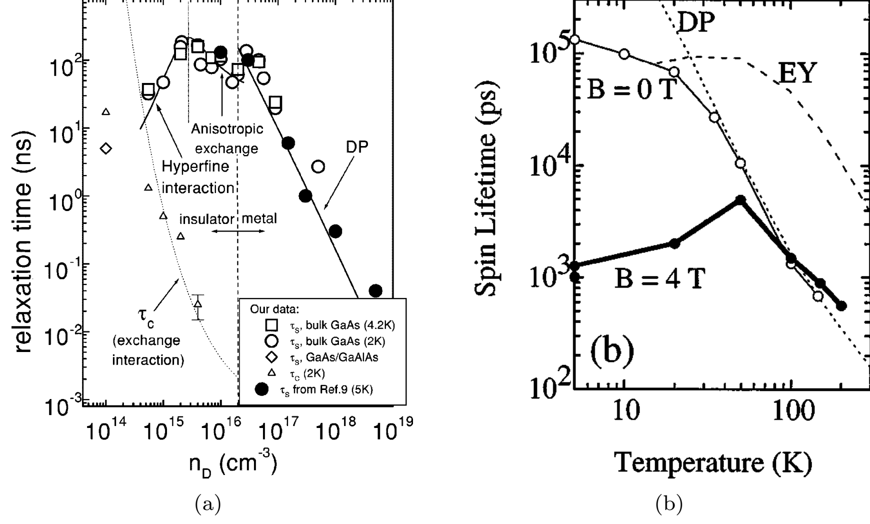

Figure 1.8: Spin relaxation time in n-type GaAs as a function of (a) donor density at low temperatures (<5 K) and (b) temperature.

Optical Detection – In optical detection, spin polarized electrons radiatively recombine with unpolarized holes emitting circularly polarized light. The spin polarization is directly related to the optical polarization of the emission through quantum selection rules governing recombination. The right- and left- circularly polarized photons have an angular momentum of +1 and -1, respectively, in the direction of the wave vector. Since the total angular momentum must be conserved, electron-hole recombination, which leads to a angular momentum change of -1 (+1), emits right(left) circularly polarized photon. Figure 1.9 shows the possible interband transitions and corresponding optical polarization for the cases of bulk material and quantum well [38]. Quantum mechanically it can be shown that transitions involving heavy hole states are three times more probable than those involving light hole states. In a bulk direct bandgap semiconductor, the heavy hole and light hole valence bands are degenerate at the Γ-point. When taken together with the relative transition probabilities, the spin polarization (Π_{inj}) of electrons and the output circular polarization

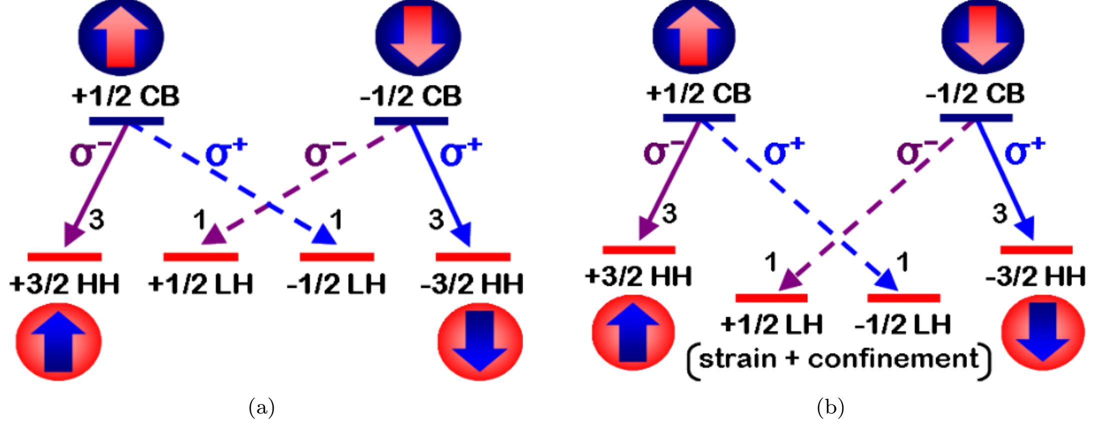

Figure 1.9: Electric dipole allowed radiative interband transitions and corresponding optical polarization for the cases of (a) bulk material with degenerate heavy- and light-hole bands and (b) a quantum well in which epitaxial strain and quantum confinement have lifted the heavy- and light-hole band degeneracy.

(Π_{CP}) are related as,

$$\Pi_{CP} = \frac{I(\sigma^+) - I(\sigma^-)}{I(\sigma^+) - I(\sigma^-)} = \frac{(3n_\downarrow + n_\uparrow) - (3n_\uparrow + n_\downarrow)}{(3n_\downarrow + n_\uparrow) + (3n_\uparrow + n_\downarrow)} = \frac{n_\downarrow - n_\uparrow}{2(n_\downarrow + n_\uparrow)} = -\frac{\Pi_{inj}}{2} \quad (1.15)$$

where $I(\sigma^+)$ and $I(\sigma^-)$ are the intensities of right circularly (σ^+) and left circularly (σ^+) polarized light, respectively. In a strained quantum well (QW) system the degeneracy between the heavy hole and light hole bands is lifted. For compressively strained system, the heavy hole band is higher energetically than the light hole band. The radiative recombination involving heavy hole transitions are predominant in this case. Hence, the relation between output circular polarization and spin-polarization is given by,

$$\Pi_{CP} = \frac{I(\sigma^+) - I(\sigma^-)}{I(\sigma^+) - I(\sigma^-)} = \frac{3n_\downarrow - 3n_\uparrow}{3n_\downarrow + 3n_\uparrow} = \frac{n_\downarrow - n_\uparrow}{n_\downarrow + n_\uparrow} = -\Pi_{inj} \quad (1.16)$$

Hence the output circular polarization is a direct measure of the electron spin polarization in this case.

Electrical Detection in Nonlocal Geometry – Electrical detection of spin polarization is very similar to the electrical spin injection. The only difference is that the direction of current is reversed now. For the similar reason as in the case of spin

injection, a ferromagnet/insulator/semiconductor tunnel barrier is used for spin detection. A schematic of the nonlocal geometry used for spin detection is shown in Fig. 1.10 [19, 20, 39]. A current bias is sent between two ferromagnetic contacts

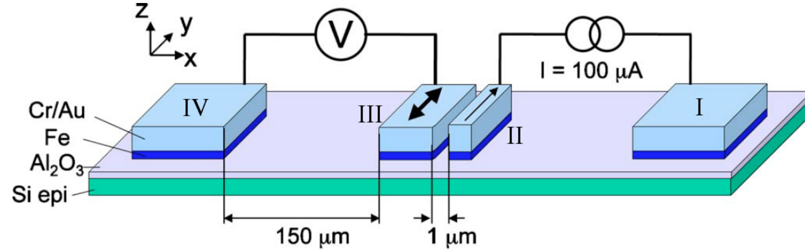

Figure 1.10: A four terminal nonlocal geometry for spin accumulation measurement.

(source and drain) which create a charge current and spin current in the semiconductor. The charge current is confined between the source (I) and drain (II) terminals, however the spin current diffuses further beneath the third (III) ferromagnetic contact. The spin polarization beneath the third contact is therefore nonzero. The fourth (IV) contact is placed far away from the other contacts. The spin polarization is zero at this contact due to spin relaxation. Hence, the fourth contact serves as the ground potential. A voltage is generated between the third terminal and the ground potential, which measures the nonlocal voltage due to spin accumulation. The nonlocal voltage measured by the third contact with respect to the ground potential can be determined by considering the resistor model for the spin selective tunnel junction, shown in Fig. 1.11 [27]. By considering the fact that zero charge current flows through the nonlocal terminal, the measured voltage is given by,

$$\mu_F = \frac{P(\mu_\uparrow - \mu_\downarrow)}{2} + \frac{(\mu_\uparrow + \mu_\downarrow)}{2} \quad (1.17)$$

where P is the spin polarization at the nonlocal terminal. The second term in Eqn. 1.17 is the voltage measured by the fourth contact. Usually $(\mu_\uparrow + \mu_\downarrow) = 0$ as the fourth contact is connected to the ground. The ferromagnet/insulator/semiconductor

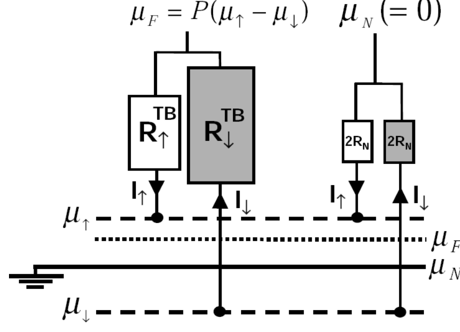

Figure 1.11: Resistor model of ferromagnet/insulator/semiconductor tunnel junction. The ferromagnetic voltage probe is weakly coupled to the spin-up and spin-down electron population in the semiconductor region. The short-circuiting resistance $2R_N$ represent the spin relaxation due to the nonmagnetic voltage probe strongly coupled to the semiconductor.

is an ideal spin detector as long as the spin current flowing from ferromagnetic voltage probe via the tunnel barrier into the semiconductor is negligible.

Electrical Detection through Spin Precession – A magnetic field $B_\perp$ exerts a torque on a spin given by,

$$T = -\mu_B B_\perp \sin\theta \tag{1.18}$$

where θ is the angle between the electron spin and the magnetic field directions. Usually the magnetic field is applied in the perpendicular direction ($\theta = 90°$) to avoid spurious effects from in plane magnetic field contribution. The torque T makes the electron spin precess, a phenomenon known as Larmor precession. The precession (Larmor) frequency is given by,

$$\omega_L = -\frac{g\mu_B B_\perp}{\hbar} \tag{1.19}$$

An electron injected from the source will acquire an angle of $\phi = \omega_L t$ before it reaches the drain, where t is the time of travel. The spin detector detects the spin projection onto its own magnetization direction. The spin accumulation signal will therefore be modulated by $\cos\phi$. A typical geometry for spin precession measurement and the modulated spin signal is shown in Fig. 1.12 [27]. The spin valve signal will

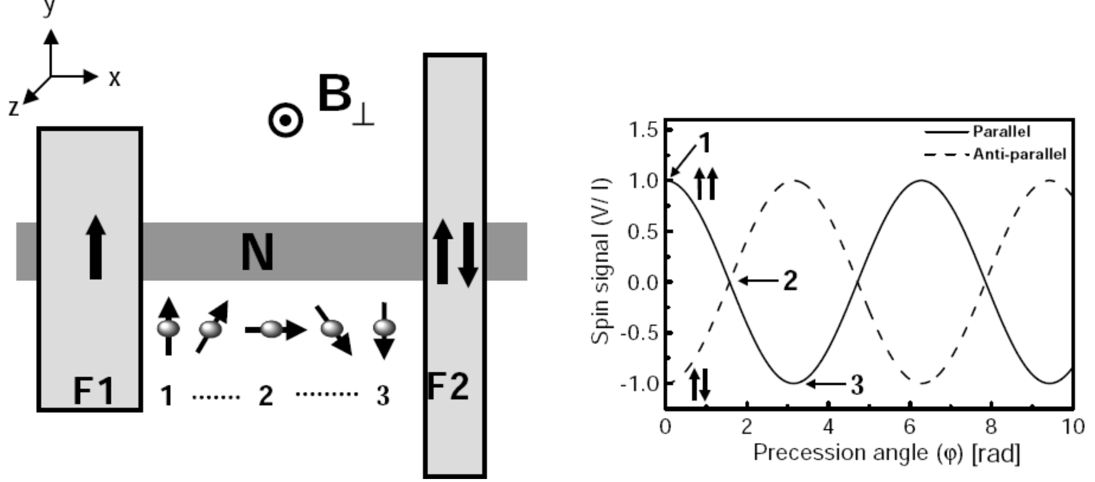

Figure 1.12: Measurement geometry for spin precession measurement and the oscillatory modulation of spin signal.

be oscillatory with fixed amplitude if the transport is ballistic and there is no spin relaxation during precession. However, the time of travel in a diffusive conductor has broad distribution due to the statistical nature of the process, which is given by,

$$\varphi(t) = \frac{1}{\sqrt{(4\pi Dt)}} \exp\left(-\frac{L^2}{4Dt}\right) \tag{1.20}$$

where D is the spin diffusion constant and L is the average distance traveled by the electrons. The output voltage, in this case, for a fixed current bias I becomes,

$$V(B_\perp) = \pm I \frac{P^2}{e^2 N(E_F) S} \int_0^\infty \varphi(t) \cos(\omega_L t) \exp\left(-\frac{t}{\tau_{sf}}\right) dt \tag{1.21}$$

where $N(E_F)$ is the density of states at the Fermi energy level (E_F), τ_{sf} is the spin relaxation time and S is the cross sectional area of the detector. The (+) and (–) sign correspond to the parallel and antiparallel magnetization of source (F1) and drain (F2), respectively. The polarization P can be very accurately determined from Eqn. 1.21.

1.4 Thesis Organization

The central theme in this thesis is to demonstrate some of the most fundamental *semiconductor spintronic* devices which can serve as a benchmark for future devices. The thesis also studies spin injection, transport and detection is various ferromagnet/semiconductor heterostructures. The thesis organization is as follows:

- We have demonstrated, for the first time, electrical spin injection and detection in a ferromagnet/semiconductor based lateral spin-valve. We have used a MnAs/GaAs Schottky tunnel barrier for spin injection and detection. Chapter II describes the detailed characterization of these devices.
- We have conceived and demonstrated a spin-current amplifier to alleviate the problem of low spin-polarization in semiconductors. Chapter III describes the results from this unique device and its unique characteristics.
- Spin transport is a very important aspect in semiconductor spintronic devices. Chapter IV discusses the study on generalized two dimensional spin-transport in a multi-terminal lateral geometry.
- We have observed a new phenomenon involving electrically driven spin dynamics of paramagnetic impurities. The phenomenon has led us to the realization of a spin capacitor. Chapter V describes the design, growth, fabrication and characterization of spin capacitors.
- We have demonstrated a quantum dot (QD) spin-VCSEL operating at 200 K. Chapter VI depicts the polarization and threshold current characteristics of this device.
- Electrical modulation of circular polarization of light sources is a very desirable feature for communication applications. It helps to double communication

bandwidth. Chapter VII describes results from the theoretical and experimental study of the polarization modulation of spin-VCSELs.

- One of the major advantages of spintronic devices is that they have the potential to be integrated with other conventional devices. We have demonstrated a monolithically integrated magneto-opto-electronic integrated circuit (MOEIC) which acts as a magnetoelectronic switch. Chapter IX describes the design, fabrication and characterization of MOEIC.

Finally, the conclusions of this present research are outlined in Chap. IX, along with some suggestions for future work.

CHAPTER II

Epitaxially Grown MnAs/GaAs Lateral Spin-Valves

2.1 Introduction

Efficient electrical injection of spin-polarized carriers into semiconductors from a ferromagnetic contact is a very challenging research field [26,40]. Spin injection in a lateral geometry is favored over more ubiquitous vertical structures used in tunneling magnetoresistance devices [41,42] since lateral structures offer a larger degree of freedom in their fabrication and the possibility of integration with other conventional lateral semiconductor devices for the realization of MOEIC. All-metal lateral spin valves fabricated by electron-beam lithography have already been demonstrated [43, 44]; however, semiconductor-based lateral spin valves with ferromagnetic contacts serving as the injector and collector have remained elusive [45, 46]. Here, we provide evidence of spin injection and collection in a hybrid ferromagnet-semiconductor heterostructure with a lateral device geometry. A peak magnetoresistance of 3.6% at 10 K and 1.1% at 125 K is measured for a 0.5 μm channel length lateral spin-valve. The variation of magnetoresistance with channel length, bias, and temperature has been studied in detail. A maximum spin polarization of 31.5% is observed at the source end in these devices. The results are explained in the framework of spin injection, transport, and collection along with micromagnetic simulations.

2.2 Origin of Magnetoresistance

A lateral spin-valve consists of a ferromagnetic polarizer contact, a non-magnetic GaAs channel region, and a ferromagnetic analyzer contact. The polarizer and analyzer have different coercivities so that it is possible to have parallel (P) and anti-parallel (AP) magnetization configurations between them by applying an appropriate external magnetic field. When a voltage bias is applied spin-polarized carriers are injected from polarizer into the GaAs channel through a Schottky tunnel barrier. The carriers traverse through the non-magnetic channel region and reach the analyzer contact. If the spin-scattering in the channel region is small, the carriers from polarizer contact will reach the analyzer with non-zero spin-polarization. The carriers will be efficiently (inefficiently) collected by the analyzer if it has the same (opposite) direction of magnetization as the polarizer and the current will be large (small). This gives rise to the spin-valve effect (magnetoresistance) in a ferromagnet/non-magnet/ferromagnet lateral device. The effective resistance of such a device is small when they are magnetized in the same direction, and large when magnetized in opposite directions.

The operation of a spin-valve can be described by a two-channel model shown in Fig. 2.1. The spin-up and spin-down currents form two independent channels for

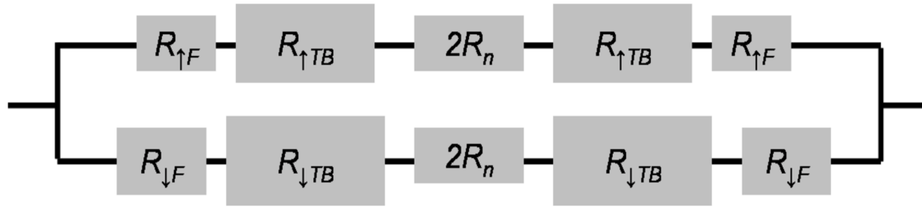

Figure 2.1: A schematic of the two-channel model for a conventional lateral spin-valve.

current conduction, assuming negligible spin-flip in the channel region. The resis-

tances of the ferromagnet, spin selective Schottky tunnel barrier and semiconductor channel are denoted by R_F, R_{TB} and R_n, respectively. The spin-up and spin-down channels are indicated by $\uparrow$ and $\downarrow$, respectively, in the suffix. It can be shown that the magnetoresistance (MR) of a small channel length spin-valve is given by,

$$MR = \frac{R_{AP} - R_P}{R_{AP}} = \frac{(\beta - 1)^2}{4\beta} \tag{2.1}$$

where $\beta = R_{\downarrow TB}/R_{\uparrow TB}$ is the spin selectivity of the tunnel barrier (Appendix A). Hence, magnetoresistance of an ideal spin-valve primarily depends on the spin selectivity of the tunnel barrier. Equation 2.1 provides a method to determine the spin selectivity of a tunnel barrier from channel length dependent magnetoresistance measurement.

In summary, the spin-valve devices operate on the principle that the polarizer, maintained at a negative bias with respect to the analyzer, injects electron spins predominantly of one spin orientation, which are subsequently detected by the analyzer. The polarizer and analyzer efficiencies change to a different extent with changing magnetic field (H) by virtue of their different coercivities, which is manifested as a change in resistance.

2.3 Growth and Fabrication of Spin-Valves

The spin-valve heterostructures are grown by molecular-beam epitaxy on semi-insulating GaAs(001) substrates (Fig. 2.2). A 150 nm Si-doped n-GaAs channel layer is grown at 600 °C, followed by a 30 nm graded doping n^+-GaAs contact layer grown at the same temperature, after which the substrate temperature is ramped down for ferromagnetic MnAs deposition. The doping concentration (N_D) profile along the vertical cross section as estimated from growth conditions is shown in Fig. 2.2. The narrow heavily doped region beneath MnAs creates a triangular tunnel contact,

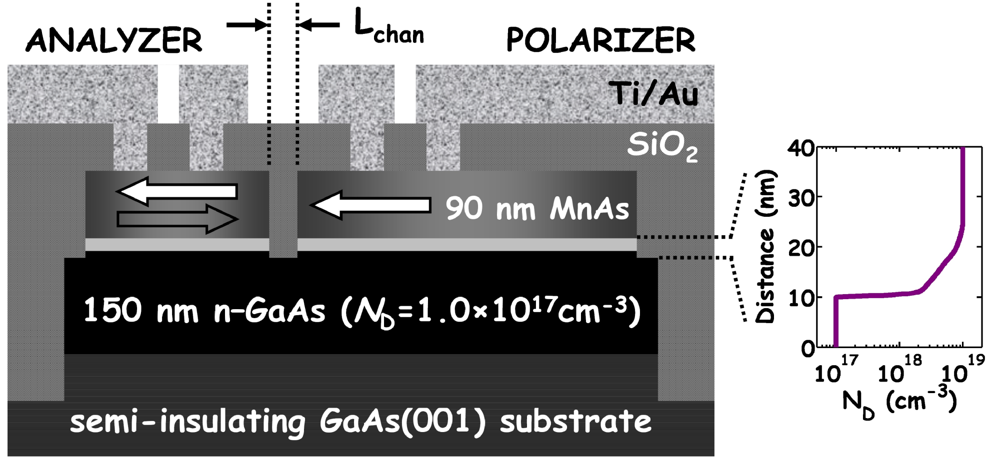

Figure 2.2: A schematic cross section of a MnAs/GaAs lateral spin valve. Analyzer and polarizer are formed by pattering them on MnAs. The vertical n-doping profile in the channel is also shown.

increasing the spin-injection efficiency and alleviates the problem of conductivity mismatch [18,47]. The channel doping ($N_D = 1 \times 10^{17}$ cm^{-3}) is optimized to ensure a large spin-relaxation time at low temperatures [37]. It is well known that two orientations of MnAs may be realized on GaAs(001) substrates depending on the growth conditions during nucleation [48]. For the present work, we select an As-rich template for growth of a 90 nm type-A MnAs film, which yields the following epitaxial relationship: $[\overline{11}20]$MnAs $\parallel$ [110]GaAs and [0001]MnAs $\parallel$ $[\overline{1}10]$GaAs. A very low growth rate (10 nm/h) and substrate temperature (200 °C) are used during growth of the first few monolayers of MnAs. After the nucleation phase, the growth rate and substrate temperature are both increased to 40 nm/h and 250 °C, respectively. An in situ anneal under an As_4 flux is performed at 350 °C to improve the structural and magnetic properties of the MnAs film. The thickness of the MnAs film (90 nm) is chosen appropriately so as to maximize the saturation magnetization and suppress the formation of cracks which complicate device fabrication. Measurements using superconducting quantum interference device (SQUID) magnetometry yield

coercivities of 210 Oe along the easy magnetization axis [110] and 2.8 T along the hard axis [$\bar{1}$10] of an as-grown unpatterned sample, which are comparable to those reported by others [49, 50].

Lateral spin valves of channel lengths L_{chan} = 0.5, 0.7, 1.0, and 1.5 μm with polarizer (P) and analyzer (A) contact length-to-width aspect ratios (L/W) of 10 and 2, respectively, are fabricated. The devices are fabricated in the following steps:

I. Mesa – The MnAs layer, n^+-GaAs heavily doped region, n-GaAs channel region and 100 nm of the GaAs buffer layer are etched away by using $H_3PO_4/H_2O_2/H_2O$ (1:1:10) solution for 120 s.

II. Source and drain – The MnAs layer and n^+-GaAs heavily doped region are etched away from mesa by using $H_3PO_4/H_2O_2/H_2O$ (1:1:100) solution for 45 s to form source and drain regions.

III. Vias – A 300 nm SiO_2 layer is deposited by low-temperature plasma enhanced chemical vapor deposition (PECVD) for passivation. Vias are etched on source and drain contacts by reactive ion etching (RIE) of SiO_2.

IV. Interconnect and metallization – Thin films of Ti/Au (20/300 nm) are deposited by physical vapor deposition (PVD) for interconnect and metallization.

A scanning electron microscope (SEM) image of a 0.5 μm channel length spin-valve is shown in Fig. 2.3

SQUID magnetometry measurements as well as finite difference micromagnetic simulations [51] using parameters optimized for our growth conditions confirm that a coercive field difference is readily obtained by varying the MnAs contact aspect ratio. The following three control devices are also fabricated to conclusively confirm spin-valve behavior in devices with different contact aspect ratios: (1) symmetric devices with L_{chan} = 0.5 μm and identical aspect ratios for both contacts

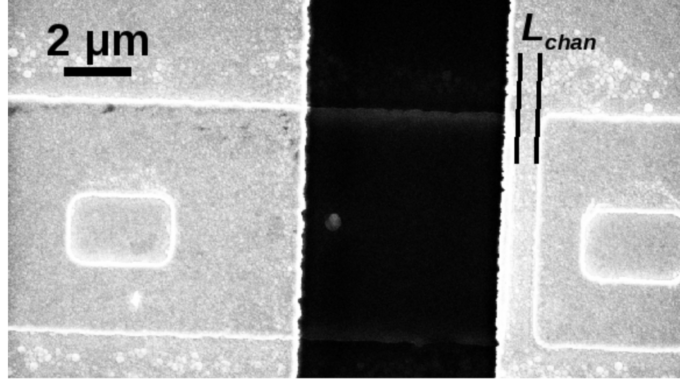

Figure 2.3: An SEM image of a 0.5 μm channel length lateral spin-valve.

$[(L/W)_A=(L/W)_P = 2]$, (2) ferromagnetic MnAs/non-magnetic GaAs/nonmagnetic GaAs (FM/NM/NM) lateral devices with $L_{chan} = 0.5$ μm, and (3) nonlocal [43] spin valves with $L_{chan} = 1$ μm. Devices identical to the lateral spin valves without the nonmagnetic GaAs channel are also fabricated to estimate the contribution from anisotropic magnetoresistance (AMR) to the overall magnetoresistance.

2.4 MnAs/GaAs Tunnel Barrier Characteristics

Electrical injection efficiency of spin polarized carriers into semiconductor is very poor due to large conductivity mismatch between ferromagnet and semiconductor, as described in Sec. 1.3.1. This problem is solved by using tunnel injection of spin polarized carriers. The GaAs beneath the MnAs contact pads is very heavily doped, creating Schottky tunnel barriers for efficient spin injection. In an FM/NM/FM lateral device, the reverse biased FM/NM junction injects a spin polarized current, however the collector junction (FM/NM) is forward biased leading to relatively inefficient detection. The magnetoresistance of the devices is mainly limited by the detection efficiency. To ensure that tunneling is the dominant mechanism for electron transport at the junctions, the following modified Rowell criteria [52] are satisfied – (1) the zero-bias tunnel resistance has very weak temperature dependence; and

(2) the conductance has parabolic voltage dependence. The zero-bias resistance as a function of temperature for MnAs/GaAs junction is shown in Fig. 2.4. It can be

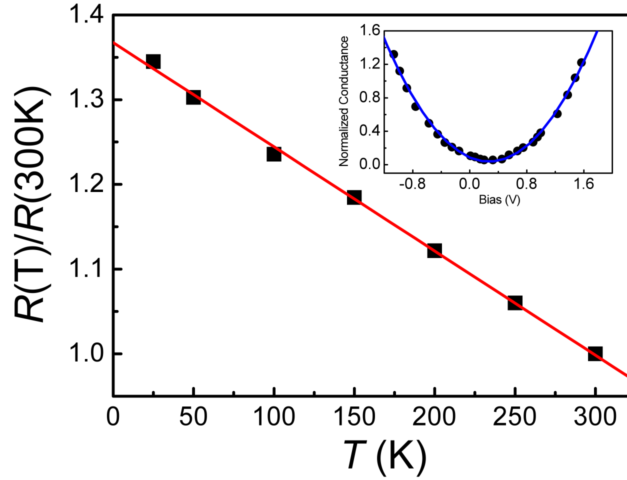

Figure 2.4: Zero-bias normalized resistance as a function of temperature for the MnAs/GaAs (FM/NM) tunnel junction. The measured conductance as a function of bias and the corresponding parabolic fit are shown in the inset.

seen that the resistance has very weak dependence on temperature. The measured conductance as a function of bias is shown in the inset of Fig. 2.4. A parabolic fit to the experimental data is shown alongside, which matches well with the experimental data. These characteristics confirm tunneling mechanism at the MnAs/GaAs junctions. The average tunnel barrier height (ϕ) and tunneling distance (d), as calculated from the conductance measurement and using the Brinkman-Dynes-Rowell model [53], are found to be 0.9 eV and 2 nm, respectively.

2.5 Magnetoresistance of Spin-Valves

The magnetoresistance, defined as $MR(H) = [R_{AP}(H_{sat}) - R_P(H)]/R_P(H_{sat})$, of the spin valves and control devices are measured for various L_{chan}, temperatures (T), and bias conditions (I_B) using a standard four-probe alternating current (ac) lock-in technique. Figure 2.5 shows magnetoresistance for spin valves having different (asymmetric) and identical (symmetric) aspect ratios of the ferromagnetic contact

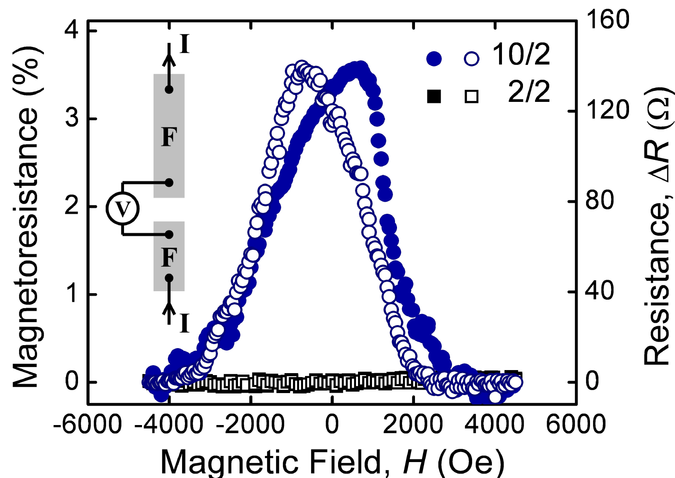

Figure 2.5: Magnetoresistance and resistance changes at 10 K as a function of applied magnetic field for a 0.5 μm channel length conventional spin valve biased at 5.5 mA. The spin valve is shown schematically in the inset. The legend indicates the length-to-width aspect ratio for the polarizer/analyzer. Open and closed symbols represent the cases of descending and ascending magnetic fields, respectively.

pads with $L_{chan} = 0.5$ μm at $T = 10$ K and $I_B = 5.5$ mA. The magnetoresistance for the asymmetric device peaks at 3.6% for |H| $\approx$ 700 Oe in both directions of the magnetic field sweep. The magnetoresistance peaks correspond to antiparallel magnetization of the MnAs pads arising from their coercive field difference. The change of magnetoresistance with magnetic field is gradual, and the change is very large even before there is any substantial change in net contact magnetization. Micromagnetic simulations of our device and the orientation of magnetic domains at the edge of the ferromagnetic contacts, which are the domains responsible for spin injection, at different points of the corresponding hysteresis are shown in Fig. 2.6. It is found that the domains at the very near edge of the channel start responding to H much earlier (even before $H = 0$) [54], but owing to their small contribution to the overall magnetization it is not observable in the hysteresis data. This explains the discrepancy between the magnetoresistance plot and SQUID magnetization data. Furthermore, the gradual rotation of domains explains the gradual change in magnetoresistance

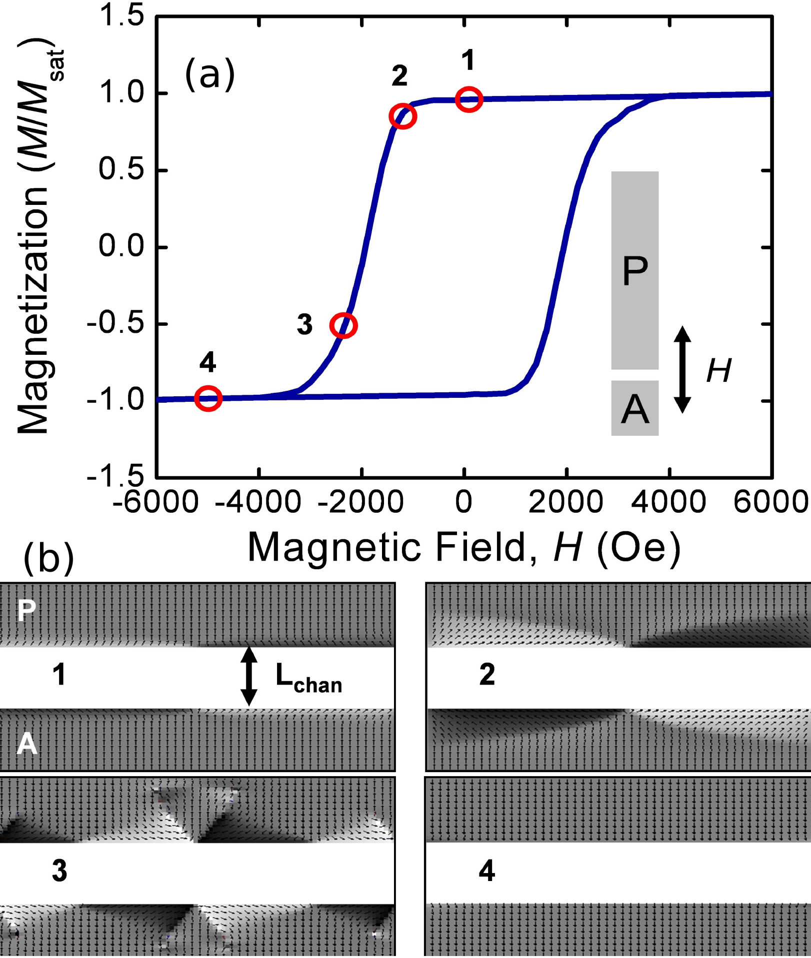

Figure 2.6: Polarizer and analyzer magnetization characteristics. (a) Hysteresis loop of the contact pads and (b) simulated magnetic domain patterns for a MnAs/GaAs spin valve at different positions along the hysteresis. A zoomed view of the domain patterns near the channel is shown for each case. The inset to (a) shows a schematic depiction of the simulated spin valve with a 10×5 μm^2 analyzer (A) and 50×5 μm^2 polarizer (P).

with H. There is no noticeable magnetoresistance (peak $MR \approx 0.04\%$ and $\Delta R_{peak} \approx$ 3.5 mΩ at $H = 0$) for the symmetric device which demonstrates the spin-valve effect in our devices.

2.6 Characteristics of Control Devices

Magnetoresistance measurements are done on control devices to ensure spin dependency of the observed effect. Magnetoresistance of the FM/NM/NM lateral devices are found to be negligible ($\sim$ 0.02%) confirming that the magnetoresistance

in FM/NM/FM devices is due to the spin-valve effect only. The measured magnetoresistance of the nonlocal spin valve as a function of magnetic field is shown in Fig. 2.7. The nonlocal spin valve removes the AMR contribution and the Hall effects

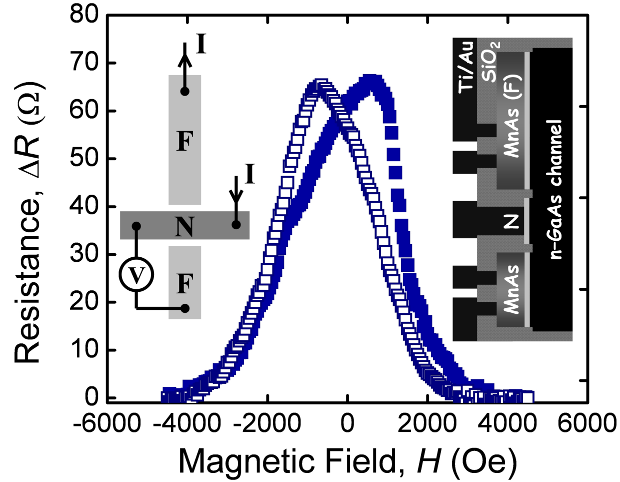

Figure 2.7: Resistance change as a function of applied magnetic field for a 1 μm channel length nonlocal spin valve. Top- and side-view schematics of the nonlocal spin valve are shown in the inset. Open and closed symbols represent the cases of descending and ascending magnetic fields, respectively.

of the ferromagnetic electrodes [43]. The magnetoresistance for the nonlocal spin valves show a similar change with varying magnetic field as the conventional spin valve. A $\Delta R_{peak} \approx 66\ \Omega$ is measured for a $L_{chan} = 1\ \mu$m nonlocal spin valve under the same operating conditions as for the conventional spin valve. This value is 2.3 times smaller, compared to the theoretically predicted factor of 2 for a transparent barrier [43], than the value measured for a similar conventional spin valve. We have not observed any difference between the shapes of the ΔR curves in the two cases, which indicates that any stray AMR contribution that might be present is too small to appear considering the magnitude of the magnetoresistance measured in the above cases. To precisely estimate the anomalous AMR contribution, magnetoresistance measurements are done on a strip of MnAs contact ($L/W = 12$) fabricated identically to the conventional spin valve but without a GaAs channel. Figure 2.8 shows

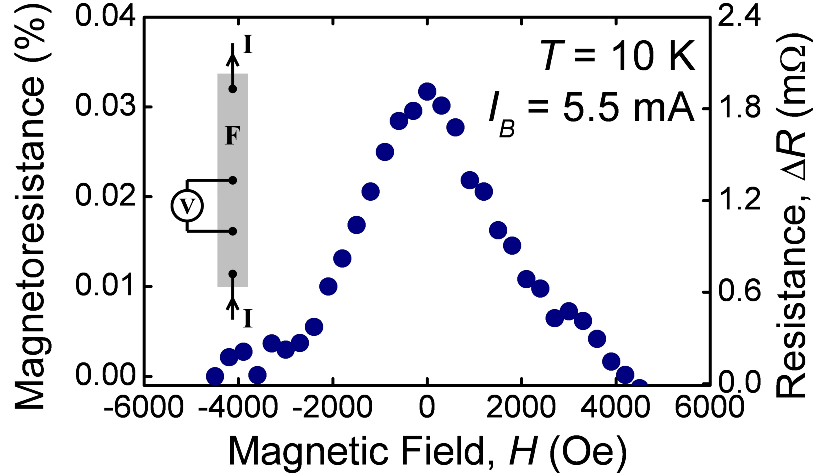

Figure 2.8: Magnetoresistance and resistance changes due to stray effects of a single MnAs strip contact, which is shown schematically in the inset.

the MR for such a device under identical bias conditions as for the conventional spin valve. The measured $\Delta R_{peak} \approx 3$ mΩ at zero magnetic field is five orders of magnitude smaller than the value measured for the spin valve. This explains the similarity of the shape of the curves observed in conventional and nonlocal spin valves. The near-zero response (Fig. 2.5) measured for the symmetric spin valves indicates that the magnetoresistance in these devices result from stray effects.

2.7 Characteristics of Magnetoresistance

Figure 2.9(a) shows that the peak magnetoresistance for the conventional spin valve varies exponentially with L_{chan}, which indicates that spin transport is diffusive in the channel [17, 55]. As L_{chan} is decreased, the number of spin-polarized electrons that reach the analyzer before spin relaxation increases, yielding a larger peak magnetoresistance. Figure 2.9(b) shows the temperature dependence of the peak MR under different bias voltages. Five spin valves across various grown and processed samples with $L_{chan} = 1.0$ μm are measured under identical experimental conditions, and the results are highly reproducible. The peak magnetoresistance increases with decreas-

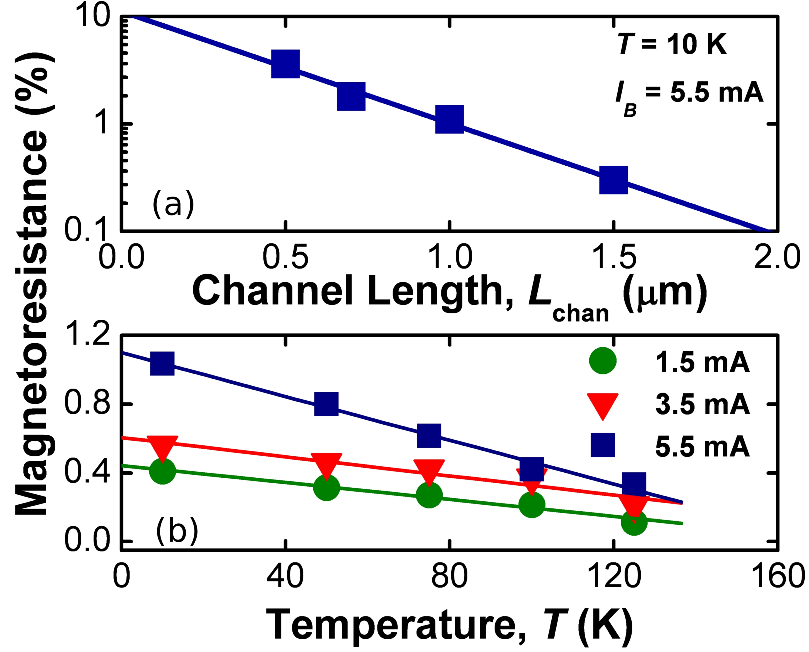

Figure 2.9: Magnetoresistance characteristics. (a) Peak magnetoresistance vs channel length measured at 10 K, (b) peak magnetoresistance vs temperature for a 1 μm spin-valve with applied biases of I_B = 1.5, 3.5, and 5.5 mA. The lines represent a linear least squares fit to the data.

ing temperature for a fixed bias voltage due to increase in average spin-relaxation time and hence spin-flip length. The increase in magnetoresistance with bias, contrary to theoretical predictions [56], can be explained by considering the effect of spin injection through a tunnel barrier at higher bias values. The effective tunneling distance for the electrons to tunnel through decreases with increasing bias, leading to efficient spin injection from the polarizer. In contrast the analyzer efficiency does not change much with bias. This leads to the overall increase in magnetoresistance at high bias. However, magnetoresistance values higher than those shown in Fig. 2.9 could not be attained since most of our devices suffered breakdown for an applied current bias greater than 5.5 mA.

Expected spin injection and magnetoresistance values at T = 10 K and I_B = 5.5 mA for a 0.5 μm channel length spin valve, calculated using the simple diffusive

injection model in Ref. [17] with experimentally determined values for the model parameters and appropriate value for bulk spin polarization from Ref. [50], are found to be 0.04% and $< 0.01\%$. The value of magnetoresistance ($\sim 3.6\%$) measured in this study is much larger, which indicates efficient spin-polarized carrier injection by tunneling through the Schottky barrier in our devices. Large spin-injection efficiencies of 32% have also been reported for similar Fe/AlGaAs Schottky tunnel barrier contacts as determined from the electroluminescence polarization of spin-polarized light-emitting diodes [21].

2.8 Spin-Selectivity of Tunnel Barrier and Channel Spin Polarization

The spin-selectivity of the tunnel barrier (β) and the spin-polarization in the channel region are determined by using the two-channel model described earlier. The magnetoresistance is extrapolated for $L_{chan} \to 0$ in Fig. 2.9. magnetoresistance for $L_{chan} = 0$ is estimated to be 11%. Equation 2.1 is then used to determine $\beta = 1.92$. It can be shown by using the two-channel model that the spin-polarization (Π_s) just beneath the source contact is given by (Appendix A),

$$\Pi_s = \frac{\beta - 1}{\beta + 1} \tag{2.2}$$

which is determined to be 31.5% for MnAs/GaAs spin-valve. The spin-polarization of MnAs is $\Pi_{\mathrm{MnAs}} \sim 0.5$ [50]. Hence, the efficiency of the Schottky tunnel barrier is, $\Pi_s/\Pi_{\mathrm{MnAs}} \approx 0.6$.

2.9 Conclusion

In summary, we have conclusively demonstrated the spin-valve effect in a lateral MnAs/GaAs device for the first time and have investigated the temperature, bias,

and channel length dependence of the observed magnetoresistance. A peak magnetoresistance of 3.6% is observed at 10 K in a 0.5 μm channel length spin valve, and a finite magnetoresistance can be seen for temperatures up to 125 K. These results provide experimental verification of spin injection and collection in a lateral structure and can serve as a benchmark for future spin-based devices.

CHAPTER III

Amplification of Spin-Current Polarization

3.1 Introduction

Electrical injection and control of large spin polarization in semiconductors are indispensable for the realization of useful spintronic devices [26, 40]. Electrical spin injection has been demonstrated in all-metal devices [14, 57, 58], ferromagnet/semiconductor based lateral spin-valves [19, 20, 45], and also electrically injected spin-polarized lasers [59]. Despite these advances, achievement of current spin polarizations of 100%, or more, and electrical control of such polarizations have remained elusive. An electrically controlled spin-current amplifier is a desirable solution to this problem. Theoretical proposals for such devices have been made [60–66], but experimental demonstration is lacking. Here we propose and demonstrate a novel electrically controlled three terminal spin-polarization amplifier using a dual-drain lateral spin-valve configuration, which can provide large current spin polarization for both majority and minority spins, independent of the injected (source) polarization. The device amplifies the small injected polarization in a semiconductor channel to a large value, which can be extracted at the second drain contact. The sign and magnitude of the amplifier gain can be controlled both at the input and output terminals to achieve a desired polarization. The device also generates a pure spin-current with

zero charge current. This aspect can be used to envisage a new class of spintronic devices.

3.2 Design of a Spin-Current Amplifier

When a current flows in a ferromagnet/semiconductor/ferromagnet lateral spin-valve, the electrochemical potentials of spin-up ($\mu_\uparrow$) and spin-down ($\mu_\downarrow$) electrons split in the semiconductor channel. The splitting ($\Delta\mu = \mu_\uparrow - \mu_\downarrow$) depends on the relative directions of magnetization of the two ferromagnetic contacts. It is large when the two contacts (we call them source and drain1) are magnetized in opposite directions, and small (with a crossover in the center) when the contacts are magnetized in the same direction. If a point contact (drain2) is then placed at the center of the semiconductor channel (L_{chan}) of the spin-valve with anti-parallel magnetization of source and drain1 contacts, its potential can be varied between $\mu_\uparrow$ and $\mu_\downarrow$, enabling a controlled collection of spin-up and spin-down electrons. It is important to note that the two spin-currents flow in opposite directions and the current polarization can be controlled by varying the drain2 bias. It is necessary to ensure that the drain2 contact acts as a high-impedance probe, so as to minimize any perturbation of the channel potentials.

A simple two-channel model for the spin-current amplifier is shown in Fig. 3.1 The source and drain1 ferromagnetic contacts are magnetized in opposite directions. The spin-up (spin-down) conductivities of the ferromagnet and the tunnel barrier are shown as $R_{\uparrow F}$ ($R_{\downarrow F}$) and $R_{\uparrow TB}$ ($R_{\downarrow TB}$), respectively. The resistance of the semiconductor channel is R_n. The ideal drain2 point contact is at the center of the semiconductor channel. The electrochemical potentials for spin-up ($\mu_\uparrow$) and spin-down ($\mu_\downarrow$) electrons are split at $x = 0$. The drain2 voltage V_{D2} can be varied between $\mu_\uparrow$

and $\mu_\downarrow$ enabling a controlled collection of spin-up and spin-down electrons. The two spin-currents $I_{D2\uparrow}$ and $I_{D2\downarrow}$ can flow in opposite directions depending upon the value of V_{D2}, yielding spin polarization gain greater than unity.

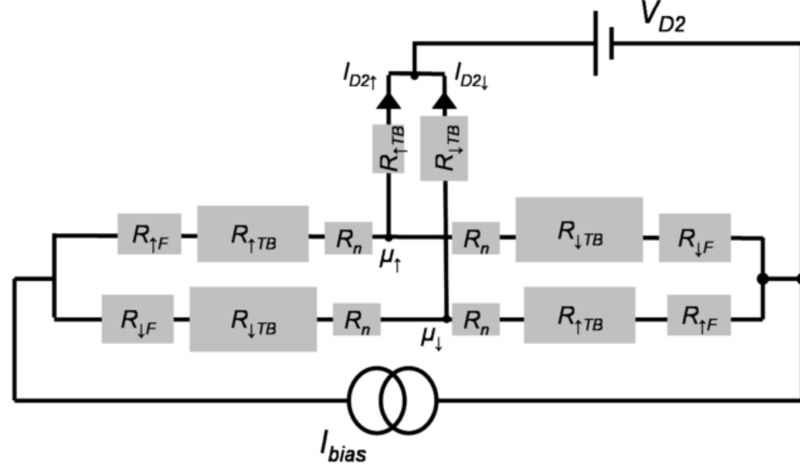

Figure 3.1: The two-channel model for the spin polarization amplifier, which is a dual-drain lateral spin-valve. The polarizer and analyzer are magnetized in opposite directions.

A schematic of the typical dual-drain lateral spin-valve is shown in Fig. 3.2. The ferromagnetic source contact (S) injects a spin-polarized current into the non-magnetic channel through a Schottky tunnel barrier [17, 18], which is collected at one of two ferromagnetic drain contacts (D1 and D2). The contact D2 is, however,

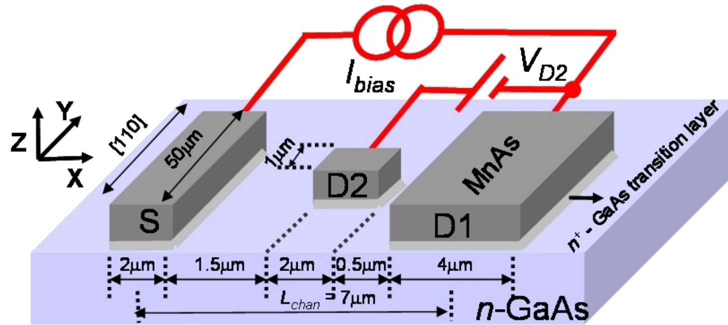

Figure 3.2: Schematic diagram of a spin polarization amplifier (not to scale). All three contacts S, D1 and D2 have magnetic easy axes along the $\hat{y}$ direction (GaAs [011] direction). The center of contact pad D2 is also the center of the effective channel L_{chan}. A fixed current bias I_{bias} establishes the spin-up and spin-down electrochemical potentials in the channel. The drain2 voltage V_{D2} controls the spin-current in contact pad D2.

distributive in nature (compared to the ideal point contact) and exactly centered within the effective channel between S and D1. The D2 terminal is operated near zero-bias with respect to the channel potential and the contact pad area is made much smaller than that of S and D1. Such operating conditions and pad dimensions ensure that the current collected at D2 is very small, compared to that collected at D1, and the potential in the channel is primarily determined by the current bias (I_{bias}) between S and D1. The geometric aspect ratios for S, D1 and D2 are chosen appropriately such that the coercivity is the largest for S and the smallest for D2. This particular choice allows various magnetization alignment conditions between S, D1 and D2 to be realized by sweeping the magnetic field B.

Figure 3.3 schematically shows the relative orientation of magnetization in S, D1 and D2 as B is swept from a large negative (positive) to a large positive (negative) value. The distinct states of magnetizations (M1-M4) and the corresponding D2 current (I_{D2}) are also shown for the $-B$ to $+B$ sweep. When the magnetic field is largely negative, S, D1 and D2 are all aligned in the same direction as B (state M1). The contacts D2 (state M2) , D1 (state M3) and S (state M4) then flip, in that sequence, as the magnetic field sweeps through zero in the positive direction because of the relative magnitude of the coercivities. If a bias current (I_{bias}) is applied between S and D1 having parallel magnetizations, it can be shown by solving the coupled spin drift-diffusion equations [55, 67] that the electrochemical potentials for spin-up ($\mu_{\uparrow}$) and spin-down ($\mu_{\downarrow}$) electrons in the channel are split. Higher doping in the channel [37] and low current bias [55] (hence, low electric field) operation in our devices ensure that drift is negligible. In absence of drift, it can be shown that the electrochemical potential splitting is antisymmetric with respect to the center, $x = L_{chan}/2$,which is also the center of contact pad D2. Hence, a bias voltage equal

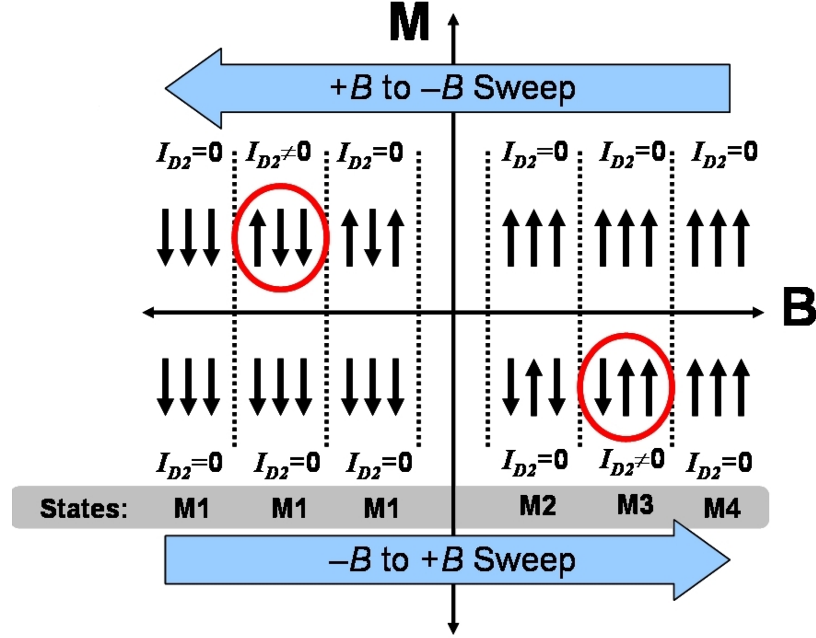

Figure 3.3: The magnetization directions of the three ferromagnetic contact pads S, D1 and D2 as the magnetic field B is swept in both directions. Each group of three arrows (left to right) represents the magnetization directions of S, D2 and D1 contact pads, respectively. The distinct states of magnetizations M1-M4 and the corresponding I_{D2} values for each state are shown for $-B$ to $+B$ sweep. A non-zero drain2 current I_{D2} flows in state M3.

to the cross-over potential for spin-up and spin-down electrons in the channel can be applied at D2 ($V_{D2} = V_{null}$) to make current $I_{D2} = 0$ for states M1, M2 and M4 in Fig. 3.3. Under this condition, spin up ($I_{D2\uparrow}$) and spin-down ($I_{D2\downarrow}$) currents are both equal to zero. However, I_{D2} will be non-zero under the same bias condition for state M3 where S and D1 are anti-parallel, for which the electrochemical potentials $\mu_\uparrow$ and $\mu_\downarrow$ are split at $x = 0$. The current spin polarization is conventionally defined as [17,18,55], $\alpha_{D2} = I_{D2,spin}/I_{D2,charge}$=($I_{D2\uparrow}$ - $I_{D2\downarrow}$)/($I_{D2\uparrow}$+$I_{D2\downarrow}$). Thus the current spin polarization at the D2 terminal can be much larger than that of the channel, resulting in a spin-current gain in the system. For a fixed I_{bias} in state M3, V_{D2} can be varied to control the spin polarization gain (amplification). The gain can also be controlled with $V_{D2} = V_{null}$ and variable I_{bias}. It may be noted that the design of the device facilitates lateral diffusion to compensate for any decrease in $\Delta\mu$ in the

channel due to carrier extraction at D2.

3.3 Device Growth and Fabrication

In our experiment, we fabricate dual-drain lateral spin-valves from a ferromagnetic manganese arsenide (MnAs) (90 nm thick), n^+ - doped ($\sim 10^{18}$-10^{19} cm^{-3}) gallium arsenide (GaAs) transition layer and n-doped GaAs ($N_D = 10^{17}$ cm^{-3}) heterostructure [19, 21], which is grown by MBE on a semi-insulating (SI) (001) GaAs substrate. The n-doping profile in the GaAs channel region and the GaAs/MnAs transition layer is shown in Fig. 3.4. The S, D1 and D2 contacts are made ferro-

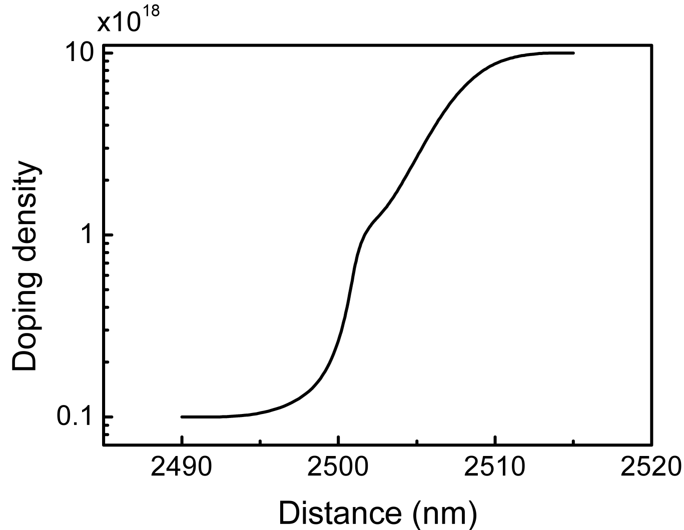

Figure 3.4: Doping profile in the GaAs channel and GaAs/MnAs transition layer. The zero of the x-axis is the top surface of the semi-insulating GaAs (001) substrate. This confirms the graded doping and the heavily doped GaAs region beneath MnAs, necessary for the Schottky tunnel contact.

magnetic by patterning them on MnAs. The source contact injects spin-polarized electrons through the heavily doped spin-selective Schottky tunnel barrier into the n - doped GaAs channel, which are subsequently collected at D1 or D2 through an identical tunnel barrier. The presence of a tunnel barrier is confirmed from temperature dependent conductivity measurement [19]. Eight devices with different channel

lengths (L_{chan}) and aspect ratios for the contacts pads were fabricated. The D2 pad is centered within the channel in all the devices. It is observed that the devices with smaller channel lengths give a larger spin-current amplification. Devices with aspect ratios different from those reported here exhibit exactly the same behavior, except the response is observed at a different magnetic field due to their different contact coercivities. The device shown in Fig. 3.2 is fabricated as follows. In the first step, the channel is defined on n - doped GaAs by etching away MnAs and n^+ - doped GaAs layers leaving only the S ($L \times W = 50\ \mu$m $\times$ 2 μm), D1 ($L \times W = 50\ \mu$m $\times$ 4 μm) and D2 pads ($L \times W = 1\ \mu$m $\times$ 2 μm). Next, silicon dioxide (SiO_2) is deposited as a passivation layer and via holes are created by dry etching. Finally, Ti/Au metal is evaporated by PVD and contacts are formed in a lift-off process. An SEM image of the device is shown in Fig. 3.5. The spin-selectivity of the

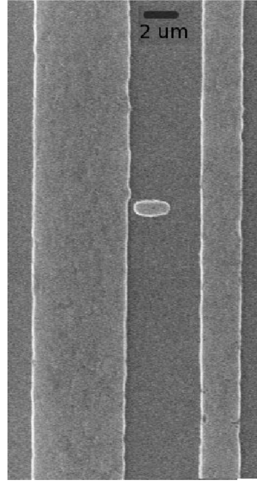

Figure 3.5: An SEM image of the spin-current amplifier after delineating source, drain1 and drain2 contacts by wet etching.

MnAs/GaAs tunnel barrier conductance, $\beta = G_\uparrow/G_\downarrow$ is determined to be 1.9 from channel length dependent magnetoresistance measurements on MnAs/GaAs/MnAs lateral spin-valves [19]. The conductivity of the n - doped GaAs channel (σ_n) is four orders of magnitude lower than that of MnAs (σ_f) in the temperature range of

operation of our devices. Identical control devices with non-magnetic D2 were also fabricated and characterized.

3.4 Spin-Valve Characteristics

The device operation is based on a spin-valve with source and drain1 magnetized in opposite directions. The magnetoresistance measurement is done to ensure basic spin-valve behavior in these devices. Figure 3.6 shows the measured magnetoresis-

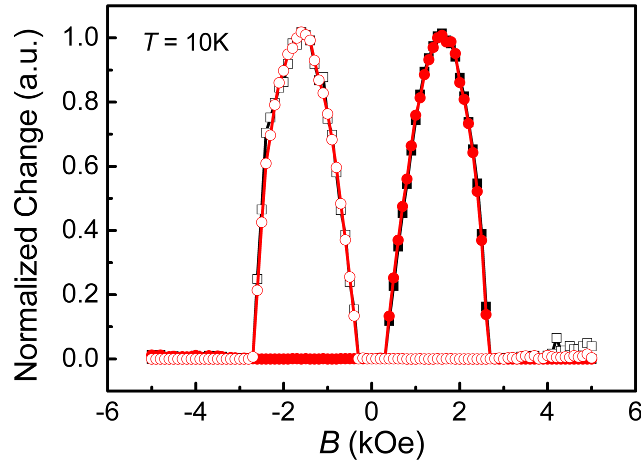

Figure 3.6: The magnetoresistance of a MnAs/GaAs lateral non-local spin-valve (circles) and drain2 current I_{D2} of a spin polarization amplifier (squares) as a function of applied magnetic field B at 10 K. The filled (open) symbols correspond to $-B$ to $+B$ ($+B$ to $-B$) sweep. The polarizer and analyzer dimensions of the MnAs/GaAs lateral spin-valve are same as that of S and D1 contact pads of the spin polarization amplifier, respectively. The peak values are normalized to unity. The overlap confirms that the peak I_{D2} coincides with the peak anti-parallel alignment between S and D1.

tance as a function of magnetic field at 10 K (circles). The drain2 current of a spin-current amplifier is also shown alongside (squares). The peak values are normalized to unity. The resistance is low when source and drain1 are magnetized in the same direction at high magnetic fields. The magnetoresistance is high when they are magnetized in opposite directions ($H = 1.5$kOe). This confirms the basic spin-valve characteristics in these devices. The anti-parallel configuration for spin-current amplifiers can therefore be achieved at $H = 1.5$ kOe. The complete overlap between

the magnetoresistance and the drain2 current confirms that the peak I_{D2} coincides with the peak anti-parallel alignment between S and D1. Control experiments were also done to ensure spin-dependency of the observed effects [19].

3.5 Spin-Current Amplifier Characteristics

The spin-current amplifier characteristics are measured by mounting the samples in a cryostat placed between the poles of an electromagnet. Figures 3.7(a) and (b) show current I_{D2} measured as a function of in-plane magnetic field B (directed along the y axis) for different temperatures T (I_{bias} = 100 μA) and I_{bias} (T = 10 K), respectively. The voltage V_{D2} is set to the corresponding null voltages (V_{null}, which depends on T and I_{bias}) in each case. A typical value for V_{null} at 10 K and I_{bias} = 100 μA is ~21 mV. The peak of I_{D2} coincides with the peak anti-parallel alignment between S and D1 at B = 1.5 kOe, which corresponds to state M3 in Fig. 3.3. The sign of current I_{D2} changes when the roles of S and D1 are reversed for the same value of B. This indicates that $\Delta\mu\,(= \mu_{\uparrow} - \mu_{\downarrow})$ and spin dependency of the effect change sign. The current decreases with increasing T and decreasing I_{bias}. Magnetoresistance measurements with conventional and non-local spin-valves show a peak at the same value of B, which also confirms that I_{D2} is sensitive to the spin-degree of freedom only. No response is observed for the control devices, with a non-magnetic D2 contact pad.

3.6 Modeling of Spin-Current Amplifiers

The experimental observations are explained by invoking the spin-diffusion model. The electrochemical potential in the channel region is described by the spin-diffusion

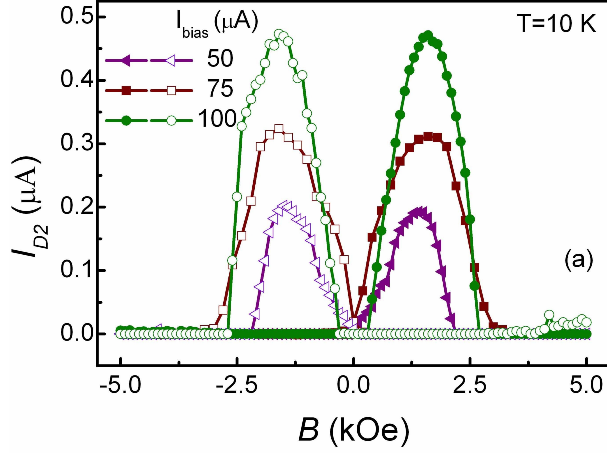

(a)

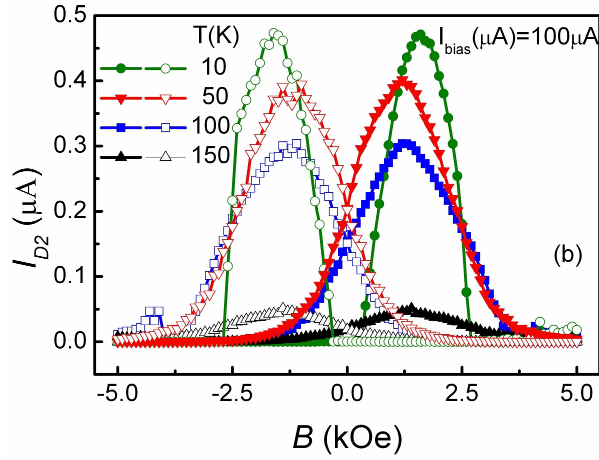

(b)

Figure 3.7: (a) Current I_{D2} as a function of magnetic field B for different I_{bias} with V_{D2} set to their corresponding null values (V_{null}) at 10 K; (b) current I_{D2} as a function of magnetic field B for different temperatures T with I_{bias} =100 μA and $V_{D2} = V_{null}$. The filled (open) symbols corresponds to $-B$ to $+B$ ($+B$ to $-B$) sweep.

equation as [67],

$$\frac{\partial^2(\mu_\uparrow - \mu_\downarrow)}{\partial x^2} = \frac{\mu_\uparrow - \mu_\downarrow}{\lambda_{sf}^2} \tag{3.1}$$

where λ_{sf} is the spin-diffusion length in the channel region. The small contribution from spin-drift is neglected because of the high doping in the channel region. The above equation is solved with the boundary conditions that the spin-currents are continuous at $x = 0$ and $x = L_{chan}$ (assuming there is no spin-flip scattering at the

interface) as given by,

$$j_\uparrow(0^-) = G_\uparrow \left[\mu_\uparrow(0^+) - \mu_\uparrow(0^-)\right] \tag{3.2}$$

$$j_\downarrow(0^-) = G_\downarrow \left[\mu_\downarrow(0^+) - \mu_\downarrow(0^-)\right] \tag{3.3}$$

$$j_\uparrow(0^-) - j_\downarrow(0^-) = j_\uparrow(0^+) - j_\downarrow(0^+) \tag{3.4}$$

where the current in each spin-channel is calculated as,

$$j_{\uparrow(\downarrow)} = \frac{\sigma_{\uparrow(\downarrow)}}{e}\frac{\partial \mu_{\uparrow(\downarrow)}}{\partial x} \tag{3.5}$$

The above equations are also written for $x = L_{chan}$. The solution of the spin-diffusion equation for the spin-up and spin-down electrons in S and D1 lateral MnAs/GaAs/MnAs spin-valves yields the electrochemical potentials in the channel as,

$$\mu_{\uparrow(\downarrow)} = \frac{jxe}{\sigma_n} + (-)\frac{2K}{\sigma_n}\left[\gamma \exp\left(-\frac{x}{\lambda_{sf}}\right) + \exp\left(\frac{x - L_{chan}}{\lambda_{sf}}\right)\right] \tag{3.6}$$

where j is the current density in the channel, e is the electron charge, and γ is +1 (-1) when magnetizations of S and D1 are anti-parallel (parallel). The constant K is determined from the boundary conditions as:

$$K = \frac{je\sigma_n}{8}\left[\frac{1+\alpha_f}{G_\uparrow} - \frac{1-\alpha_f}{G_\downarrow}\right] \Big/ \left[\gamma + \exp\left(-\frac{L_{chan}}{\lambda_{sf}}\right)\right] \tag{3.7}$$

where $\alpha_f(\sim 0.5)$ is the spin polarization of MnAs [50]. The current I_{D2} is then obtained as:

$$I_{D2} = \int_{L1}^{L2} \left[G_\uparrow\left(V_{D2} - \frac{\mu_\uparrow}{e}\right) + G_\downarrow\left(V_{D2} - \frac{\mu_\downarrow}{e}\right)\right] W_{D2} dx \tag{3.8}$$

where $L1$ are $L2$ are the bounding x coordinates of contact pad D2. The detailed derivation is described in Appendix B.

Figure 3.8(a) shows the measured peak I_{D2} as a function of I_{bias} in state M5 of the device. Theoretically calculated values of peak I_{D2}, using Eqn. 3.8 and a

value of $\lambda_{sf} = 7\ \mu$m, are also shown alongside the measured data. Figure 3.8(b) shows the estimated spin-diffusion length as a function of temperature. The good

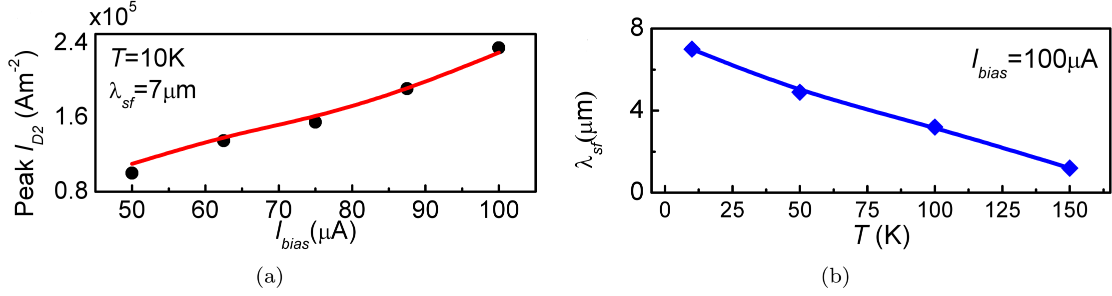

(a) (b)

Figure 3.8: (a) The peak drain2 current I_{D2} as a function of I_{bias} in state M3. The solid circles represent measured data at 10 K and the solid line represents the theoretically calculated values based on Eqn. 3.8. The spin diffusion length λ_{sf} is found to be 7 μm at 10 K. The spin-up and spin-down currents flow in opposite directions in contact pad D2, yielding spin polarization gain greater than unity; (b) estimated spin diffusion length as a function of temperature.

agreement provides further evidence for the spin-dependent effects in these devices. The electrochemical potential difference between spin-up and spin-down electrons is plotted as a function of position along the channel in Fig. 3.9. $\mu_\uparrow$ and $\mu_\downarrow$ remain anti-

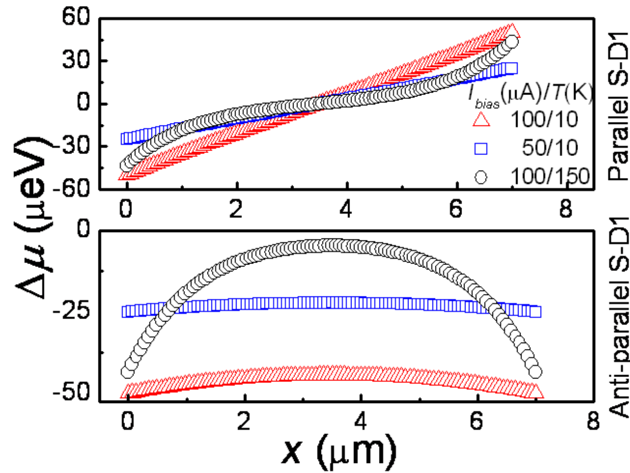

Figure 3.9: The anti-symmetric (symmetric) electrochemical potential difference ($\Delta\mu$) between spin-up and spin-down electrons in the channel when S and D1 contact magnetizations are parallel (anti-parallel) for two different temperatures T and I_{bias}. $\Delta\mu$ decreases in the channel at higher temperature due to enhanced spin relaxation. It increases at the source/channel interface ($x = 0$) for higher I_{bias} due to enhanced spin-splitting.

symmetric in the channel, making I_{D2} zero for all T and I_{bias} with $V_{D2} = V_{null}$, when

magnetizations of S and D1 are parallel. On the other hand, when the magnetizations of S and D1 are antiparallel, the difference $\Delta\mu$ decreases with decreasing I_{bias} and increasing T, which results in reduced I_{D2} in spite of increased tunnel conductance at higher T.

3.7 Amplifier Gain Characteristics

We calculate the current spin polarization α_{D2} as a function of I_{bias} and V_{D2} from measured values of I_{D2}. Figure 3.10(a) shows the current spin polarization gain (α_{D2}/α_f) as a function of V_{D2} for different I_{bias}. The voltage V_{D2} is varied in steps of 5 μV for the measurement of I_{D2} in this case. The gain curve shifts along the V_{D2} axis with increasing I_{bias} due to the increasing value of V_{null}. Figure 3.10(b) shows the gain curves as a function I_{bias} for different values of V_{D2}. The current

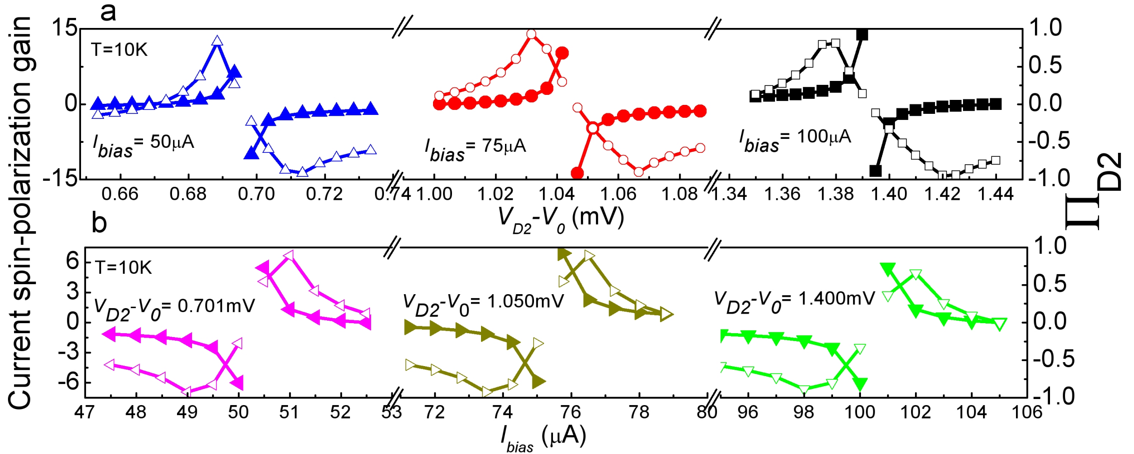

Figure 3.10: Dual control of the spin polarization gain. The open (closed) symbols represent negative (positive) gain. (a) Spin polarization gain as a function of V_{D2} for varying I_{bias} at 10 K. The gain increases with increasing I_{bias}; (b) spin polarization gain as a function of I_{bias} for varying V_{D2} at 10 K. A constant offset voltage, $V_0 = 19.565$ mV is subtracted from each of the V_{D2} values. The gain curves exhibit singularities along the V_{D2} and I_{bias} axes when a pure spin-current flows through contact pad D2 ($I_{D2} = 0$).

I_{bias} is varied in steps of 0.5 μA during this measurement. The plots show that the magnitude and sign of the polarization gain can be varied by changing the value

of I_{bias}. The gain curves exhibit several singularities along the V_{D2} and I_{bias} axes. These occur when the charge current at D2, $I_{D2} = 0$ ($I_{D2\uparrow}$ =- $I_{D2\downarrow}$) and a pure spin current, I_{spin} (= $I_{D2\uparrow}$ - $I_{D2\downarrow}$) flows through this contact [65, 68]. The peak gain that can be measured is limited by the smallest possible increment of V_{D2} and I_{bias} around these singularities. Hence, a combination of V_{D2} and I_{bias} can be used to electrically control the spin polarization gain. The gain can be made negative or positive by external bias, independent of the polarization of S and D1.

3.8 Conclusion

It is evident that the device just described provides current spin-polarization gain, which can be controlled from a very large negative value to a large positive value. It is possible to generate 100% spin-polarization for both majority and minority spins. Last, and not the least, the device generates pure spin current with zero charge current. These aspects might be useful for a new class of spintronic devices. Since a large spin polarization is not required at the input (source) terminal, the device may also facilitate the study of spin-based phenomena in materials wherein spin injection is difficult, such as silicon. It can further be used to make a novel memory device by placing several D2 contacts in the channel and tunning the geometric aspect ratios to maintain different states, which can be read electrically.

CHAPTER IV

Two Dimensional Spin Diffusion in Multi-Terminal Lateral Spin-Valves

4.1 Introduction

Spintronics has gained interest in recent years for the possibility of improved device performance and enhanced functionality of conventional devices [33]. Spintronic devices rely on efficient electrical spin injection and detection in semiconductors and metals [14, 19, 20, 25, 39, 43, 45]. Electrical spin injection and detection have recently been demonstrated in silicon [25, 39]. Most of the devices make use of the effects of one dimensional spin transport only. The effects of finite dimensions of magnetic contacts on spin-transport and the resulting spin-current distribution in lateral spin-valves have been explored theoretically [69, 70]. Spin extraction using a third terminal has recently been investigated for unique applications [71]. An additional contact terminal on the semiconductor channel of a conventional lateral spin-valve introduces another degree of freedom to the system, and its bias can be independently varied for controlled collection of spin and charge currents. We have investigated the advantages of two dimensional spin transport in spin extraction from semiconductors, using a third terminal, both experimentally and theoretically. We observe that transverse spin-diffusion *increases* the efficiency of spin extraction by a ferromagnetic contact, which can be very beneficial for three- or multi-terminal

spintronic devices. The observations are also useful for all-metal spintronic devices based on tunnel injection of spin polarized carriers.

4.2 Origin of Two Dimensional Spin Diffusion

When a current flows between polarizer and analyzer of a two terminal lateral spin-valve, the electrochemical potentials of spin-up ($\mu_\uparrow$) and spin-down ($\mu_\downarrow$) electrons split in the semiconductor channel. The splitting $\Delta\mu$ ($=\mu_\uparrow - \mu_\downarrow$) is large when the two contacts are magnetized in opposite directions. and small when the contacts are magnetized in the same direction. If a third contact is formed on the semiconductor channel of the spin-valve with anti-parallel magnetization of source and drain contacts, its potential can be varied enabling a controlled collection of spin-up and spin-down electrons [71]. Extracting carriers from the channel perturbs the equilibrium condition. The splitting decreases in the vicinity of the third contact and both the current- and spin-polarization decrease. However, if the size of this contact is significantly smaller than the other two contacts, the carriers can diffuse in the transverse direction. The diffusion occurs for both spin-up and spin-down electrons in such a manner it tends to increase the electrochemical potential levels to the unperturbed values. The amount of increase depends on the operating bias conditions and the geometric sizes of the contact pads.

4.3 Growth and Fabrication of Multi-Terminal Spin-Valves

A schematic of a typical device is shown in Fig. 4.1. The devices are fabricated from a ferromagnetic manganese arsenide (MnAs) (60 nm thick), n^+ - doped ($\sim 10^{19}$ cm^{-3}) GaAs transition region and n-doped GaAs ($n = 10^{17}$cm^{-3}) heterostructure grown by molecular beam epitaxy, using conventional photolithography, dry etch-

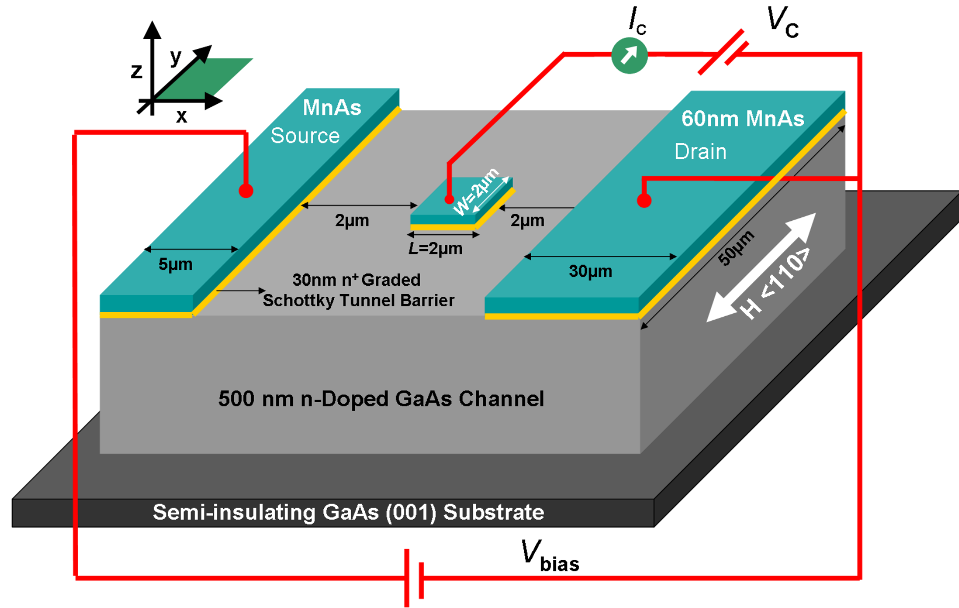

Figure 4.1: Schematic cross section of a typical three terminal device with $W = 2$ μm. The central terminal selectively collects electron with a particular spin through the voltage source V_c.

ing, metal deposition and lift-off techniques [19]. The dimensions of the source and drain are 5×50 μm^2 and 30×50 μm^2, respectively. The width of the *central* ferromagnetic contact (C) is varied as $W = 2, 4, 8, 16$ μm with the length fixed at $L = 2$ μm. Identical control devices with non-magnetic C terminal were also fabricated and characterized. The heavily doped region forms a Schottky tunnel contact for efficient spin injection into semiconductors [18]. The source (S) and drain (D) contacts form polarizer and analyzer of a conventional lateral spin-valve. The hysteresis characteristics of S and D contact pads, as determined from low temperature Magneto-Optic-Kerr-Effect (MOKE) measurements, are shown in Fig. 4.2.

4.4 Characterization of Multi-Terminal Spin-Valves

A voltage bias is applied between S and D terminals. Spin-polarized electrons are injected from S into the channel and the electrochemical potentials for spin-up ($\mu_\uparrow$)

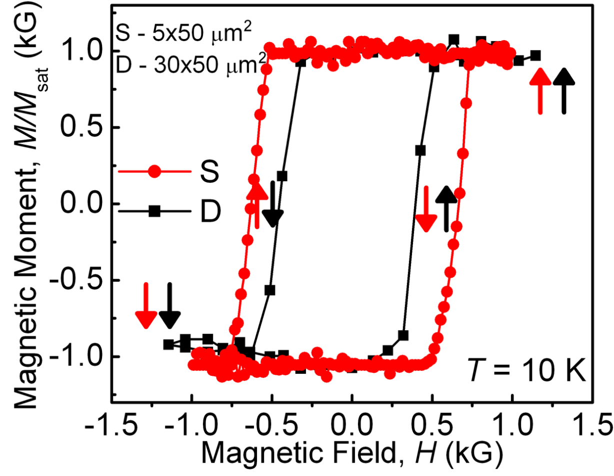

Figure 4.2: Hysteresis characteristics of source and drain contact pads as determined from low temperature MOKE measurements.

and spin-down ($\mu_{\downarrow}$) electrons split-up due to spin dependent reflections from D. The C contact extracts spin carriers from channel through voltage source V_c. Figure 4.3 shows the current extracted through terminal C, I_c as a function of applied magnetic field H for a $W = 2$ μm device. I_c is initially adjusted to zero by varying V_c $(= V_{null})$

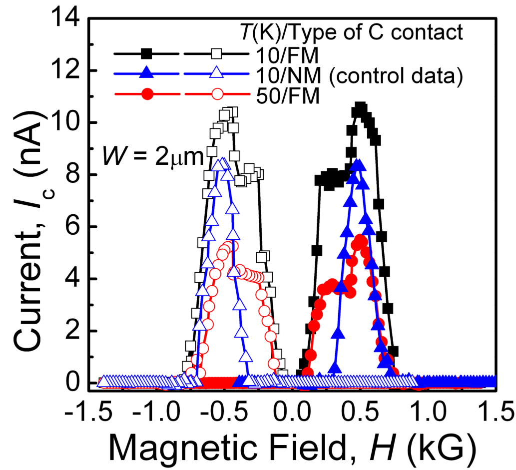

Figure 4.3: Measured collector terminal current I_C vs applied magnetic field H for a $W = 2$ μm device biased at $V_C = V_{null}$. Data are shown for both ferromagnetic and non-magnetic central contact C.

at large magnetic field ($|H| = 1.25$ kG), when all the three contacts are magnetized in the same direction. The current shows a plateau for 100 G $\lesssim |H| \lesssim$ 300 G, which

is followed by a peak at $|H| \sim 500$ G. The plateau occurs when magnetization for contact C changes direction earlier than S and D due to its smaller coercivity, and the peak occurs when S and D become anti-parallel at higher magnetic fields (300 G $\lesssim |H| \lesssim 750$ G, Fig. 4.2). The transitions in the current levels are gradual, which is due to the gradual reversal of the contact pad magnetizations as shown in Fig. 4.2. Devices with other values for W are identically characterized. They show similar responses except the plateau occurs at different H values due to different coercivities. This effect could be utilized to realize a multi-terminal spin-based memory device (shown in the inset to Fig. 4.4). The control devices with non-magnetic C contact

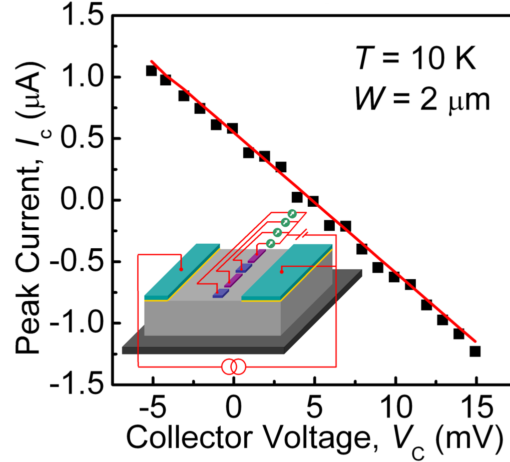

Figure 4.4: Measured I_C as a function of collector terminal voltage V_C at 10 K for the same device. The line shows the theoretically estimated values for I_C under the same experimental conditions. A schematic of a potential multi-terminal spin-based memory device is shown in the inset.

do not show the plateau in I_c, however they show a peak for 300 G $\lesssim |H| \lesssim 750$ G as before, the origin of which is due to magnetization switching of the ferromagnetic drain contact. Figure 4.4 depicts the measured current I_c (peak value) as a function of V_c for the $W = 2$ μm device at 10 K and $H \approx 500$ G (peak anti-parallel alignment between S and D). The almost linear behavior ensures that the device is operated in the linear response regime under the experimental conditions discussed here.

4.5 Modeling of Two Dimensional Spin Diffusion

We have used the coupled spin diffusion equation to determine the electrochemical potentials $\mu_\uparrow$ and $\mu_\downarrow$ and the spin-polarization in the channel [55]:

$$\nabla^2 \mu_{\uparrow(\downarrow)} = \frac{\mu_{\uparrow(\downarrow)} - \mu_{\downarrow(\uparrow)}}{\lambda^2_{\uparrow\downarrow(\downarrow\uparrow)}} \tag{4.1}$$

where ∇^2 is the Laplacian and $\lambda_{\uparrow\downarrow}(\lambda_{\uparrow\downarrow})$ is the average electron spin-flip length from spin-up (spin-down) to spin-down (spin-up) state. The small contribution from drift is neglected. The high doping in the channel, high tunnel contact resistance and low bias operation ensure that the peak electric field in the channel $E_{peak} < E_c$ $[= (1/e\lambda)(\mu/eD)^{-1} = 1.4$ kV/m], where e is the electronic charge, λ is the average spin-diffusion length, μ is the effective electron mobility and D is the effective electron diffusion constant [55]. The depth of the channel in our devices is very small ($h = 0.5$ μm) compared to the other dimensions. The variation along the z-direction (see Fig. 4.1) is negligible, and the electrochemical potentials are assumed to be invariant along this direction and are approximated with an average constant value [69]. Equation 4.1 is solved for our devices with the boundary conditions that (1) the spin-up and spin-down current-flow normal to the hard boundaries (edges of the GaAs channel in x- and y- directions) are individually zero, and (2) spin-up and spin-down currents are continuous at the ferromagnetic contacts. The effects of spin-dependent Fermi wave vectors, transmission coefficients and density of states are taken into account by considering spin-dependent resistance for electrons ($G_\uparrow$,$G_\downarrow$) at the ferromagnet/semiconductor contact region at low temperatures [69, 72]. The effect of a heavily doped region on spin extraction is discussed in Ref. [73]. The MnAs/GaAs tunnel conductance and spin-selectivity of the tunnel barrier are experimentally determined to be $G_\uparrow + G_\downarrow \approx 2.9 \times 10^7$ Ω^{-1}m^{-2} and $\beta = G_\uparrow/G_\downarrow \approx 1.9$ at

10 K, respectively. The electron mobility is determined from Hall measurements as $\mu \approx 3000$ cm^2/V.s at 10 K.

Theoretically estimated values for I_c under the experimental bias conditions at 10 K are shown alongside the experimental data (squares) in Fig. 4.4. The spin diffusion length, $\lambda = \lambda_{\uparrow\downarrow}/\sqrt{2} = \lambda_{\downarrow\uparrow}/\sqrt{2}$ is found to be equal to 7 μm at 10 K, which is close to the value reported earlier [71]. The small deviation between experiment and theory at higher current values is due to higher tunnel conductance at higher bias and asymmetric MnAs/GaAs tunnel barrier characteristics. Good agreement between experiment and theory supports the assumption that the device operates in a linear response regime under the stated experimental conditions. The predicted values for I_c for all our devices match well with the experiments within the limits of experimental error. We define an *enhancement factor*, ξ, as the ratio of the integrated divergence of spin-current in the y direction to the integrated divergence of the total spin-current under the contact C, to determine the contribution of transverse (along y direction) diffusion to current spin-polarization. Thus

$$\xi = \oint_{\mathcal{C}} \left[\widehat{\mathbf{y}} \frac{\partial \left(\Delta\mu\right)}{\partial y} \right] .d\mathbf{r} \Bigg/ \oint_{\mathcal{C}} \left[\left(\widehat{\mathbf{x}} \frac{\partial}{\partial x} + \widehat{\mathbf{y}} \frac{\partial}{\partial y} \right) \left(\Delta\mu\right) \right] .d\mathbf{r} \tag{4.2}$$

where the contour $\mathcal{C}$ consists of the closed boundary of contact C. ξ is determined under the operating conditions by using Eqn. 4.2 and experimentally determined device and bias parameters.

4.6 Enhancement of Spin Polarization

Figure 4.5 shows the current spin-polarization and ξ as a function of I_c. The current spin-polarization decreases for large values of I_c (hence for large value of V_c) as $(\mu_\uparrow/e - V_c)$ and $(\mu_\downarrow/e - V_c)$ become comparable and the polarization is primarily determined from the spin selectivity of the tunnel barrier. However, the magnitude

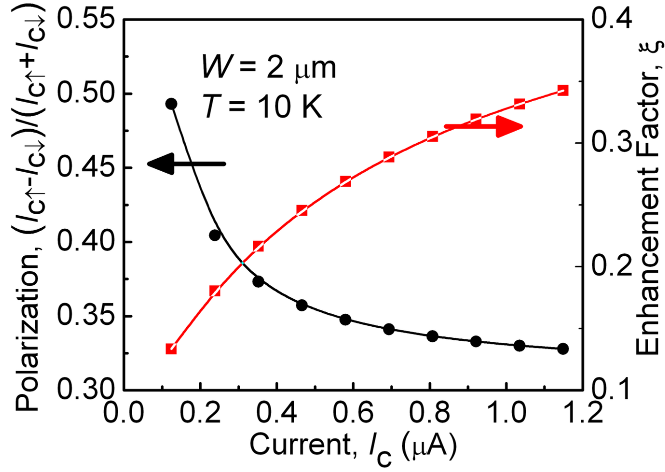

Figure 4.5: Estimated current spin polarization (left y axis) and enhancement factor (right y axis) vs measured I_C at 10 K.

of ξ increases, which indicates an increase in transverse spin-diffusion to compensate for the perturbation in the channel potential. The rate of increase in ξ decreases with increasing bias due to finite spin-polarization beyond the contact pad C. An exponential characteristics indicates a very strong dependence of ξ on spin extraction. It should be noted that ξ increases in a direction to compensate for the reduction in spin-polarization.

Figure 4.6(a) shows ξ versus normalized carrier extraction (I_c/W) for different contact widths. ξ increases with increasing carrier extraction. However, it saturates earlier and to a lower value for larger width devices, which indicates that the current spin-polarization is smaller for larger width devices. Hence, spin polarized carrier extraction is more efficient in the presence of transverse diffusion. Figure 4.6(b) shows ξ decreases exponentially with increasing W for fixed values of I_c/W. The transverse diffusion is, therefore, more efficient for contact pads having smaller aspect ratio W/L because of geometric size effect. The exponential dependence of ξ on W emphasizes the importance of transverse diffusion in these cases.

To determine the extent of perturbation in the electrochemical potentials from

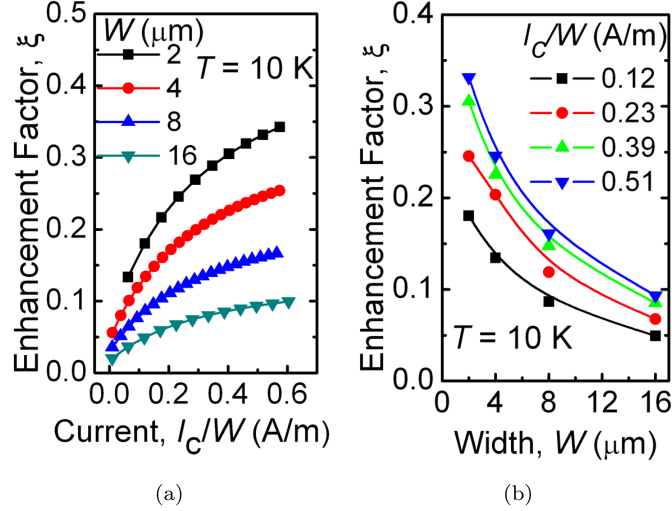

Figure 4.6: (a) Enhancement factor ξ vs normalized collector current I_C/W for various width devices at 10 K; (b) ξ vs device widths W for various levels of normalized carrier extraction I_C/W at 10 K.

equilibrium condition due to spin extraction, the electrochemical potential difference $(\Delta\mu - \Delta\mu_0)$ is plotted for $W = 2$ μm (Fig. 4.7(a)) and $W = 16$ μm (Fig. 4.7(b)) devices biased at $V_c - V_{null} = 1$ mV. It can be seen that the perturbation is very small and localized beneath the contact for $W = 2$ μm device. The maximum decrease is $\sim$5 μV compared to the $\sim$23 μV determined for $W = 16$ μm device. Also, the reduction extends over a larger area below the drain contact for $W = 16$ μm device. This confirms our earlier observation that transverse spin diffusion is more efficient for smaller width devices. It is also observed that the spin-current absorption due to an intervening magnetic contact is negligible for both the devices with $I_c = 0$. Such behavior is reported earlier in all-metal spin-valves [74].

4.7 Conclusion

The effects of two dimensional spin diffusion on spin extraction in lateral semiconductor spin-valves have been investigated experimentally and theoretically. A ferromagnetic collector terminal of variable size is placed between the ferromagnetic

electron spin injector and detector of a conventional lateral spin valve for spin extraction. It is observed that transverse spin diffusion beneath the collector terminal

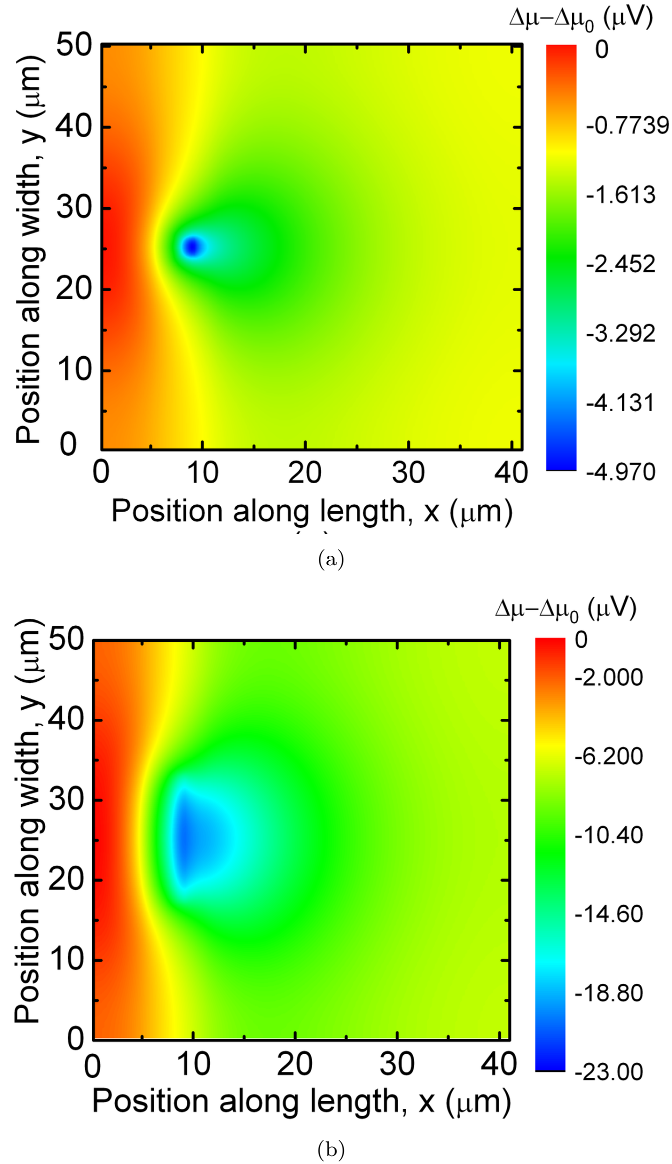

Figure 4.7: Deviation from equilibrium electrochemical potential difference between spin-up and spin-down electrons are plotted for (a) $W = 2$ μm and (b) $W = 16$ μm devices at 10 K.

plays an important role along with the conventional longitudinal spin diffusion in describing the overall transport of spin carriers. Two dimensional spin diffusion reduces the perturbation of the channel electrochemical potentials and improves spin extraction. The small size of the contact pad facilitates transverse spin-diffusion leading

to increased spin polarization and reduced perturbation from the equilibrium conditions. This study suggests that the width is also an important design parameter for spintronic devices.

CHAPTER V

Electrically Driven Spin-Dynamics of Paramagnetic Impurities: A Spin Capacitor

5.1 Introduction

Electrical spin injection, manipulation and detection in non-magnetic materials have gained interest in recent years for the possibility of realizing spintronic devices [33, 75]. The successful operation of spin-valve and spin-torque devices [11, 14, 20, 57, 71, 76] is dependent on minimizing spin-scattering during transport through non-magnetic metals, semiconductors and hetero-interfaces [59]. In contrast, in this paper we report experiments on a lateral MnAs/GaAs/MnAs spin-valve structure (Fig. 5.1) [19,77] with paramagnetic Mn impurities that are *deliberately introduced* into the channel region. These Mn impurities cause spin-flip scattering and, since they do not have any significant alternative means of relaxation [78], get polarized in the process resulting in a decrease in the spin-flip current and hence the terminal current. This transient response in the terminal current due to an electrically driven impurity polarization is the subject of the present study. The study demonstrates electrical detection and manipulation of the spin-magnetic moment of bound magnetic impurities in semiconductors, which may be useful in envisioning new devices [79]. The observed phenomenon should be scalable to very few magnetic impurities, which will be useful for the realization of quantum information processing

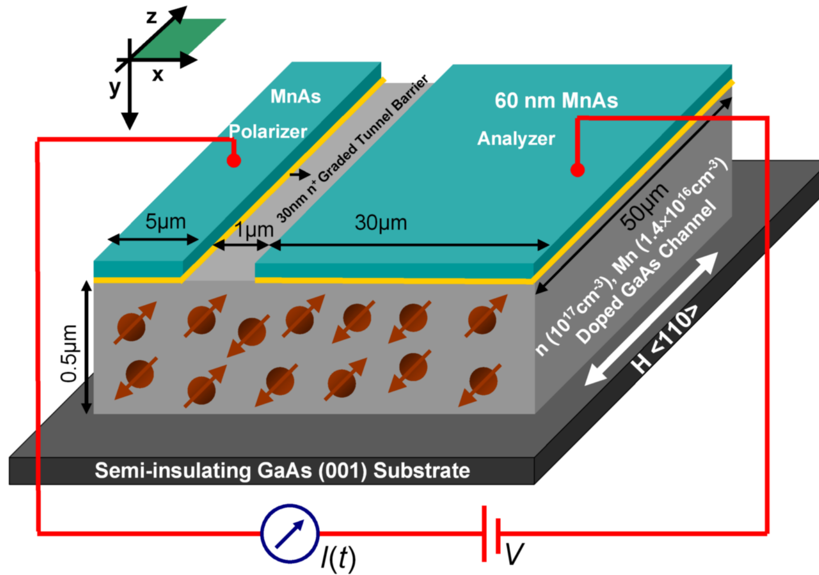

Figure 5.1: Schematic cross-section (not to scale) of a typical Mn-doped spin-valve. The channel region is n-type and it is lightly co-doped with Mn impurities. The arrows indicate the initial unpolarized Mn impurities.

devices [80]. The study also provides an easy method to determine the spin-spin scattering time constant between various magnetic impurities and delocalized conduction electrons.

We demonstrate experimentally, for the first time to our knowledge, that (1) the impurities can be polarized when the spin-valve is operated in the anti-parallel configuration but not in the parallel configuration, and, (2) this polarization leads to a transient response in the terminal current. Both these features appear to be in good agreement with the model proposed in refs. [81] and [79] where it is shown that the spin-polarization of the channel electrons is negligible in the parallel configuration but is much larger in the anti-parallel configuration and the resulting spin-flip current polarizes the Mn impurities. This is similar in principle to the well-known Overhauser effect (or dynamic nuclear polarization (DNP)) [82] but it is driven by the exchange interaction between the conduction band electrons in GaAs and localized Mn impurity spins rather than the hyperfine nuclear interaction. To our knowledge, neither

(1) the dynamic impurity polarization nor (2) the use of anti-parallel spin-valves to drive it electrically (with no external magnetic field) have been demonstrated before.

5.2 Growth and Fabrication

The heterostructure samples in the experiments are grown by molecular beam epitaxy on semi-insulating GaAs (001) substrate and consist of a ferromagnetic type-A manganese arsenide (MnAs) (60 nm) layer, n^+-doped ($\approx 10^{19}$ cm^{-3}) GaAs transition region (30 nm), and n-doped ($N_D \approx 10^{17}$ cm^{-3}) GaAs channel region ($h = 500$ nm), which is lightly co-doped with Mn impurities ($N_{\rm Mn} \approx 1.4 \times 10^{16}$cm^{-3}). The growth procedure is as follows. A 500 nm GaAs:(Si,Mn) channel layer is grown at 580 °C on a (2×4)-reconstructed surface using a growth rate and V/III beam equivalent pressure ratio of 0.72 μm/hr and 25, respectively. A 30 nm graded-doping n^+-GaAs contact layer is then grown with the Mn flux shuttered to form a triangular tunnel barrier. The substrate temperature is ramped down to 400 °C under an As_4 overpressure, and the surface reconstruction transitions to a c(4×4) pattern as indicated by reflection high-energy electron diffraction (RHEED). The As_4 flux is shuttered, and the substrate temperature is ramped down to 200 °C. Once the temperature has stabilized, the surface is soaked with an As_4 flux of 5×10^{-6} Torr for 90 s to form a template suitable for growth of type-A MnAs [83]. A 60 nm MnAs film is grown using a low growth rate (10 nm/hr) and substrate temperature (200 °C) during deposition of the first few monolayers of MnAs. After the nucleation phase completes, the growth rate and substrate temperature are both increased to 40 nm/hr and 250 °C, respectively. Analysis of the RHEED pattern indicates growth of a type-A MnAs film with the following epitaxial relationship: [$\bar{1}\bar{1}$20]MnAs//[110]GaAs.

The devices are fabricated by using conventional photolithography, dry etching,

metal deposition and lift-off techniques [19]. The Mn concentration in the channel is sufficiently low such that significant donor compensation or formation of MnAs precipitates can not occur [84]. The effective donor density in the channel region is, $n_0 = N_D - N_{Mn} = 8.6 \times 10^{16}$ cm^{-3}. The Mn doping density is verified by secondary ion mass spectroscopy (SIMS), shown in Fig. 5.2. SQUID measurements on the (Si,Mn)-doped channel region does not show any hysteresis (shown in the inset to Fig. 5.2). This confirms the absence of ferromagnetism in the Mn-doped

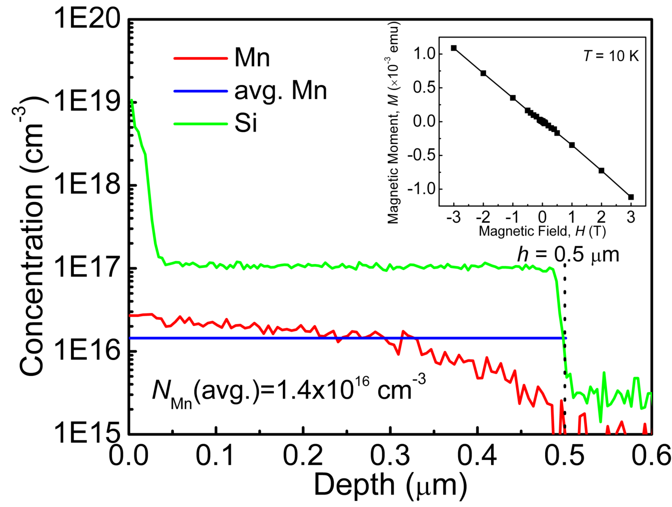

Figure 5.2: The doping densities of silicon (n-doping) and Mn versus channel depth are shown. Mn atoms behave as acceptors and partially compensate the n-doping. Inset shows the SQUID measurement on (Si,Mn) doped channel region grown on semi-insulating GaAs(001) substrate. The absence of remanent magnetization indicates lack of ferromagnetism in the channel region.

channel region. The lightly doped Mn atoms in GaAs behave as paramagnetic impurities [78, 85]. Identical control devices without Mn impurities in the channel region were also fabricated and characterized. The heavily Si- doped (n^+) region beneath the MnAs contact pads forms a Schottky tunnel contact for efficient spin injection into semiconductors [18]. The basic MnAs/GaAs/MnAs spin-valve behavior of both Mn-doped spin-valves and control devices is confirmed through conventional and control measurements using a four probe ac lock-in technique [19]. Figure 5.3

shows the measured magnetoresistance as a function of applied magnetic field H for a Mn-doped spin-valve. The two peaks correspond to the anti-parallel alignment of analyzer (A) and polarizer (P) at $H = 500$ G, which is confirmed by low temperature MOKE measurements, also shown in Fig. 5.3. A peak magnetoresistance of $\sim$1.3%

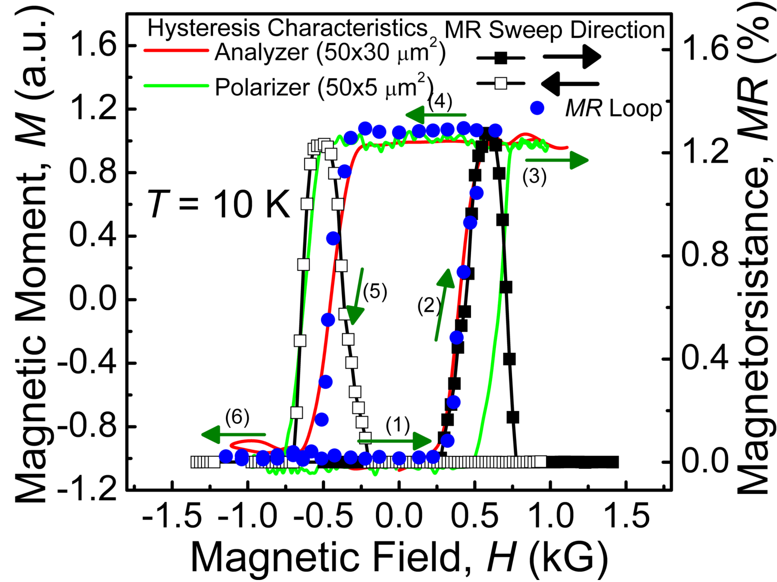

Figure 5.3: MOKE measurements (left y axis) on analyzer and polarizer contact pads, and magnetoresistance measurements on the Mn-doped spin-valves (right y axis) versus applied magnetic field at 10 K. The magnetoresistance data show two peaks which correspond to the antiparallel magnetization alignment of analyzer and polarizer contact pads. The MR loop closely follows the hysteresis of the analyzer contact pad. The arrows indicate the magnetic field sweep directions for the hysteresis plots. Contact pad magnetization data are shown for sweep (1)-(6). The MR loop is shown for sweep (1),(2),(4)-(6).

is measured at 10 K, which is close to the value reported earlier [19].

5.3 Transient Characterization of Devices

Transient current measurements are performed by mounting the samples in a cryostat, placed between the poles of an electromagnet. An in-plane variable magnetic field (along the magnetic easy axis of MnAs, GaAs [110] direction) is swept quasi-statically from -5 kG to 500 G, which sets the polarizer and analyzer magnetization in opposite directions (Fig. 5.3). The magnetic field is then swept back to

zero. The polarizer and analyzer retain the anti-parallel magnetization configuration due to the remanence of ferromagnetic MnAs contact pads. A voltage bias is applied and the current through the device is measured as a function of time. Figure 5.4(a) shows the measured data for $T = 10$, 15 and 20 K. The current is initially large at 99.94 μA, before it saturates to a lower value of 98.86 μA at $T = 10$ K. The measurements are repeated for $T = 15$ and 20 K. It is observed that the relative change $[\Delta I = I(t = 0) - I(t = \infty)]$ decreases from 1.08 μA to 0.55 μA as the temperature increases from 10 K to 15 K. The effect disappears for T $\geq$ 20 K. No transient change in current was observed for control devices at all temperatures. The external magnetic field is zero during the transient measurements, which prevents spurious polarization of Mn impurities from external magnetic fields.

Similar measurements were carried out with polarizer and analyzer magnetized in the same direction. In this case, an in-plane -5 kG (larger than the coercivity of both the contact pads) magnetic field is applied to magnetize both contacts in the same direction. The magnetic field is then quasi-statically made zero. A pulse bias is applied as before and the transient current through the device is measured. Figure 5.4(b) shows the measured current as a function of time at $T = 10$, 15 and 20 K. No noticeable change in the current level is observed under these conditions. Figure 5.4(c) shows the magnetoresistance, $MR = (I_P - I_{AP})/I_{AP}$ as determined from Figs. 5.4(a) and (b).

5.4 Origin of Transient Current

Almost all the experimental features can be explained in terms of the circuit diagrams in Fig. 5.5 (adapted from Figs. 3(a) and (b) of ref. [81]), where the elements in the "shunt arm" g_{so}, g_γ and I_γ represent spin-flip processes that try to

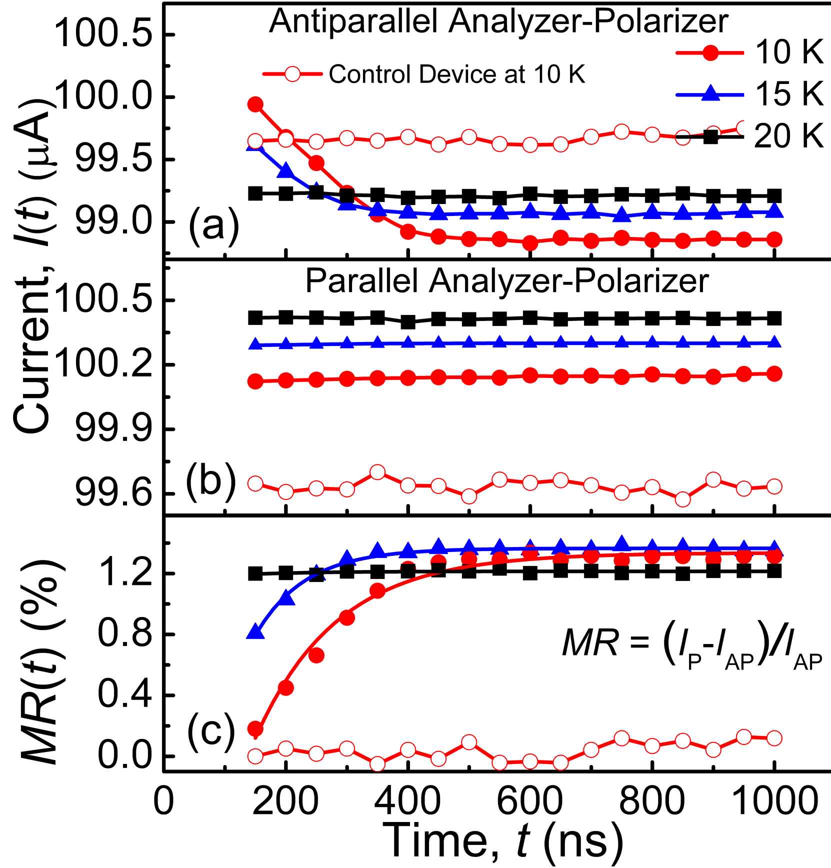

Figure 5.4: The measured transient current through the device as a function of time with (a) anti-parallel and (b) parallel magnetization of analyzer and polarizer contacts. The current is initially large before it saturates to a lower value for the anti-parallel configuration. No significant change is observed for the parallel configuration; (c) magnetoresistance, $MR = (I_P\text{-}I_{AP})/I_{AP}$ as a function of time. The solid-lines show $MR(t)$ as determined from the model using appropriate model parameters. An external trigger is generated at $t = 0$. There is a delay of $\sim$150 ns for the voltage source and the electrometer to respond to this trigger, which leads to the the shift in the origin for the time axis by the same amount.

restore the imbalance in the electrochemical potentials $\mu_\uparrow$ and $\mu_\downarrow$ in the spin-up and spin-down channels. *First, the transient terminal current is observed only for the anti-parallel configuration and not for the parallel configuration* (Fig. 5.4). This can be understood by noting that the contact conductances, in the parallel configuration, form a balanced "Wheatstone Bridge" (Fig. 5.5(a)), which results in negligible potential difference $\mu_\uparrow - \mu_\downarrow$ between spin-up and spin-down channel electrons. By contrast, the anti-parallel configuration results in a significant imbalance potential

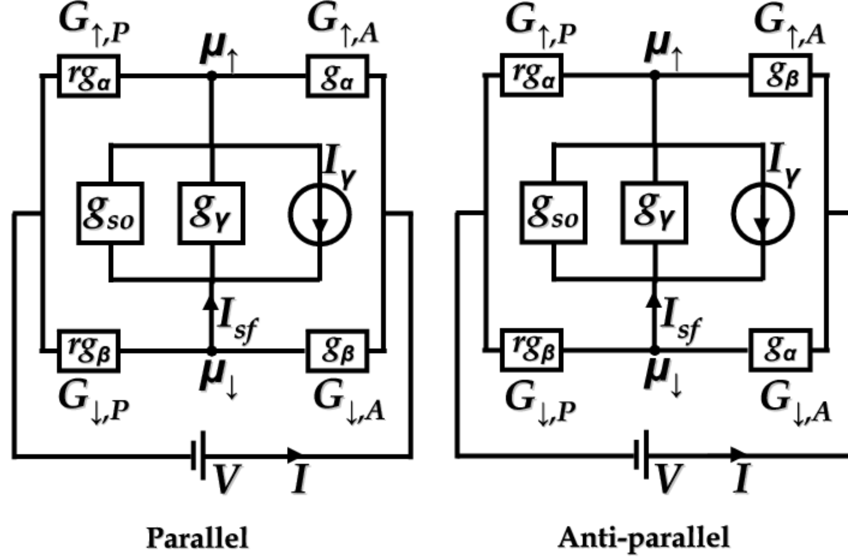

Figure 5.5: Equivalent circuit diagram of the SCT structure: g_γ, g_{so}, $G_{\uparrow(\downarrow),P}$, $G_{\uparrow(\downarrow),A}$, g_α, g_β, r,$\mu_{\uparrow(\downarrow)}$, and, I_{sf} are spin-flip conductance due to Mn impurity, spin-flip conductance independent of Mn impurity, polarizer conductance for up(down)-spin, analyzer conductance for spin-up(down) electrons, majority-spin tunnel conductance, minority-spin tunnel conductance, polarizer to analyzer area ratio, average chemical potential for spin-up(down) channel electrons, and, total spin-flip current respectively. The current source $I_\gamma \propto \int dE\{f_\uparrow(1-f_\downarrow)+f_\downarrow(1-f_\uparrow)\}(F_\uparrow - F_\downarrow)$, where, $f_{\uparrow(\downarrow)}$ and $F_{\uparrow(\downarrow)}$ are the average energy (E) distribution of spin-up(down) electrons having chemical potential $\mu_{\uparrow(\downarrow)}$ and fraction of impurities having up(down)-spin respectively.

$\mu_\uparrow - \mu_\downarrow$, which gives rise to spin-flip processes that polarize the impurities leading to transient behavior in the terminal current. *Second, the terminal current in the anti-parallel configuration decays with time with a time-constant* $\sim(k_BT)^{-1}$: This is understood by noting that as the Mn impurities get polarized ($F_\uparrow - F_\downarrow$ increases) the spin-flip current (through g_γ and I_γ) and hence the terminal current decreases. So the transient behavior in the terminal current is, in essence, the signature of the dynamics of polarization ($F_\uparrow - F_\downarrow$) of the Mn impurity spins. Assuming that the Mn impurities have negligible spin-lattice-relaxation [78] the time constant (τ) for impurity polarization through exchange interaction with conduction band electrons has been shown, according to NEGF treatment, to be inversely proportional to $\int dE\{f_\uparrow(1-f_\downarrow)+f_\downarrow(1-f_\uparrow)\} \approx k_BT$ for $\mu_\uparrow - \mu_\downarrow < k_BT$ (Eqn. 5.6 and the associated

discussion in [81]). Our model thus suggests that $\tau \sim (k_B T)^{-1}$ is in agreement with experiment (120 ns at 10 K, 80 ns at 15 K). As the temperature increases we expect the effect to get smaller because g_{so} increases (increased spin-orbit relaxation) while g_γ decreases (fewer Mn impurities are present within a spin-diffusion length which gets shorter with temperature). While this is in qualitative agreement with experimental observations we do not have a full quantitative explanation for the disappearance of the effect at 20 K. One of the possible reasons may be that the phonon assisted spin-lattice relaxation of Mn impurities in GaAs becomes dominant at the higher temperatures. Interestingly our model predicts that as $t \to \infty$ the Mn impurities get polarized and do not contribute to spin-flip scattering any more, suggesting that a spin-valve with and without Mn impurities should show approximately the same temperature dependent magnetoresistance determined by the spin-orbit term (g_{so}). This seems to be in agreement with experimental observations [19].

5.5 Modeling of Spin Dynamics

For a quantitative model, we have adopted two approaches: one based on the Non-equilibrium Green's Function (NEGF) method [81] and one based on the drift-diffusion method [55,69]. Both can be approximately mapped onto the circuit model of Fig. 5.5 and lead to similar quantitative results. Here we present results from the second model, which is based on the spin-diffusion equation,

$$D\frac{\partial^2 n_{\uparrow(\downarrow)}}{\partial x^2} = \frac{\partial n_{\uparrow(\downarrow)}}{\partial t} + \frac{n_{\uparrow(\downarrow)} - n_{\downarrow(\uparrow)}}{\tau_{\uparrow\downarrow(\downarrow\uparrow)}} + \frac{1}{e^2 h} G_{\uparrow(\downarrow)} \left[\mu_{\uparrow(\downarrow)} - eV\right] \tag{5.1}$$

where D is the effective diffusion coefficient, $n_{\uparrow(\downarrow)}(x,t)$ is the spin-up (spin-down) electron density, $G_{\uparrow(\downarrow)}(x)$ is the spin-up (spin-down) tunnel conductance, $V(x)$ is the applied voltage, and $\mu_{\uparrow(\downarrow)}(x,t)$ is the electrochemical potential for spin-up (spin-down) electrons. Also, the relation, $n_\uparrow(x,t) + n_\downarrow(x,t) = n_0$ holds. The time depen-

dence of the spin-flip current, $I_{sf} = I_{\uparrow,A}$ - $I_{\uparrow,P}$ with spin-dynamics is determined by integrating Eqn. 5.1 as:

$$\frac{1}{e}[I_{\uparrow,\mathrm{A}}(t) - I_{\uparrow,\mathrm{P}}(t)] \quad = \quad \frac{\partial N_{\uparrow}}{\partial t} + \frac{N_{\uparrow} - N_{\downarrow}}{\tau_{\uparrow\downarrow}} \tag{5.2}$$

where $N_{\uparrow(\downarrow)}$ are the total number of spin-up (spin-down) electrons in the channel. Equation 5.2 helps to decouple the spin-scattering due to Mn impurities and the scattering due to Mn-independent processes. We define a parameter β which correlates $n_{\uparrow(\downarrow)}$ with $\mu_{\uparrow(\downarrow)}$ through Fermi-Dirac distribution and density-of-states functions, and which is approximated by a linear function obtained from Taylor series expansion as,

$$\beta = \frac{n_{\uparrow(\downarrow)} - n_0/2}{\mu_{\uparrow(\downarrow)} - \mu_0} = \left[\frac{\partial n_{\uparrow(\downarrow)}}{\partial \mu_{\uparrow(\downarrow)}}\right]_{\mu_{\uparrow(\downarrow)}=\mu_0} \tag{5.3}$$

where μ_0 is the electrochemical potential for the unpolarized electrons, $n_{\uparrow} = n_{\downarrow} = n_0/2$. The detail model is described in Appendix C. The high doping in the channel, large contact resistance and low bias operation lead to negligible drift in these devices [55]. The model parameters, determined at 10 K, are as follows: (1) from Hall measurements, $\mu = 3000$ cm^2/V.s; (2) from the Fermi integral, $De/\mu k_B T = 8.3$ [55]; (3) tunnel conductance and spin-selectivity of the tunnel barrier are determined by analyzing the experimentally measured magnetoresistance data (assuming $\tau_{\uparrow\downarrow} = \tau_{\downarrow\uparrow} = 13$ ns [37]) with the spin-diffusion model. Thus $G_{\uparrow} + G_{\downarrow} = 2.5 \times 10^7$ Ω^{-1} m^{-2} [19]; (4) from Fermi-Dirac distribution and density-of-states functions, $\beta = 0.2{\cdot}(n_0/2k_BT)$.

5.6 Determination of Spin Relaxation Time Constant

Figure 5.6(a) shows the estimated time dependence of the spin-flip current in the antiparallel configuration as determined by using Eqns. 5.1 and 5.2 on the experimental data shown in Fig. 5.4. Note that the change in spin-flip current ΔI_{sf} at

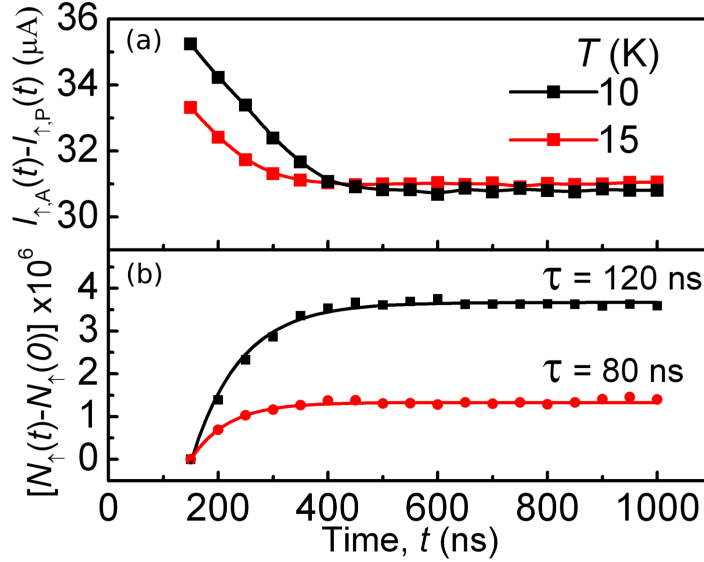

Figure 5.6: (a) Estimated spin-flip current as a function of time, for $T = 10$ and 15 K. The spin-capacitive effect is reduced at higher temperatures due to enhanced spin-relaxation from native GaAs lattice atoms; (b) *charging* of Mn paramagnetic spin as a function of time.

different temperatures is larger than the change in the terminal current ΔI, as we would expect from the circuit diagram of Fig. 5.5 which gives $\Delta I_{sf}/\Delta I = (1/P_c)\{1 + (r-1)^2(1-P_c^2)/(4r)\}$, where, $P_c = (g_\alpha - g_\beta)/(g_\alpha + g_\beta) = (G_\uparrow - G_\downarrow)/(G_\uparrow + G_\downarrow)$. Using experimental values ($P_c = 0.39$ and $r = 1/6$) we find $\Delta I_{sf}/\Delta I$ to be 4.8, which is reasonably close to the value of 3.6 obtained from the detailed numerical calculation (see Figs. 5.4 and 5.6). Time constants (τ) associated with the charging of the *spin-capacitor* (Fig. 5.6(b)) as determined by using Fig. 5.6(a) and Eqn. 5.2 are found to be 120 ns and 80 ns at 10 K and 15 K, respectively. The estimated value for τ (120 ns) is close to the value of the spin-spin relaxation time-constant (100 ns) reported earlier for an interaction between conduction electron spin and a paramagnetic defect in a silicon field-effect-transistor [86].

5.7 Conclusion

In summary, the spin-dynamics of dilute paramagnetic impurities embedded in a semiconductor GaAs channel of a conventional lateral spin-valve has been investigated. It is observed that the electron spin of paramagnetic Mn atoms can be polarized electrically when driven by a spin-valve in the anti-parallel configuration. The spin-polarization of the paramagnetic impurities retain their state as long as the applied bias is present. The transient current through the MnAs/GaAs/MnAs spin-valve bears the signature of the underlying spin-dynamics driven by the exchange interaction between the conduction band electrons in GaAs and the localized Mn electron spins. The time constant for this interaction is observed to be dependent on temperature and is estimated to be 80 ns at 15 K.

CHAPTER VI

Electrically Injected InAs/GaAs Quantum Dot Spin Laser

6.1 Introduction

The ability to control and/or modulate the output polarization of lasers [87, 88] to electrically switch between orthogonal polarization states [89–91] would be useful for a host of applications including coherent detection systems, optical communications with enhanced bandwidth, secure communication and cryptography, and optical switching. The output polarization of semiconductor lasers is determined by the polarization properties of the active (gain) region and optical cavity. Vertical cavity surface emitting lasers (VCSELs) exhibit very poor polarization selectivity, stability and control. The in-plane fundamental transverse mode of these devices is randomly oriented [92, 93], and polarization stability is usually obtained by introducing anisotropy in the gain curve of different competing polarization modes (gain anisotropy) or by various schemes of mirror or cavity asymmetry [94].

Polarization control in lasers may be obtained with injection and recombination of spin polarized carriers and the output polarization is related to the spin polarization of carriers in accordance with the relevant selection rules for the conservation of angular momentum in the gain medium [95, 96]. Recombination of spin-up and spin-down electrons yields two coherently-coupled lasing modes, producing left-

and right-circularly polarized light, respectively. In a non-magnetic laser, these two modes are pumped equally, producing two equal and in-phase circularly polarized modes which combine to form linearly polarized light. For 100% spin polarization of the injection current, a pure circularly polarized output is theoretically estimated, while for spin injection less then 100%, the circularly polarized light is superimposed on the linearly polarized emission to yield an elliptically polarized output. Additionally, the threshold current is reduced with injection of spin-polarized carriers, and for 100% spin polarized injection, the threshold is ideally reduced by a factor of 2. The first demonstration of an optically pumped spin-polarized vertical-cavity surface-emitting-laser (spin-VCSEL) was made by Rudolph *et al.* [97].The laser active region consisted of pseudomorphic InGaAs/GaAs quantum wells. The devices were operated at 6 K and both polarized light output and threshold reduction were demonstrated. The same group have subsequently demonstrated a room temperature spin-VCSEL with GaAs/AlGaAs quantum wells [98]. The first electrically injected spin-VCSEL, with InGaAs/GaAs quantum well gain medium, was demonstrated recently by Holub *et al.* [59].The lasers were operated at 50 K and a maximum threshold current reduction of 11% and output degree of circular polarization of 23% were observed. Spin injection of electrons were accomplished with a Fe/AlGaAs Schottky tunnel diode.

For application of spin-polarized lasers, it is imperative that they are operated at high temperatures. At these temperatures, the electron spin relaxation time τ_s is determined by the D'Yakonov-Perel' (DP) spin scattering process [75]. In InGaAs quantum wells, $\tau_s = 6$ ps at room temperature [99], which is much lower than the radiative lifetime of 100 ps. On the other hand, the discrete density of states and the spatial localization of carriers in quantum dots (QDs) inhibit both the DP

and phonon scattering processes, which reduce the spin relaxation time and a weak temperature dependence of τ_s is expected [100]. The characteristics of an InAs/GaAs self-organized QD VCSEL is described here. The VCSEL is operated at 200 K. A maximum threshold current reduction of 14% and output optical polarization of 8% are measured in these devices.

6.2 Growth and Fabrication

Circular post spin-VCSELs, schematically shown in Fig. 6.1, were grown by MBE

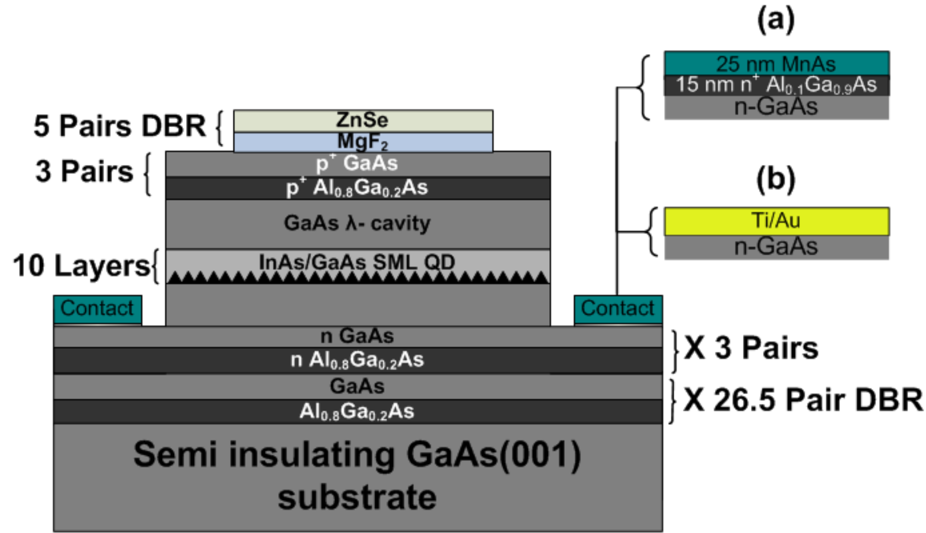

Figure 6.1: Schematic cross section of an InAs QD spin-VCSEL heterostructure with (a) magnetic and (b) nonmagnetic n-contact grown by MBE.

and fabricated using standard optical lithography, wet chemical etching, polymide planarization and passivation, contact and interconnect metallization, and dielectric electron beam evaporation techniques [59]. The InAs QDs density in the active region is 3×10^{10} cm^{-2}. The device mesa diameters varied from 15 μm to 30 μm. To form the spin polarized electron injector contact, MnAs/n^+-$Al_{0.1}Ga_{0.9}As$ Schottky barrier heterostructure was selectively regrown by MBE after a mesa definition. The mesa top surface and side walls were protected during re-growth by a $\sim$2 μm thick SiO_2

layer which was formed by PECVD and subsequently patterned to reveal the annular n^+-GaAs contact layer. After a high temperature annealing for oxide removal from the GaAs surface, 15 nm n^+-$Al_{0.1}Ga_{0.9}As$ ($N_D = 10^{19}$ cm^{-3}) and 25 nm MnAs were epitaxially grown at 630 and 250 °C, respectively. Non-magnetic control VCSELs were also fabricated with the same mesa dimensions, but with a Ti/Au bilayer serving as the n-contact. The top DBR mirror was formed with 5 pairs of ZnSe/MgF_2 deposited by electron beam evaporation.

6.3 Threshold Current Reduction and Output Circular Polarization

The quantum dot spin-VCSELs were mounted in a magneto-optical cryostat equipped with a 7 T superconducting magnet. The devices were characterized at T = 200 K under continuous wave (CW) bias operation and in the Faraday geometry. Hence the MnAs spin injector was magnetized along the hard axis. The chosen operating temperature of 200 K is low enough such that enough spin-polarized electrons would reach the QD active region and create a gain anisotropy. The lasing wavelength and the linewidth of the lasers were 983 nm and 0.28 nm, respectively. These values are consistent with the interband transition energy as determined from the low temperature photoluminescence measurements. The degree of circular polarization of the output, Π_c was analyzed using a photoelastic modulator (PEM) operating at 50 kHz and a Glan-Thompson linear polarizer, and the signal was detected and recorded with a silicon avalanche photodiode, low-noise preamplifier and by using lock-in techniques. The measured values of Π_c as a function of magnetic field, for a device with mesa diameter 15 μm and biased at $1.05 \times I_{th,0}$ (the threshold current for this device at zero magnetic field, $I_{th,0}$, is 13.8 mA), are shown in Fig. 6.2.

The value of Π_c saturates at 8% at a magnetic field of ~2 T. On the other hand, Π_c

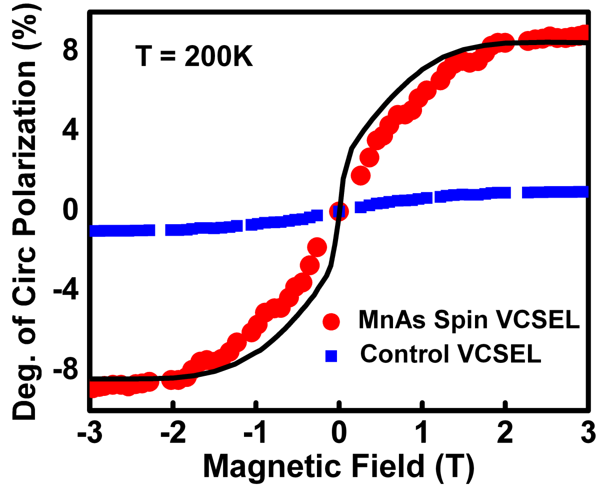

Figure 6.2: Measured degree of output circular polarization vs magnetic field for a 15 μm mesa diameter MnAs spin-VCSEL (circle) and control VCSEL (square) measured at 200 K are shown. The spin-VCSEL polarization closely follows the out-of-plane magnetization curve for MnAs.

for the control VCSEL, shown in the Fig. 6.2, is $< 0.5\%$. Also shown in the figure is the room temperature out-of-plane magnetization of MnAs film epitaxially grown on GaAs. It is evident that Π_c closely tracks the magnetization of the MnAs layer and provides evidence of electron spin injection at the MnAs Schottky tunnel diode as the source of the observed output polarization.

In order to eliminate the possibility of the observed output polarization being attributed to stray field effects directly from the MnAs contact layer and Zeeman effect, we had previously characterized an identically designed VCSEL with an Fe contact layer formed on top of a ~0.45 μm non-magnetic ohmic contact metallization [59]. The measured Π_c was $< 1.5\%$. We also performed magneto-photoluminescence measurements on the same device with linearly polarized laser excitation and observed a negligible value of Π_c, which indicates that a parasitic contribution from magnetic circular dichorism is absent in these devices.

To measure the reduction in threshold current ΔI_{th}, due to injection of spin

polarized carriers, magnetic field dependent optical power measurements were performed at 200 K in the Faraday geometry using a silicon photodiode and current pre-amplifier, with the devices under the CW operation. The measured light current characteristics and the reduction in I_{th} as a function of applied magnetic field are shown in Fig. 6.3. Again, the reduction saturates at $\sim$2 T corresponding to the

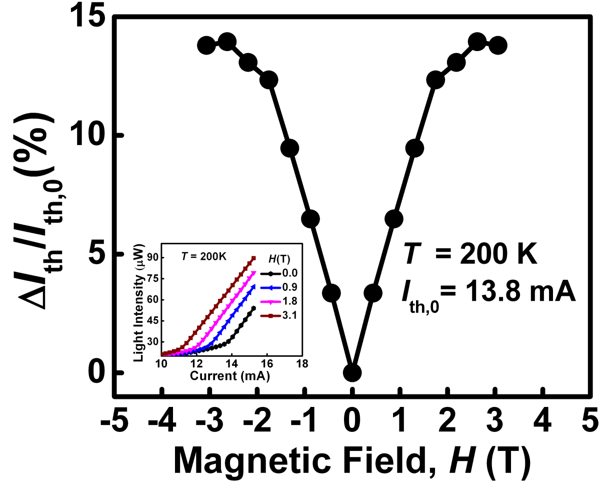

Figure 6.3: Threshold current reduction vs magnetic field for a 15 μm mesa diameter MnAs spin-VCSEL measured at 200 K. Inset shows the measured light-current characteristics.

magnetization saturation of the MnAs contacts. No reduction in threshold current is observed for the non-magnetic quantum dot spin-VCSELs.

The reduction in the threshold current in the presence of a magnetic field is accompanied by an enhancement in light emission, $\Delta L = \eta_D \, \Delta I_{th}$, where ΔL is the differential quantum efficiency and η_D is the slope efficiency. The measured emission enhancement as a function of injection current, for different values of magnetic field, are shown in Fig. 6.4(a). A peak emission enhancement of 37% is recorded at 3.1 T. When biased near threshold, a small difference in spin polarization of the injected carriers can result in a large difference in the intensities of the two circular polarizations due to gain anisotropy, provided the spin relaxation time is greater than the carrier lifetime. The gain anisotropy and the resulting polarization anisotropy will

decrease with increasing injection and eventually disappear with the onset of gain saturation. This explains the observed peaking of the emission enhancement at $I/I_{th} \cong 1$ in Fig. 6.4(a) and an identical trend of the threshold current reduction shown

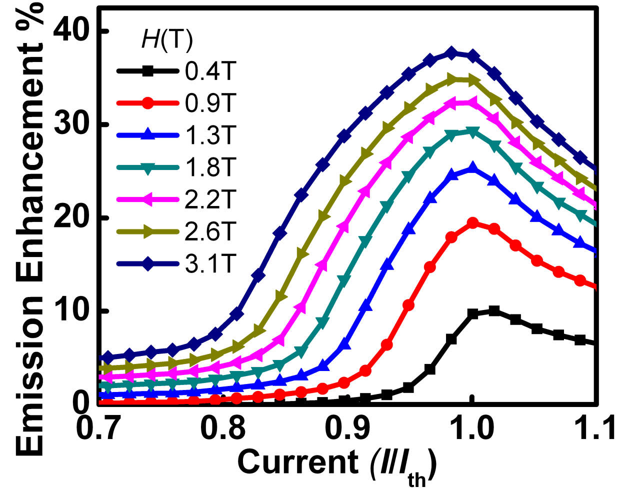

(a)

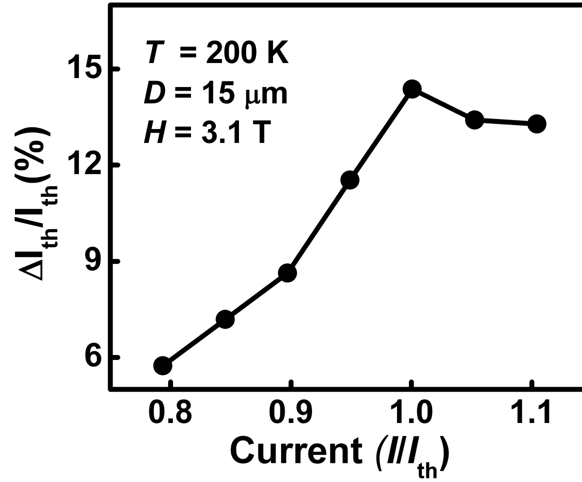

(b)

Figure 6.4: (a) Emission intensity enhancement vs normalized current (I/I_{th}) measured for different magnetic fields; (b) variation in threshold current reduction ($\Delta I_{th}/I_{th}$) vs normalized current (I/I_{th}) measured at a magnetic field of 3.1 T.

in Fig. 6.4(b). Due to gain anisotropy, the threshold current of the favored mode is reduced at the expense of the mode with opposite polarization whose threshold increases.

6.4 Modeling of QD spin-VCSEL

The dynamic properties of the QD spin-VCSEL were analyzed with the spin polarized carrier-photon coupled rate equations including non-linear gain compression effects [97, 101]. The device and material parameters used, for operation at 200 K, are given in Table 6.1. The transparency current density in the cavity is varied to

Table 6.1: Quantum dot parameters at 200 K used to analyze spin laser performance characteristics

Parameter	Symbol	Value	Reference
Differential gain	$\partial g/\partial n$	4.5×10^{-14} cm^2	[102]
Gain compression factor	ϵ	4.5×10^{-17} cm^{-3}	[59]
Rad. recombination coeff	B_{sp}	9.4×10^{-10} cm^{3}s^{-1}	[59]
Auger recombination coeff	C	1.5×10^{-27} cm^{6}s^{-1}	[103]
Carrier capture time	τ_{cap}	45 ps	[104]
Spin-flip time in barrier	$\tau_{s,b}$	50 ps	[99]
Spin-flip time in QD	τ_{sf}	75 ps	[100]
Photon group velocity	v_g	8.7×10^9 cm s^{-1}	[59]
Optical confinement factor	Γ	0.024	[59]
Spontaneous emission factor	β	6×10^{-4}	[105]
Photon lifetime	τ_{ph}	1.25 ps	[59]

fit the measured threshold currents. The calculated variation of threshold current reduction with injection current spin polarization is shown in Fig. 6.5(a). Thus for the measured I/I_{th} = 14% the required P_{spin} = 15%, corresponding to which the spin polarization in the QD active region and barriers at $I = I_{th}$ are calculated to be 5.8% and 8.5%, respectively. This is the point of maximum gain anisotropy and it may be noted that the output polarization of 8% is larger than the QD spin polarization of 5.8%. As the spin injection current is increased, the density of both spin polarizations approaches n_{th}, the gain anisotropy is reduced, and the QD spin polarization approaches zero and the measured output polarization of the laser is determined by the barrier polarization of 8.5% (Fig. 6.5(b)). It is to be noted that the

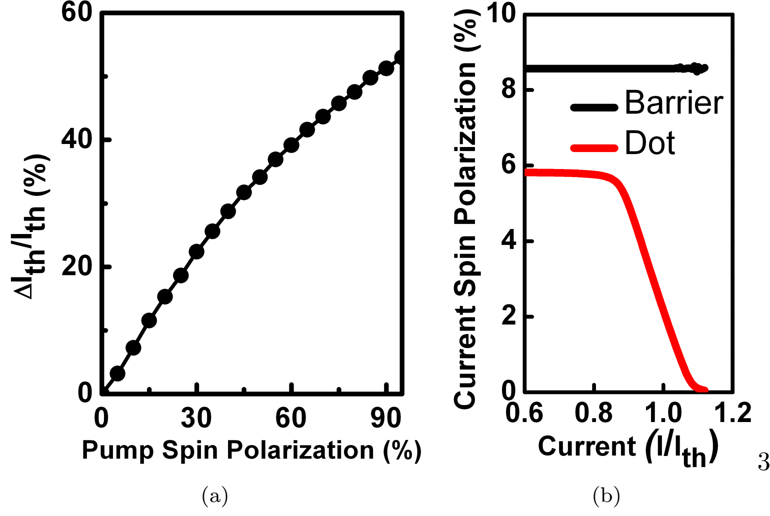

(a) (b)

Figure 6.5: (a) Calculated threshold current reduction vs pump-current spin polarization for spin relaxation time $\tau_{sf} = 75$ ps; (b) calculated variation of the spin polarization values in the barrier and in the QDs vs normalized current.

dominant depolarization for the spin-polarized carriers occur during the transport process, when the spin polarization decreases from 31% at the spin injector to 5.8% at the QDs.

6.5 Conclusion

We demonstrate a QD spin-VCSEL operating at 200 K. To operate the device at room temperature, the mesa diameter of the devices need to be reduced to 2-3 μm in order to decrease the effects of spin relaxation due to transport from the contacts to active region, which is perfectly feasible. It would also be desirable to increase P_{spin}. The latter is primarily determined by the spin polarization in the ferromagnetic spin injector. For MnAs the spin polarization is ~31% [19] and for Fe, the value is 45% . With these values it would be difficult to attain the theoretical maximum current reduction of 50%.

CHAPTER VII

Optical Polarization Modulation and Gain Anisotropy in an Electrically Injected Spin Laser

7.1 Introduction

The output polarization characteristics of semiconductor lasers are determined by the polarization properties of the gain medium and optical cavity and are therefore difficult to predict, stabilize, or control [90, 93, 106]. The ability to dynamically switch between orthogonal polarization states, preferably with the bias current, offers a novel and elegant technique for secure communication in a lightwave network. Other envisaged applications include reconfigurable optical interconnects, study of vitamins and asymmetric photochemical synthesis [107]. Spin-polarized lasers also promise reduced threshold current [59, 98], enhanced emission intensity and optical communication with enhanced bandwidth [38].

In electrically pumped spin polarized light sources, a non-equilibrium spin population is injected from a magnetic contact to the forward biased active region of a diode consisting of non-magnetic semiconductors [108]. The active region can be a bulk semiconductor, or quantum structures such as quantum wells, wires, or dots [109]. The selection rules for the conservation of angular momentum directly relate the spin orientation of the carriers transported to the active region to the polarization of photons emitted upon their radiative recombination [110]. While these relations hold

for spontaneous emission, such as in a spin light-emitting diode (LED), they do not reflect the output polarization in a spin laser [98] due to the non-linear dynamics and the spin polarization in the gain medium (active region), which gives rise to a large gain anisotropy at biases near threshold. As a result, the output polarization can be much larger than the spin polarization of the injected carriers. This is intuitively understood and has also been observed by us in quantum well spin lasers [59], but the exact magnitude of the output polarization and the parameters and dynamics upon which it depends have been hitherto unknown. In the present study we have derived the analytical form of the output polarization Π_C , threshold current $I_{th}(H)$, and the threshold current reduction $\Delta I_{th}/I_{th,0}$, as determined by gain anisotropy. In particular, we have highlighted the role of the diffusive transport of spin-polarized electrons from the ferromagnetic contact to the active region. The calculated values of these parameters are in excellent agreement with values obtained from the first measurement of electrical modulation of a InAs/GaAs QD spin-VCSEL with MnAs ferromagnetic contacts, schematically shown in Fig. 7.1. The QD active region al-

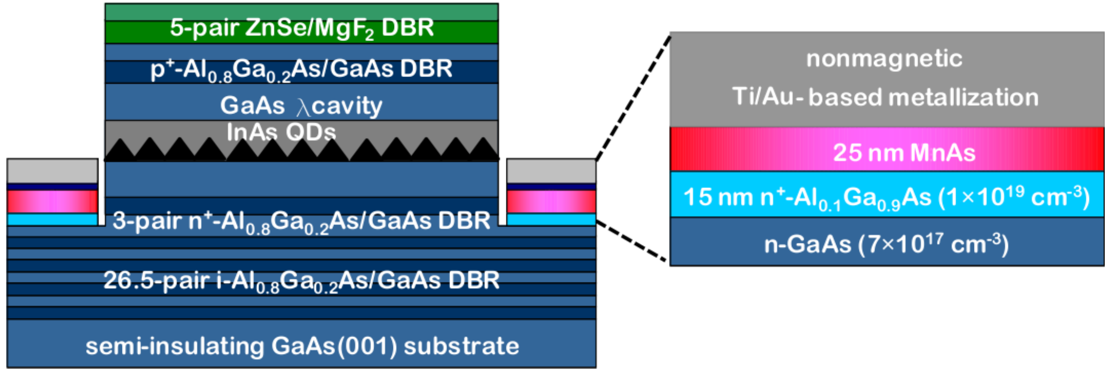

Figure 7.1: Heterostructure of GaAs-based spin-VCSEL grown by molecular beam epitaxy. The active (gain) region consists of 10 periods of self-organized InAs/GaAs quantum dots placed in a GaAs -cavity. The top DBR mirror consists of 5 pairs of ZnSe/MgF_2 deposited by PVD. The ferromagnetic MnAs/$Al_{0.1}Ga_{0.9}As$ tunnel injector contact is regrown selectively on GaAs after a mesa-etch stop, as shown in the figure.

lows high temperature operation since the spin relaxation time in the dots, limited by the DP spin scattering process [35], is enhanced due to carrier confinement. The present study provides a comprehensive insight to the operation and characteristics of an electrically injected spin-polarized semiconductor laser.

7.2 Analytical Determination of Laser Ouput Parameters and Gain Anisotropy

An important aspect which has to be taken into account in any spin laser, edge- or surface-emitting, is the diffusive spin transport from the ferromagnetic contact to the active region. Spin polarization at a distance x from the ferromagnetic contact at $x = 0$ (see Fig. 7.2) is governed by [111],

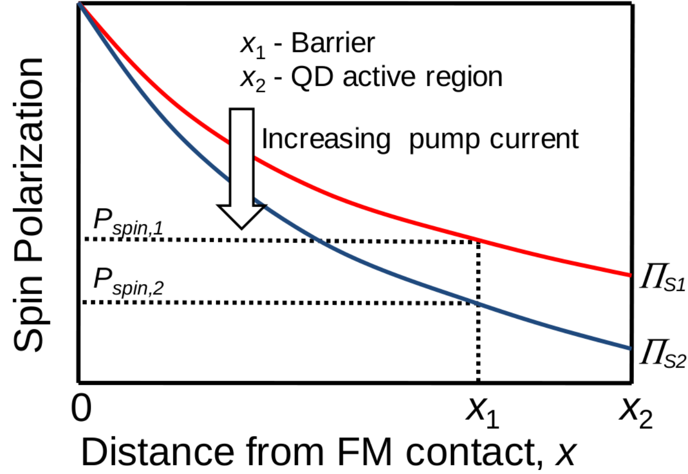

Figure 7.2: Schematic representation of the variation of carriers spin polarization with distance from ferromagnetic contact (MnAs) in VCSEL in accordance with the spin diffusion equation. The barrier (cavity) is at distance x_1 and the quantum dot region is at distance x_2. The spin polarization decreases with increasing pump current. In the barrier and quantum dots the polarization decreases from $P_{spin,1}$ to $P_{spin,2}$ and Π_{S1} to Π_{S2}, respectively.

$$\frac{\partial^2(N^+ - N^-)}{\partial x^2} = \frac{N^+ - N^-}{\lambda_{sf}^2} \tag{7.1}$$

where λ_{sf} is the spin diffusion length in the transport medium and $N^+(x)$ and $N^-(x)$ are the spin-up and spin-down carrier densities at any point x. Drift of spin-polarized

carriers is neglected since the doping densities in the transport region is relatively high (5×10^{17} cm^{-3}) [111] . These functions are valid from the contact up to the barrier (cavity) region *i.e.* $x = x_1$. For $x > x_1$ the polarization is governed by the laser parameters. Also, we know that the ferromagnetic contact polarization is given by,

$$P_{contact} = \Pi(x = 0) = \frac{N^+(x = 0) - N^-(x = 0)}{N^+(x = 0) + N^-(x = 0)} \tag{7.2}$$

The value of $P_{contact}$ is known from a measurement of the out-of-plane magnetization of the MnAs contact as a function of H [112], the spin dependent density of states of MnAs [50] and the spin injection efficiency at the MnAs/GaAs tunnel barrier [19].

The dynamics of carrier and photon densities in semiconductor lasers are governed by the coupled rate equations, which can be easily expanded to include the spin polarization of the carriers and the circular polarization of the photons as [98],

$$\frac{\partial n_b^\pm}{\partial t} = -\frac{n_b^\pm}{\tau_{cap}} + \frac{1 \pm P_{spin}}{2}\frac{I_{pump}}{qV_b} \mp \frac{n_b^+ - n_b^-}{\tau_{s,b}} \tag{7.3}$$

$$\frac{\partial n^\pm}{\partial t} = \frac{V_b}{V_{QD}}\frac{n_b^\pm}{\tau_{cap}} - v_g g(n^\pm, S^\pm)S^\mp \mp \frac{n^+ - n^-}{\tau_s} - B_{sp}n^\pm(n^+ + n^-) - Cn^\pm(n^+ + n^-)^2 \tag{7.4}$$

$$\frac{\partial S^\pm}{\partial t} = \Gamma v_g g(n^\mp, S^\pm)S^\pm + \Gamma\beta B_{sp}n^\mp(n^+ + n^-) - \frac{S^\pm}{\tau_{ph}} \tag{7.5}$$

where $n_b^\pm$ are the spin-up and the spin-down carrier densities in the barrier, $n^\pm$ are the spin-up and spin-down carrier densities in the active (gain) region, $S^\pm$are the densities of the right- and left-circularly polarized photons, τ_{cap} is the carrier capture time into the active (gain) material, P_{spin} is the degree of spin polarization of the pump current (I_{pump}) at the edge of the barrier region (point x_1 in Fig. 7.2), $\tau_b(\tau_s)$ is the spin-flip time in the barrier (QD), V_b (V_{QD}) is the volume of the barrier (QD), B_{sp} is the radiative recombination coefficient, C is the Auger recombination, v_g is

the group velocity of light, Γ is the optical confinement factor, β is the spontaneous emission factor, and τ_{ph} is the photon cavity lifetime. The non-linear gain in the active region is expressed in terms of gain compression factor ϵ as,

$$g(n,S) = \frac{dg}{dn}(n - n_{tr})/(1 + \epsilon S) \tag{7.6}$$

where dg/dn is the differential gain and n_{tr} is the transparency carrier density. Since the laser is operated very close to threshold where the gain anisotropy is a maximum, $\epsilon S \ll 1$, hence $g(n,S) \cong g(n)$.

The laser rate equations and the spin diffusion equation are solved with the objective of obtaining analytical forms of the threshold current (and hence the threshold current reduction) and output polarization as a function of applied magnetic field. In solving these equations, we define a set of intermediate parameters. These are the spin polarization at any point $x(0 \leq x \leq x_1)$, $\Pi(x)$, the quantum dot spin polarization, Π_S, and the average barrier polarization, $\Pi_{s,b}$. It should be noted that $P_{spin} \equiv \Pi(x_1)$ is not an independent parameter, but is related to $\Pi_{s,b}$ via the rate equations as $P_{spin} = \Pi_{s,b}(\tau_{cap}/\tau)$, where $1/\tau = 1/\tau_{cap} + 2/\tau_{s,b}$. On the other hand the degree of circular polarization of the output, $\Pi_C = (S^+ - S^-)/(S^+ + S^-)$, and the light output $L = S^+ + S^-$ are measurable quantities. From the derivation (Appendix D) we get,

$$I_{th}(H) = qV_{QD}\left[\frac{1}{\Gamma}\frac{S_{th}}{\tau_{ph}} + \frac{Bn_{th}^2(1-\beta)}{(1+\Pi_s)^2} + \frac{Cn_{th}^3}{(1+\Pi_s)^3}\right] \tag{7.7}$$

where S_{th} is the photon density at threshold. Hence, knowing $I_{th,0}$, the percentage threshold current reduction, $\Delta I_{th}(H)/I_{th,0}$ is given by,

$$\frac{\Delta I_{th}(H)}{I_{th,0}} \cong \frac{\Pi_S(\Pi_S + 2)}{(1+\Pi_S)^2} \tag{7.8}$$

Similarly, the output polarization is given by,

$$\Pi_c(H, I_{pump}) = -\Pi_s \frac{1 + \Gamma v_g \tau_{ph}\frac{dg}{dn} n_{tr}}{1 + \Gamma v_g \tau_{ph}\frac{dg}{dn} n_{tr} - \Gamma v_g \tau_{ph}\frac{dg}{dn} n_{th}(1 - \Pi_s)} \tag{7.9}$$

The gain anisotropy parameter for the laser is defined as,

$$g_A(H, I_{pump}) = \frac{g(n^+)}{g(n^-)} \cong \frac{1+\Pi_S}{1-\Pi_S} \tag{7.10}$$

A detail derivation of the model equations are given in Appendix D.

7.3 Role of Spin Diffusion on Output Polarization

The output circular ppolarization, threshold current reduction and gain anisotropy are calculated using the model equations are the following device and material parameters [75, 102, 105, 113]: τ_{cap} = 45 ps, $\tau_{s,b}$ = 300 ps, τ_s = 150 ps, $dg/dn = 3.4 \times 10^{-14}\text{cm}^2$, $n_{tr} = 4 \times 10^{17}$ cm^{-3}, $n_{th} = 4.66 \times 10^{18}$ cm^{-3}, $\epsilon = 4.5 \times 10^{-17}$ cm^{-3}, B_{sp} $= 9.4 \times 10^{-9}$ cm^{3}s^{-1}, $C = 1.5 \times 10^{-27}$ cm^{6}s^{-1}, $v_g = 8.7 \times 10^9$ cm s^{-1}, $\Gamma = 0.024$, $\beta = 6 \times 10^{-4}$, τ_{ph} = 0.1 ps, $P_{contact}$ = 0.31, and $\lambda_{sf} = 0.6 \times 10^{-4}$ cm. The gain anisotropy as described by Eqn. 7.10 is plotted in Fig. 7.3. The threshold current of

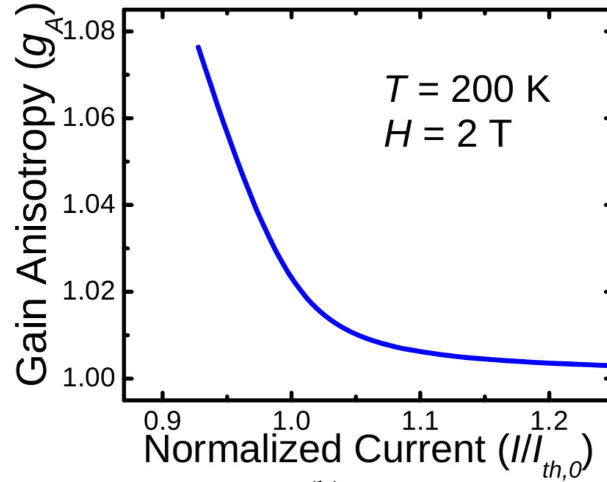

Figure 7.3: Calculated variation of gain anisotropy parameter with normalized pump current.

a spin laser is lower than that of an identical laser with non-magnetic contacts. As the pump current reaches threshold, the carrier concentration of the polarized lasing mode with higher gain (say S^+) becomes clamped at n_{th}. Further increase in pump current will increase the carrier concentration of the mode with lower gain (S^-), till

n_{th} is reached for this mode also and the mode will lase. It is easily seen that the spin polarization in the QD active region will steadily decrease as the injection increases beyond the point where the first threshold (for S^{+}) is reached. This is also the overall threshold for the laser. Intuitively, it is expected that in the injection regime between the thresholds for S^{+} and S^{-}, the output polarization will steadily increase and then decrease after the threshold for S^{-} is crossed. However, considering the transport of injected spin-polarized carriers from the ferromagnetic contact to the active region by spin diffusion, the pump spin P_{spin} also decreases, as illustrated in Fig. 7.2. This leads to a decrease in output circular polarization as soon as the pump current increases beyond the threshold (for S^{+}) (Fig. 7.4). Thus the intuitive picture

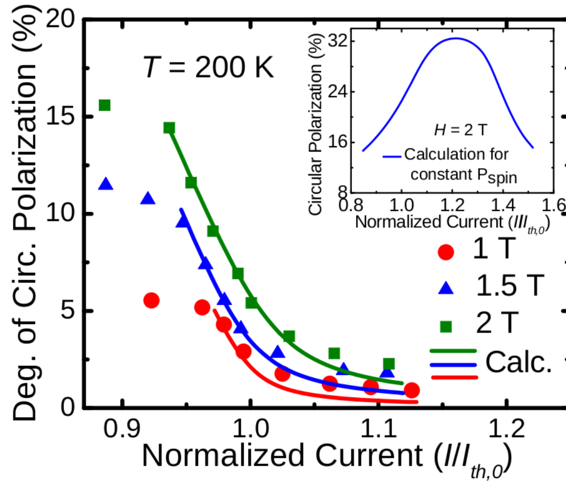

Figure 7.4: Calculated and measured modulation of output circular polarization of InAs/GaAs QD spin-VCSEL as a function of normalized pump current at different magnetic fields.

of the variation of output polarization would be valid only if diffusive transport of injected carriers is neglected and P_{spin} is held constant (inset to Fig. 7.4). It is of interest to note that the threshold current reduction, given by Eqn. 7.8 and plotted in inset to Fig. 7.5, is determined exclusively by Π_S. Therefore, parameters such as gain and differential gain of the active material, or the quality factor of the laser cavity will not play a role in threshold current reduction.

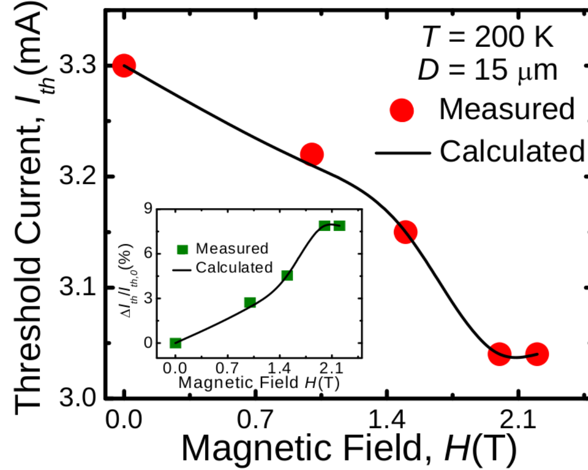

Figure 7.5: Calculated and measured reduction of threshold current with magnetic field applied perpendicular (hard axis) to the plane of the MnAs contact. The inset shows the calculated and measured percentage reduction of threshold current with field.

7.4 Device Growth and Fabrication

Measurements have been carried out on spin-polarized quantum dot VCSELs. In particular we have measured the reduction in the threshold current due to spin injection of electrons and the electrical modulation of the output polarization. We also choose an operating temperature of 200 K, which is low enough to allow enough spin polarized electrons to reach the QD active region from the MnAs Schottky tunnel contact. The laser hetrostructure shown in Fig. 7.1 is grown by MBE. The InAs quantum dot density in each of the 10 layers is approximately 3×10^{10} cm^{-2}, as measured by scanning tunneling microscopy. The dot layers are incorporated in a GaAs λ-cavity and the bottom and top mirrors are formed by 29.5 pairs of GaAs/$Al_{0.8}Ga_{0.2}As$ and 5 pairs of ZnSe/MgF_2 deposited by electron beam evaporation, respectively. Circular post devices with mesa diameters from 15-30 μm diameter were fabricated by standard optical lithography, wet chemical etching, polymide planarization and passivation, contact and interconnect metallization, and dielectric electron beam evaporation techniques. As illustrated in Fig. 7.1, a MnAs (25 nm)

$/n^+$-$Al_{0.1}Ga_{0.9}As$ (15 nm) Schottky barrier hetrostructure is selectively regrown after a mesa definition, to form the spin polarized electron injector contact [30]. The regrowth is done on an annular n^+-GaAs surface which is delineated by patterning an SiO_2 layer. The latter also serves to protect the mesa top and sidewalls during regrowth. The regrowth of the tunnel junction is critical in the context of electron spin injection [18]. Before regrowth, a high temperature annealing of the exposed GaAs surface is done at 630 °C for 2 mins. and subsequently the $Al_{0.1}Ga_{0.9}As$ ($N_D = 1 \times 10^{19}$ cm^{-3}) and MnAs layers are grown at 625 and 250 °C, respectively. We have earlier measured the injected spin polarization at identical MnAs tunnel injectors to be 31% [19]. Identical control VCSELs were also fabricated with a Ti/Au non-magnetic contact replacing the MnAs injector.

7.5 Polarization Modulation and Threshold Current Reduction

The lasers were mounted in a magneto-optical cryostat for measurements, which were done in the Faraday geometry. Hence the MnAs layer was magnetized along the hard axis. All measurements reported here were carried out on 15 μm diameter VCSELs at 200 K and current biasing to the lasers was in the continuous wave mode. The lasing output wavelength is 983 nm, which corresponds to the ground state electron-hole transition in the quantum dots at 200 K. The change (reduction) in threshold current due to spin injection of electrons was accurately derived from the measured change in the total light intensity (output power) for a fixed current bias, upon application of a magnetic field, and the measured slope of the light-current characteristics at zero field. The measured reduction of the threshold current is also plotted in Fig. 7.5 and there is good agreement with the calculated

values. A maximum threshold current reduction ($\Delta I_{th}/I_{th,0}$) of $\sim$8% is measured at $H = 2.1$ T, at which field the saturation of the out-of-plane magnetization of MnAs contact also occurs. No threshold reduction is observed for the non-magnetic VCSEL. The output polarization, Π_C, is analyzed using a PEM operating at 50 kHz and a Glan-Thompson linear polarizer. The signal is detected and recorded with a silicon avalanche photodiode and low-noise preamplifier and by using lock-in techniques. For a fixed bias current, the measured value of Π_C as a function of the applied magnetic field follows the measured out-of-plane magnetization of the MnAs contact very closely. In comparison the observed polarization of the non-magnetic VCSEL is negligible. The modulation of the output polarization Π_C with bias current was measured at different saturation magnetic fields and the data are shown in Fig. 7.4. Again, the agreement with calculated results is very good. This is the first demonstration of electrical modulation of the output polarization of a semiconductor laser. We define a modulation index as $\Delta\Pi_C/\Delta(I/I_{th})$ and this parameter is plotted in Fig. 7.6 as a function of normalized current. The index goes through a maximum

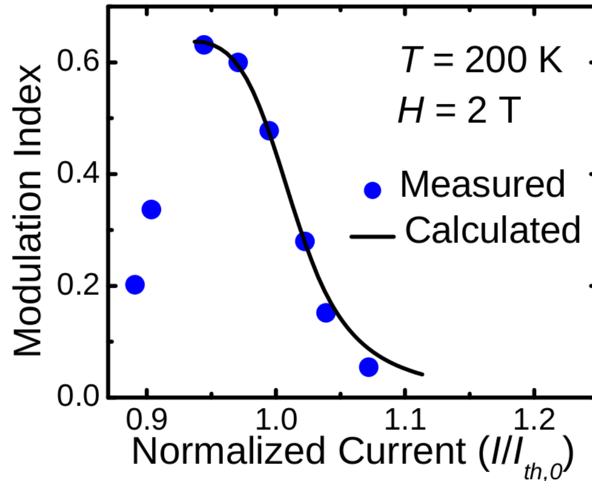

Figure 7.6: Measured modulation index versus pump current. The calculated values are shown for currents at and above threshold.

value of 0.6 at $I/I_{th,0} \cong 1$.

7.6 Conclusion

In conclusion, we have studied the effects of spin-induced gain anisotropy in spin polarized lasers. Analytic expressions have been derived for threshold current reduction, output polarization and the gain anisotropy parameter, taking into account the diffusion of spin polarized carriers from the ferromagnetic contact to the active region and the spin-coupled laser rate equations. The validity of the derivations is endorsed by excellent agreement of calculated values of Π_C and $\Delta I_{th}(H)/I_{th,0}$ with those obtained from measurements made with spin VCSELs having InAs/GaAs self-organized quantum dots as the gain media. The device measurements clearly indicate that room-temperature operation can be demonstrated with smaller diameter VCSELs, such that the transport length of spin injected carriers is reduced. This will also enhance P_{spin} and the output polarization. The calculated data in the inset to Fig. 7.4 indicates that if the transport length is very small, as with very small diameter VCSELs or edge-emitting lasers, and if the injected spin polarization is large, then the gain anisotropy will assist in the realization of output polarizations of $\sim$50% or higher at room temperature.

CHAPTER VIII

A Monolithically Integrated Magneto-Opto-Electronic Circuit

8.1 Introduction

Semiconductor spintronics is aimed at improving the operation and functionality of conventional devices in terms of speed, power and packing density [40, 75]. Significant advances in this area have been made, such as the demonstration of discrete devices like spin-valves [19, 20, 25, 39], spin-current amplifiers [71], spin capacitors [114], spin LEDs [31], and spin lasers [59, 112] using ferromagnet/semiconductor heterostructures. New physical phenomena involving spin with the potential for device applications have also been unravelled [26]. Most of these devices have been demonstrated with GaAs-based platforms, on which matured microelectronic and optoelectronic technologies also exist. For future applications with new paradigms and functionalities, it is of interest and importance to monolithically integrate spintronic devices with microelectronic and optoelectronic devices, to form a MOEIC. To cite a couple of applications, the spintronic devices will make the MOEICs inherently reprogrammable and will enable them to be included in the important class of reconfigurable integrated circuit (IC). The MOEIC will also allow spin information to be transmitted over distances much longer than the spin-diffusion length. In analogy with micro-electro-mechanical systems (MEMS), the integration of spintronic

devices with other conventional devices can have multiple benefits. We demonstrate here, for the first time, the characteristics of a MOEIC on GaAs, which is realized by the monolithic integration of a spin valve, an amplifier circuit containing high electron mobility transistors (HEMTs) and passive elements, and a LED. Variation of magnetic information is amplified and read out by photons emitted by the LED.

8.2 A Magneto-Electronic Switch Based on MOEIC

Spintronics has been included as a part of the ITRS as an emerging field with the potential to sustain the scaling of device feature sizes for performance improvement [2]. It presents a couple of additional advantages compared to other emerging areas: (1) it contributes equally to electronic and optoelectronic devices; and (2) it has the potential to be integrated with other semiconductor devices for varying functionalities [115]. The integration of magnetic, optoelectronic and electronic devices is facilitated by the fact that the fabrication steps for semiconductor spintronic devices are analogous to the conventional micro-fabrication techniques. We present here an MOEIC wherein a lateral semiconductor spin-valve, a cascaded HEMT amplifier and an LED are monolithically integrated to demonstrate a magneto-electronic switch. A spin-valve has two ferromagnetic contacts acting as polarizer and analyzer [19]. The resistance of the spin-valve is low if both polarizer and analyzer are magnetized in the same direction and high if they are magnetized in opposite directions. The magnetoresistance resulting from parallel to anti-parallel magnetization configurations is usually small and at times difficult to detect. The cascaded HEMT amplifier in the integrated circuit amplifies the magnetoresistance [116]. A change in the gate-to-source voltage of the HEMT changes the drain-to-source current and hence the device acts as a transconductance amplifier. A cascaded configuration is used to

increase the amplifier gain. The large change in the current of the second HEMT is used to drive the LED. The light intensity of the LED changes in proportion to the change in the drain-to-source current [117] of the second HEMT. Hence, the circuit operation can be described in the following sequential steps: (1) a magnetic field (H) changes the resistance of the spin-valve; (2) the magnetoresistance is amplified by the cascaded HEMT amplifier to a large change in current; and (3) the LED light intensity is modulated by the changing current. The MOEIC therefore converts the spin-polarization in the channel region of the lateral spin-valve to an equivalent change in light intensity of the LED. The circuit operates as a magneto-electronic switch which modulates the light intensity of the LED.

8.3 Principle of Operation

The circuit diagram of the MOEIC is shown in Fig. 8.1. The spin-valve [resistance $R(H)$] and resistor R_1 are connected in series between gate and source terminals of the first HEMT (HEMT_1). A current bias I_B is applied, which creates a gate-to-source bias voltage, $V_{GS1} = I_B(R + R_1)$. A small change in resistance ΔR (magnetoresistance, $MR = \Delta R/R$) changes V_{GS1} by v_{gs1}, which in turn changes the drain-to-source current, I_{DS1} by i_{ds1}. These quantities are related by the transconductance ($g_{m1} = \partial I_{DS1}/\partial V_{GS}$) of HEMT_1 as, $i_{ds1} = g_{m1} v_{gs1} = I_B(g_{m1}\Delta R)$, where $g_{m1}\Delta R$ is the gain of the first stage of the cascaded amplifier. The output of HEMT_1 is connected to the gate terminal of HEMT_2. The change in the gate-to-source voltage of HEMT_2 is given by, $v_{gs2} = -i_{ds1}R_2$, where R_2 is the bias resistor in the HEMT_1 drain terminal. The negative sign is due to the fact that an increase in i_{ds1} decreases v_{gs2}. The gain of the second stage amplifier is $g_{m2}R_2$, where g_{m2} is the transconductance of HEMT_2. The change in the drain-to-source current of HEMT_2

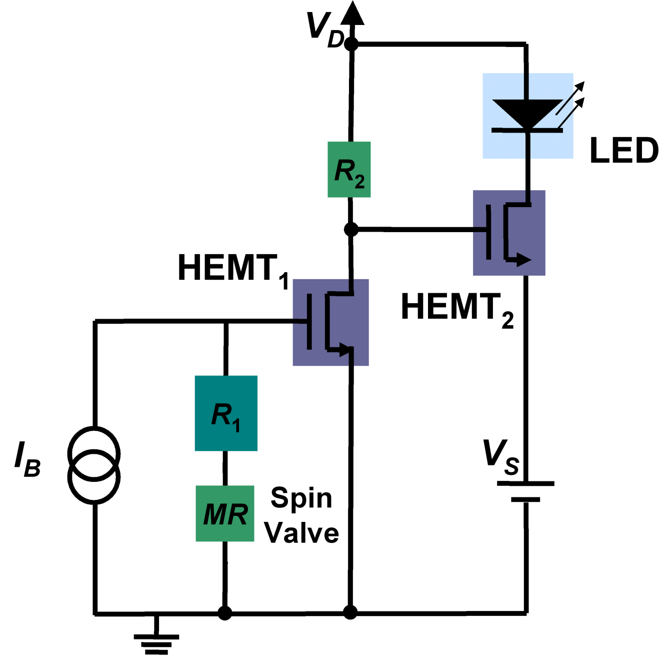

Figure 8.1: A schematic of the magneto-opto-electronic integrated circuit. A magnetic field changes the resistance of the spin-valve. The magnetoresistance is amplified by the cascaded transconductance HEMT amplifier to a large change in drain-to-source current which modulates the light intensity of the LED. The resistors R_1 and R_2 are used to correctly bias the cascaded HEMT amplifier in the linear region.

is therefore given by $i_{ds2} = -I_B(g_{m1}\Delta R)(g_{m2}R_2)$, which is also the change in the current flowing through the LED. If the slope of the light-output versus input-current (L–I) characteristics of the LED is η ($= \partial L/\partial I$), the resultant change in the light output is given by,

$$\Delta L \quad = \quad -I_B \left[g_{m1}\Delta R\right] \left[g_{m2}R_2\right] \eta \qquad (8.1)$$

Hence, the change in the light intensity is directly proportional to the change in resistance in the linear region of operation of the amplifier. If the quiescent (Q) drain-to-source current of HEMT$_2$ is $I_{DS2,Q}$, the fractional change in light intensity is given by,

$$\Delta L/L_0 \quad = \quad -I_B \left[g_{m1}\Delta R\right] \left[g_{m2}R_2\right] \eta \,/L(I_{DS2,Q}) \qquad (8.2)$$

where $L_0 = L(I_{DS2,Q})$ is the light-output at the quiescent drain-to-source current $I_{DS2,Q}$. When the amplifier operates in the linear region, $HEMT_2$ operates in the saturation region. $I_{DS2,Q}$ is therefore independent of R and the fractional change in light intensity (Eqn. 8.2) is also independent of R. Hence, the magnetoresistance amplification is primarily dependent on the external circuit parameters and independent of the absolute value of MR.

8.4 Growth and Fabrication

A schematic of the MOEIC heterostructure grown by molecular beam epitaxy (MBE) is shown in Fig. 8.2. The heterostructure consists of epitaxially grown layers for the MnAs/GaAs lateral spin-valve [19], the GaAs/$Al_{0.2}Ga_{0.8}As$ multi-quantum-well LED [117], and the $Al_{0.2}Ga_{0.8}As$/ $In_{0.2}Ga_{0.8}As$ pseudomorphic HEMT [116], all separated by undoped GaAs buffer layers. The spin-valve is grown as the last (uppermost) device which has ferromagnetic MnAs as the top layer. This avoids the necessity for epitaxial growth on MnAs, which is very difficult. The LED heterostructure is grown beneath the spin-valve to minimize out-diffusion of Be from the p-doped layer during subsequent thermal cycling. The heterostructure for the HEMT is grown first and is therefore at the bottom. The fabrication of the MOEIC circuit is done in the following sequence: spin-valve, resistance R_1, LED, HEMT, resistance R_2, interconnect and contact metallization. The nominal value for R_1 and R_2 are designed to be 175 Ω and 1 kΩ, respectively. Figures 8.3(a) and (b) show a three-dimensional (3D) schematic and a micro-photograph (before the final interconnect and metallization steps) of the MOEIC, respectively. The fabrication procedure is described in Appendix E. The circuit layout ensures good surface morphology. Circuits with additional contact terminals for individual access to the circuit elements

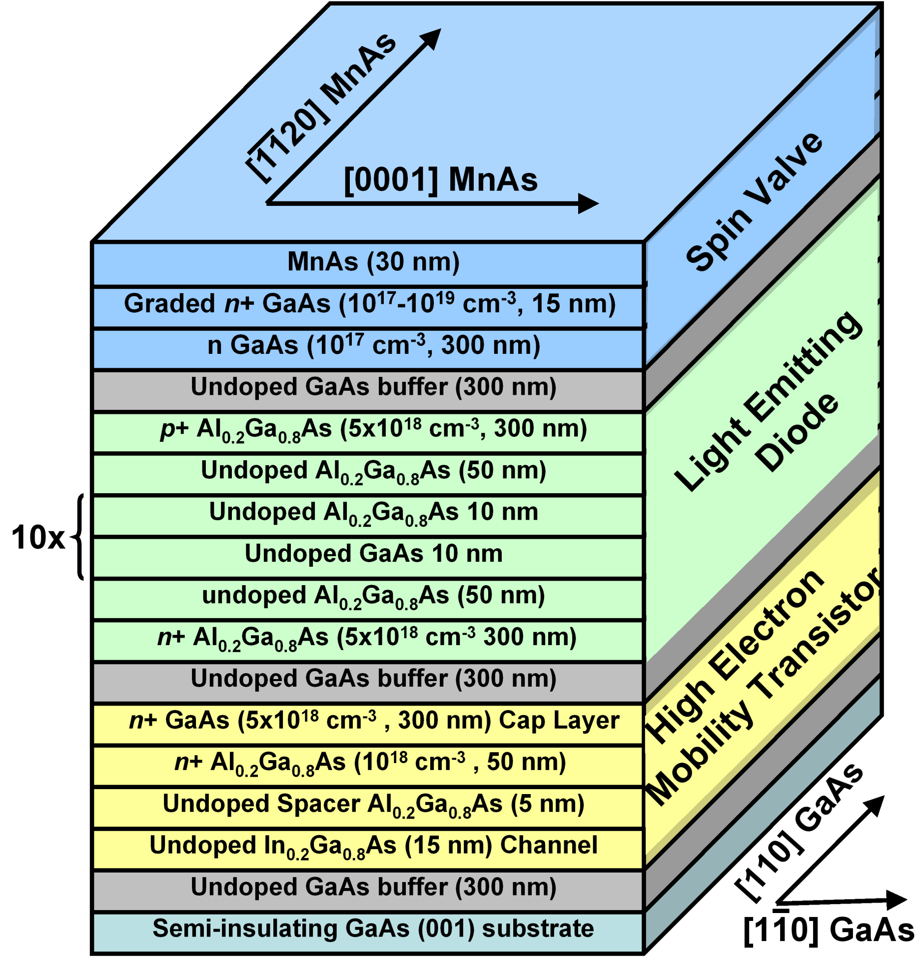

Figure 8.2: A schematic of the MOEIC heterostructure grown by MBE. The heterostructure consists of epitaxially grown layers for the MnAs/GaAs lateral spin-valve, the GaAs/$Al_{0.2}Ga_{0.8}As$ multi-quantum-well LED and the $Al_{0.2}Ga_{0.8}As$/$In_{0.2}Ga_{0.8}As$ pseudomorphic HEMT separated by undoped GaAs buffer layers.

are also fabricated to trace signal flow as it moves from input to output. Control devices were also fabricated to confirm spin dependency of the observed effects.

8.5 Characteristics of Circuit Elements

Measurements are done by mounting the MOEIC samples in a cryostat, placed between the poles of an electromagnet. Figure 8.4 (a) shows the spin-valve characteristics as the magnetic field is varied from -2 kG to 2 kG. It can be seen that the resistance is low when polarizer and analyzer are magnetized in the same direction

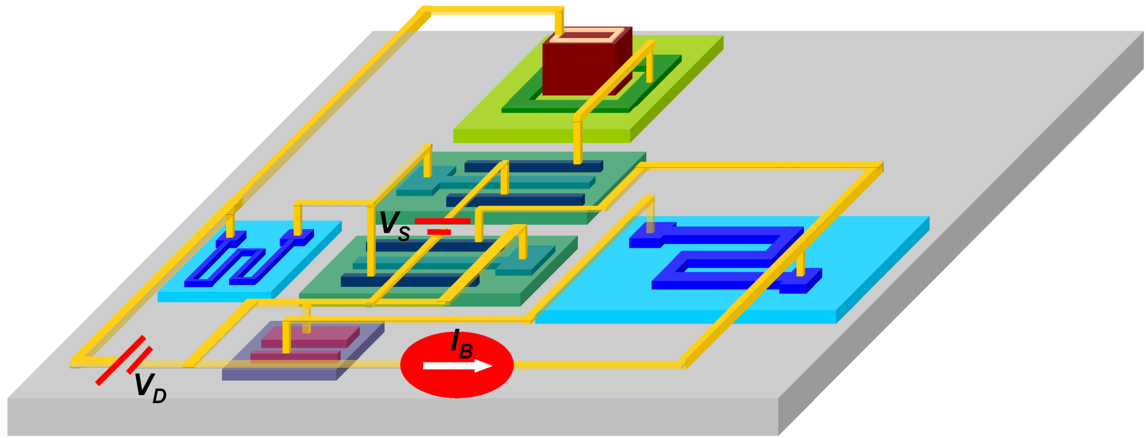

(a)

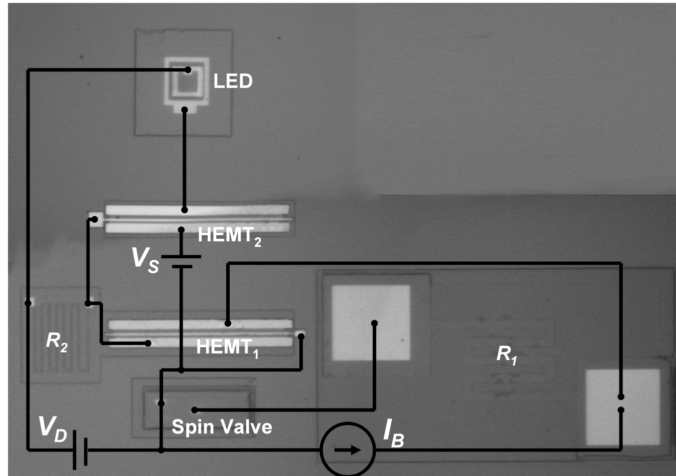

(b)

Figure 8.3: (a) A schematic and (b) a micro-photograph of the fabricated MOEIC (before the final interconnection and metallization step). The resistors R_1 and R_2 are delineated on undoped GaAs buffer layers by physical vapor deposition and lift-off technique.

for large magnetic fields and high when they are magnetized in opposite directions ($|H| = 1.2$ kG). A peak magnetoresistance of 0.33% is measured at 20 K. The Hanle effect (spin precession in a perpendicular magnetic field) measurement were also done to ensure spin dependency of the observed effect (Fig. 8.4(b)). The measured magnetoresistance is smaller than reported earlier [19] and is due to the fact that annealing of HEMT source and drain contacts introduces undesirable MnAs/GaAs interface mixing, which reduces spin injection and detection efficiencies. Control

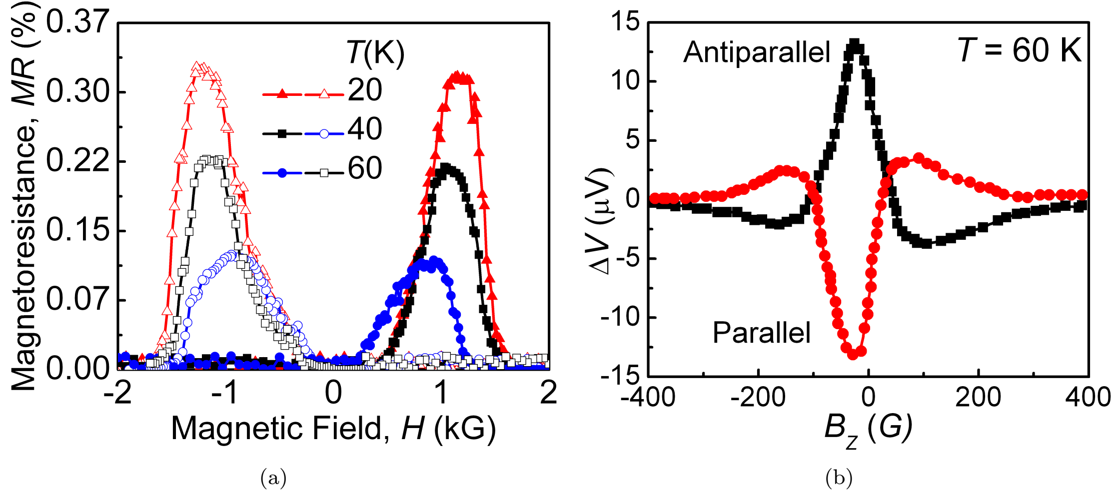

(a)

(b)

Figure 8.4: (a) The spin-valve shows two magnetoresistance peaks corresponding to the case when the polarizer and the analyzer are magnetized in opposite directions. The magnetoresistance decreases with increasing temperature due to decreasing spin-relaxation time; (b) non-local voltage as a function of perpendicular magnetic field in a spin-valve. The spin precesses due to Hanle effect which leads to the change in spin accumulation. The asymmetry is due to a small misalignment of the sample and presence of a small axial magnetic field.

measurements were also done to ensure spin dependency of the effect [19, 71, 114]. Figures 8.5(a) and (b) show the measured characteristics of an isolated HEMT which has undergone all the processing steps as the MOEIC. Figure 8.5(a) shows g_m as a function V_{GS} for $V_{DS} = 2$ V . The threshold voltage V_{TH} is determined to be -1.9 V. Figure 8.5(b) depicts g_m as a function of temperature for $V_{DS} = 2$ V. These characteristics confirm that the HEMTs function as a voltage controlled current source. Figure 8.6(a) shows the measured L–I and I–V characteristics of an LED. Figure 8.6(b) shows the L–I characteristics as a function of temperature. The quantum efficiency and hence η increases with decreasing temperature. The individual circuit elements, therefore, exhibit the desired characteristics. It is also observed that the HEMT and LED characteristics do not change for magnetic fields $|H| \leq 3$ kG.

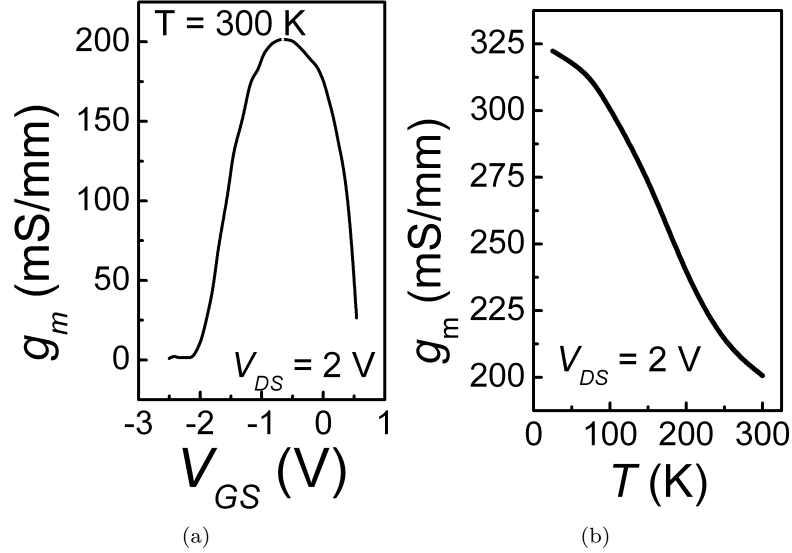

(a) (b)

Figure 8.5: (a) Transconductance g_m of the HEMT as a function of gate-to-source voltage. It reaches peak at V_{GS} = -0.9 V; (c) transconductance of the HEMT as a function temperature. It increases with decreasing temperature due to increasing mobility.

8.6 Circuit Operation of MOEIC

The MOEIC circuit operation is then measured by biasing it with voltage and current sources, as shown in Fig. 8.1. Both the HEMTs are biased with, $V_{GS1,Q} = V_{GS2,Q} = -1.5$ V and $V_{DS1,Q} = V_{DS2,Q} = 2$ V at 40 K. Transconductances g_{m1} and g_{m2} are then both equal to 175 mS/mm under this bias condition. Consequently, the quiescent currents through the HEMTs and LED are equal and are given by $I_{DS1,Q} = I_{DS2,Q} = I_{LED} \approx 5$ mA. The measured $R \approx 2.17$ kΩ, and hence a current bias $I_B = V_{GS1,Q}/(R + R_1)$ = -640 μA is applied to the input terminal. The drain bias voltage V_D is determined as, $V_D = I_{DS1,Q}R_2 + V_{DS1,Q} = 7$ V. The source voltage for HEMT$_2$ is then determined as, $V_S = V_{DS1,Q} - V_{GS2,Q} = 3.5$ V. The voltage across the LED is given by, $V_{LED} = V_D - V_{DS2,Q} - V_S = 1.5$ V. It is to be noted from the I–V characteristics in Fig. 8.6(e) that $I_{LED}(V_{LED} = 1.5\text{ V}) \approx 5$ mA $= I_{DS2,Q}$. Hence, the circuit is correctly biased at a stable operating point. A magnetic field is then swept and the LED light intensity is measured as a function

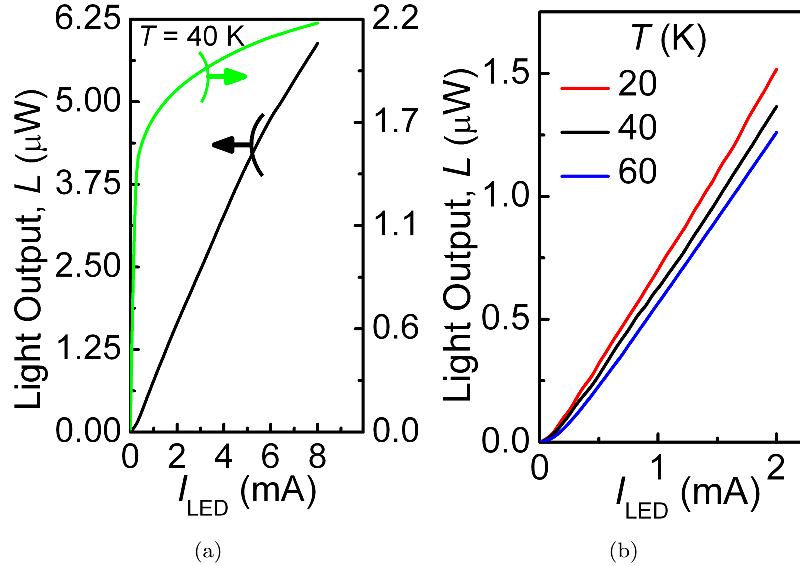

(a)

(b)

Figure 8.6: (a) LED light output and terminal voltage as a function of bias current; (b) light output versus bias current of the LED as a function of temperature. The quantum efficiency increases with decreasing temperature, hence, the slope increases.

of H at various temperatures with a silicon photodetector (Fig. 8.7). The light intensity modulation shows exactly the same magnetic field dependence as the spin-valve characteristics, as predicted by Eqn. 8.2. This confirms the spin-dependency of the observed change. The overall MOEIC gain, $(R/L).(\partial L/\partial R)$ is determined to be $\sim$20 in the temperature range of operation. As expected, the MOEIC amplifies the magnetoresistance of the spin-valve and acts as a magneto-electronic switch which modulates the LED light intensity in response to a varying magnetic field. The modulated light intensity, which can be transmitted over a long distance, bears the signature of spin-polarization in the spin-valve channel region.

8.7 Conclusion

In conclusion, we have demonstrated a magneto-opto-electronic integrated circuit which monolithically integrates a magnetic device, an optoelectronic device and an electronic device. We have shown that the circuit operates as a magneto-electronic

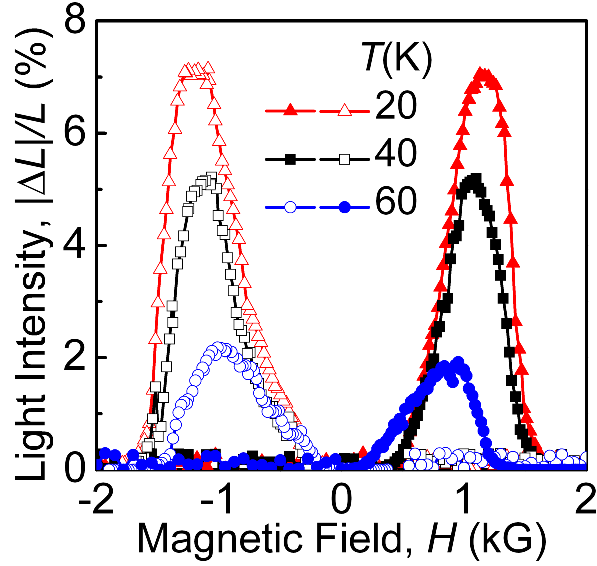

Figure 8.7: MOEIC characteristics. Modulation of LED light intensity as a function of magnetic field. The light intensity modulation shows exactly the same magnetic field dependence as the spin-valve characteristics. The magnetoresistance amplification is determined to be ∼20 in the region of operation. The MOEIC acts as a magneto-electronic switch which varies LED light intensity in response to an external magnetic field.

switch which controls the light intensity of an LED. The circuit can also be used to transfer spin information over a long distance on a chip or from chip to chip. The integration scheme will facilitate realization of ICs with new functionalities. The MOEIC demonstrated here is very versatile and all-metal magnetic devices (such as giant magnetoresistance (GMR)) and TMR devices can replace the semiconductor spintronic device for broader applications.

CHAPTER IX

Conclusion

9.1 Summary of Present Work

This thesis has designed and demonstrated several fundamental spintronic devices. The elemental nature of these devices make them very versatile and they are suitable for wide range of applications. Key results and conclusions from this research are highlighted below.

9.1.1 Epitaxially Grown MnAs/GaAs Lateral Spin-Valves

We have demonstrated for the first time electrical spin injection and detection in semiconductors using a MnAs/GaAs lateral spin-valve. We have measured a magnetoresistance of 3.6% at 10 K and 1.1% at 125 K. We have determined the spin-selectivity of the MnAs/GaAs tunnel barriers as 1.9 and a spin-polarization of 31% has been estimated beneath the source contact using the two-channel model. The channel length and bias dependent magnetoresistance measurements have indicated diffusive spin-transport of the spin-polarized carriers in the GaAs channel. The spin dependency of the observed effects have been confirmed from the results of well designed control experiments which eliminate spurious contributions from the ferromagnetic contact pads and the external magnetic fields. The results have been explained in the framework of spin injection, transport, and collection along with

micromagnetic simulations.

9.1.2 Amplification of Spin-Current Polarization

It is difficult to achieve large spin polarization into semiconductors and electrical control of such polarizations have remained elusive. We have designed and demonstrated an electrically controlled spin-current amplifier to circumvent this problem. An amplified spin-polarization of ∼100% has been experimentally measured in these devices. Large spin-polarizations have been achieved independent of temperatures. We have also introduced the concept of using a third terminal to provide an addition control input for output polarization. We have highlighted the importance of minimizing spin-drift to avoid non-linearity in the amplifier gain. The device can be extended to build logic and non-volatile memory devices.

9.1.3 Two Dimensional Spin Diffusion in Multi-Terminal Lateral Spin-Valves

Spin-based lateral multi-terminal devices are being explored for new functionalities and to discover new phenomena. However, most of these devices take into account only one dimensional spin-transport to ascertain the device response. We have discovered the importance of two dimensional spin transport to enhance the spin-polarization in a semiconductor. We have demonstrated that the spin-polarization in a three terminal geometry has exponential dependence on the geometric contact sizes. The spin-polarization has been greatly enhanced by decreasing the contact size and increasing the transverse spin-diffusion. An enhancement factor as large as 0.35 has been experimentally observed. The enhancement factor has been found to be larger when more charge current is drawn using the third terminal. We have also demonstrated that two dimensional spin-diffusion helps to minimize the effects of perturbation due to carrier extraction and restore the channel potential to its

equlibrium value.

9.1.4 Electrically Driven Spin-Dynamics of Paramagnetic Impurities: A Spin Capacitor

We have presented a new phenomenon where we have observed that paramagnetic impurities embedded in a semiconductor channel of an anti-parallel lateral spin-valve are driven electrically and they are spin-polarized in the process. We have used Mn doped MnAs/GaAs lateral spin-valves to demonstrate the effect. The Mn impurities cause spin-flip scattering and, since they do not have any significant alternative means of relaxation, get polarized in the process resulting in a decrease in the spin-flip current and hence the terminal current. The transient current through the device therefore bears the signature of the charging of the paramagnetic spins of the Mn atoms. The phenomenon also provide an easy method to determine the spin-spin scattering time constant between various magnetic impurities and conduction electrons. The time constant has been experimentally determined to be 120 ns at 10 K and 80 ns at 15 K for Mn impurities in the GaAs channel.

9.1.5 Electrically Injected InAs/GaAs Quantum Dot Spin Laser

We have demonstrated a quantum dot spin-VCSEL operating at 200 K. An output circular polarization of 8% and a threshold current reduction of 14% have been measured in these devices. The observed effects have been explained using the carrier-photon coupled laser rate equations. The spin dependency of the observed effects have been confirmed from the results of carefully designed controlled experiments which unambiguously demonstrate that the measured output circular polarization and threshold current reduction come solely from the spin-polarized carriers. The spurious contribution from external out-of-plane magnetic field has been found to be negligible. The devices can be operated near room temperature by reducing the

mesa diameter to ∼2-3 μm, which will reduce the transport length of spin-polarized carriers and therefore reducing the spin depolarization.

9.1.6 Optical Polarization Modulation and Gain Anisotropy in an Electrically Injected Spin Laser

We have studied the effects of spin-induced gain anisotropy in spin polarized lasers. We have demonstrated that the output polarization of the spin-laser can be modulated by varying the bias current near threshold. We have experimentally measured a peak modulation index of 0.6 at 200 K in these devices near threshold. Analytic expressions have been derived for threshold current reduction, output polarization and the gain anisotropy parameter, taking into account the diffusion of spin polarized carriers from the ferromagnetic contact to the active region and the spin-coupled laser rate equations. We have highlighted the importance of spin transport from ferromagnetic contact to the laser active region and the gain anisotropy on the operation of the spin lasers.

9.1.7 A Monolithically Integrated Magneto-Opto-Electronic Circuit

We have demonstrated a magneto-opto-electronic integrated circuit which monolithically integrates a magnetic device, an optoelectronic device and an electronic device. We have integrated a ferromagnet/semiconductor lateral spin-valve, a cascaded HEMT amplifier and a LED to operate as a magneto-electronic switch. An external magnetic field changes the resistance of the spin-valve; the small change in magnetoresistance is amplified by the cascaded HEMT amplifier which finally drives the LED. The LED light intensity is thus modulated in proportion to the change in the magnetoresistance. The circuit can also be used to transfer spin information over a long distance on a chip or from chip to chip. The integration scheme will facilitate realization of ICs with new functionalities. The MOEIC, we have demonstrated

here, is very versatile and GMR/TMR devices can replace the spin-valve for broader applications.

9.2 Suggestions for Future Work

9.2.1 Spin Based Read/Write Memory

Memory is a fundamental building block for microprocessors. High speed, low power and high density memories are essential so that information can be stored and retrieved by the arithmetic logic unit (ALU) of a micro-processor with minimum delay and low power consumption. Here, we propose a memory device with all the required characteristics, which can also be integrated with the proposed spin-transistor in Ref. [60].

A schematic of the proposed device is shown Fig. 9.1. The device is based on

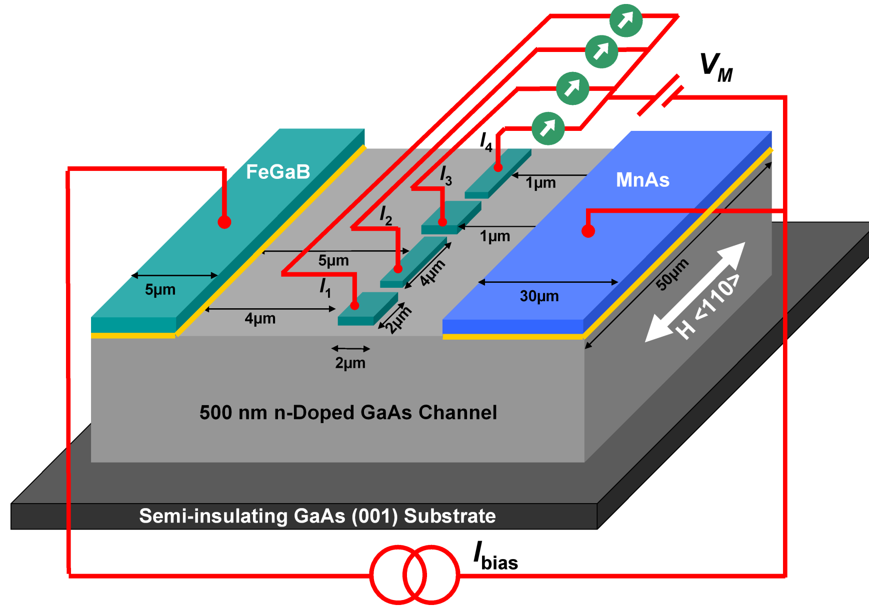

Figure 9.1: A schematic of the proposed spin-based memory device. The two large ferromagnetic contact pads act as source and drain, which create an electrochemical potential splitting in the anti-parallel configuration. The central ferromagnetic contact pads on the channel region act as memory bits.

a spin-current amplifier. It consists of two large ferromagnetic contact pads acting as source and drain. The source will be fabricated from FeGaB having a very low

coercivity (∼5 Oe) [118] and the drain contact is fabricated from MnAs having a larger coercivity (∼100 Oe). The device is operated with source and drain magnetized in opposite directions. There are several small FeGaB contact pads on top of the channel region, which act as memory bits. The coercivity is so chosen that the central contacts pads have the smallest coercivity compared to the source and drain contact pads. The channel region beneath the contact pads are heavily doped to create Schottky tunnel barrier for efficient spin injection and detection. [18]

Read Operation: The read operation is performed through spin-accumulation measurement with source and drain magnetized in opposite directions. The small memory bits are placed with its center coinciding with the center of the effective channel. It is shown earlier that the electrochemical potential difference is anti-symmetric (symmetric) with respect to the center of the channel when source and drain are magnetized in the same (opposite) direction (Chapter III). A read voltage V_M which is equal to the electrochemical potential at the crossover point is applied to the memory bits. Hence, there is no current flow in the parallel configuration as spin-up and spin-down electron currents are individually zero. The memory is operated with source and drain in the anti-parallel configuration. There is a finite electrochemical potential splitting at the center of the channel in this configuration. As shown earlier, the current flowing through the bits in the anti-parallel configuration is given by Eqn. 3.8 which is repeated here,

$$\frac{I_{D2}}{W_{D2}} = \int_{L1}^{L2} \left[G_{\uparrow} \left(V_{D2} - \frac{\mu_{\uparrow}}{e} \right) + G_{\downarrow} \left(V_{D2} - \frac{\mu_{\downarrow}}{e} \right) \right] dx \tag{9.1}$$

Hence, a non-zero current flows through the central contacts. The central contact pads have two specific sizes (different coercivities) acting as bits '1' and '0'. The magnitude and sign of the current flowing through the two contact pads depend on the orientation of the memory bits, which allow the read operation.

Write Operation: The write operation is performed through spin-torque phenomenon [10]. FeGaB has the unique property of very low coercivity which can be tuned by varying B concentration. Since the memory bits are fabricated from FeGaB, the magnetization directions can be easily changed by sending a large spin-polarized current through them. For write operation, the device is operated at higher bias between source and drain, which creates an even larger electrochemical potential splitting in the channel region as given by Eqn. 3.6. A large spin-polarized current flows through the memory bits, which enables write operation. The sign of the electrochemical potential splitting depends on the direction of bias current I_{bias}. Hence, the memory bits can be written in either direction ('1' or '0') by changing the direction of I_{bias}. It is to be noted that the memory is non-volatile in nature and therefore has zero off-state current, hence low power dissipation.

Figure 9.2 shows the hysteresis characteristics of FeGaB. It can be seen that

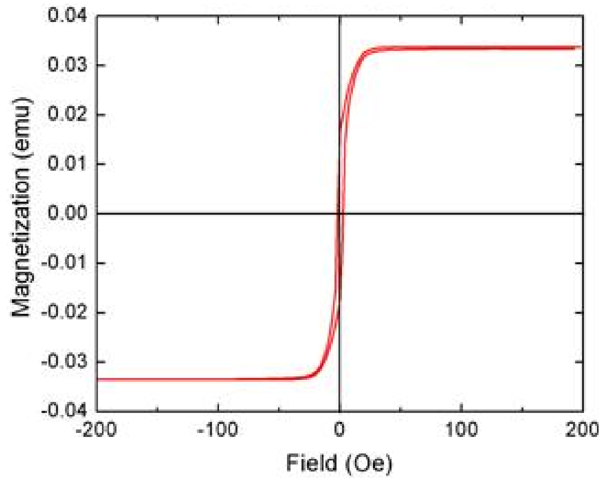

Figure 9.2: A typical hysteresis of a sputtered thin FeGaB film on GaAs. The coercivity is very small ∼1-2 Oe

the soft ferromagnetic property of FeGaB makes the hysteresis characteristics very narrow. The typical coercivities are found to be within ∼1-10 Oe, which makes it very suitable for electrical writing of magnetization directions. The read operation

of a 4 bit memory device is shown in Fig. 9.3. The currents flowing through the

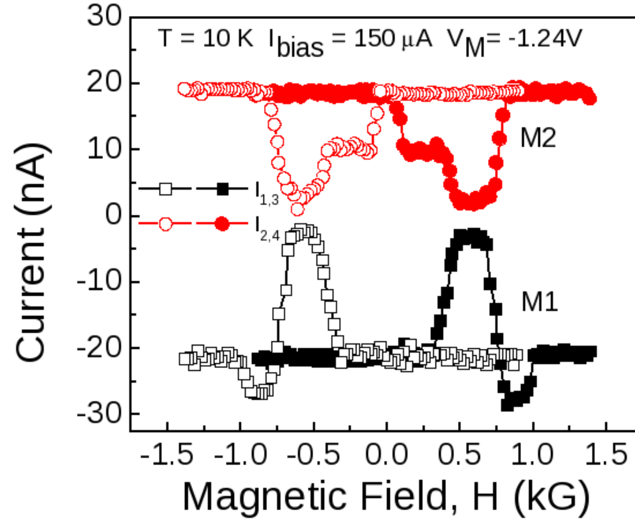

Figure 9.3: Read operation of the memory bits. The current flowing through through '0' (I_2 and I_4) and '1' (I_1 and I_3) have different signs.

two memory bits have different sign, which also gives a large noise margin for these devices. Since only a small finite electrochemical potential splitting is required for its operation, these devices is expected to operate at high temperatures. The concept is already verified in spin-current amplifiers which operate up to a temperature of 150 K. The devices need to be scaled down one order of magnitude to further increase the operating temperature to 300 K. It is to be noted that the device does not require any external magnetic field during operation. The device is permanently operated with source and drain magnetized in opposite directions, where the bit currents have opposite sign.

9.2.2 Spin Based Memory Array

We have recently demonstrated a monolithically integrated magneto-opto-electronic circuit where a spin-valve, a HEMT amplifier, and a LED are integrated to achieve a new functionality [119]. Here we propose a spin-based memory array by integrating spin-based memory and HEMT devices, which can be used to store large amount of

information. It will be possible to read and write blocks of information as required by any micro-processor.

A schematic of the memory array is shown in Fig. 9.4. Each block represents an 8

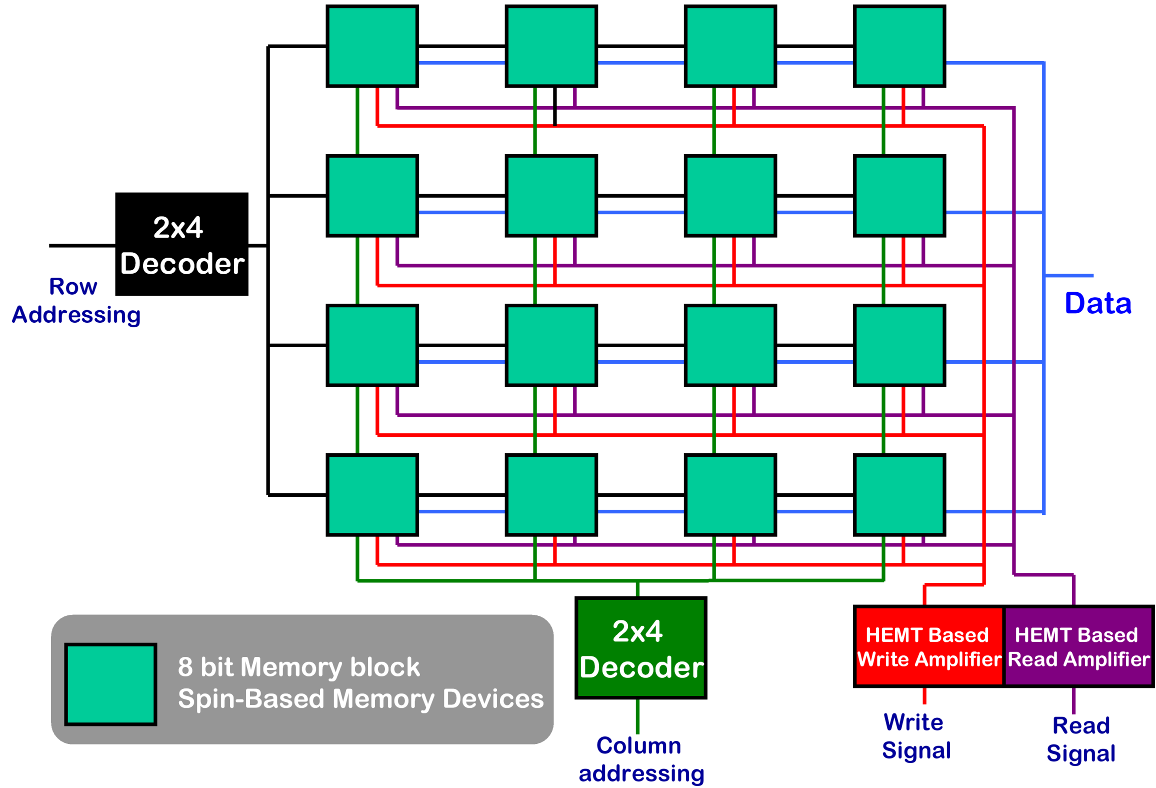

Figure 9.4: A schematic of the proposed spin-based memory array. The memory is arranged in a 4×4 array with monolithically integrated address and read/write circuits.

bit memory device shown in Fig. 9.1. The blocks are arranged in rows and columns. Since there are two rows and two columns, there are two 2×4 bit row and column address decoder to address a particular block (possible addresses 00, 01, 10 and 11). The read and write signals are generated by a HEMT based transmission gate which either enables the read path or the write path. The write signal strength (I_{bias}) is higher than the read signal as it will involve changing magnetization direction through spin-torque effect. All the memory blocks are connected to a common 8 bit data bus to take the information in and out of the memory array. Hence the memory operations can be depicted as follows:

- Addressing - A particular memory block in the array is selected by a two bit row address and a two bit column address.
- Data bus enabling - Data bus is enabled for reading/writing.
- R/W operation - Appropriate read/write signals are generated externally.

It is to be noted that data bus is enabled before the actual read/write signals are generated. This is done in order to ensure that information to be written is made available before enabling the write signal avoiding time synchronization problem and inadvertently writing wrong data into the memory block.

The proposed memory architecture has several advantages over traditional architectures: (1) off-state power requirement is zero, hence, there is no static power consumption; (2) power required for read cycle is very small (1-50 nW), which makes it very energy efficient; and (3) packing density is at least one order of magnitude higher as several memory bits can be laid out with single source and drain.

9.2.3 Light Sources with Large Polarization Injection

Spin-polarized light sources with large output polarization are very useful for secure communication and enhancing communication bandwidth. However, long spin transport length in spin-LEDs and spin-lasers reduces the actual injected polarization into the active region, which in turn reduces the output polarization. Here, we propose a device with a nearly 100% spin-polarized carrier injection into the active region. The light output from the device is also theoretically estimated to be 100% circularly polarized.

The device is based on a spin-current polarization amplifier [71] in which a large spin-current can be extracted using a third terminal placed on top of the semiconductor channel region. Here, we feed the extracted large spin-polarized current into the

active region of a microcavity spin-LED or a super-luminescent LED. A schematic of the device is shown in Fig. 9.5. This is a three terminal device like the spin-

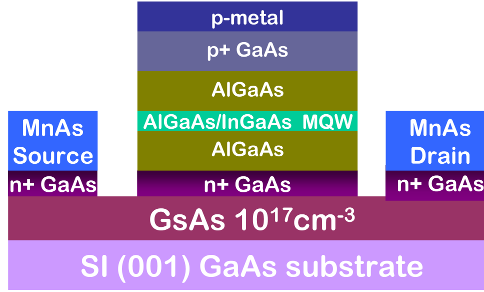

Figure 9.5: A schematic of the light source with large polarization injection

current amplifier, however the central contact is non-magnetic and consists of the heterostructure of an LED. The source and drain contacts are ferromagnetic. The central contact is delineated at the center of the source edge to drain edge channel distance. It is shown that the electrochemical potential in the channel region is described by Eqn. 5.1, and the electrochemical potential is related to the spin-carrier density by Eqn. 5.3. These two equations are solved self-consistently along with $n_{\uparrow}(x,t) + n_{\downarrow}(x,t) = n_0$ to determine the spin-current polarization in the active region. Using the typical values for MnAs/GaAs tunnel barrier, it is estimated that the devices will emit 100% spin-polarized light at room temperature for 1 μm channel length between anti-parallel source and drain.

The light intensity and the output polarization can be controlled by varying both the bias current and the central terminal collector voltage. The dual electrical control of the output imparts an unique characteristic to the device. The light intensity can be varied keeping the output polarization constant and vice versa.

Some of the preliminary results for this device is shown in Fig. 9.6. The device is fabricated with non-magnetic Ti/Au central contact (without the LED heterostructure) with 6 μm channel length. It can be seen that there is a current flowing through

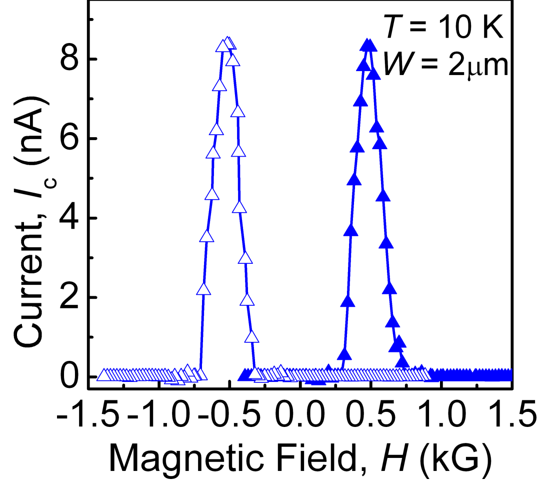

Figure 9.6: current through the Ti/Au non-magnetic central contact. The current is large when source and drain are magnetized in opposite directions.

the central contact for the case when source and drain are magnetized in opposite directions. The magnitude and sign of the current match well with that predicted by the theory. Since the spin-polarization is maximum with anti-parallel ferromagnetic source and drain, they can be permanently magnetized in this configuration, which will alleviate the need for any external magnetic field.

9.2.4 Room Temperature Edge Emitting Spin Laser

We have demonstrated spin-VCSELs using both quantum well and quantum-dot active regions [59, 112]. It is experimentally observed that the quantum-dot spin-VCSELs operate up to a temperature as high as 200 K. Theoretical model indicates that large spin-transport length in these devices prevents the operation at room temperature. Also, VCSELs require a very high out-of-plane magnetic field to magnetize the ferromagnetic contacts along hard axis.

Here we propose a spin-based edge-emitting laser which circumvents the problem of depolarization of electron spin during transport by reducing the spin-transport length to less than 0.5 μm. Also, edge-emitting lasers do not require an external

magnetic field. The ferromagnetic contacts inject spin-polarized carriers from remanent magnetization with in-plane quantization axis. The active region of the laser is a wide quantum well, which ensures in-plane orientation of heavy hole angular momentum. The circularly polarized light is collected from the edge. This configuration ensures that the quantum selection rule is satisfied for edge emitting lasers.

A schematic of the device is shown in Fig. 9.7. The device is designed with an

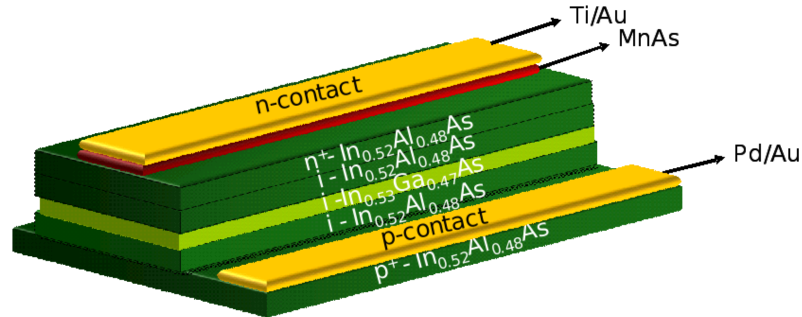

Figure 9.7: A schematic of the proposed edge emitting laser with an InP based lattice matched system. The top n-contact injects spin-polarized carriers into the InGaAs active region.

InP based lattice matched system, which has a much larger differential gain than GaAs. The top n-contact is ferromagnetic in nature, which injects spin-polarized electrons into the InGaAs active region. Using typical values for laser parameters and using Eqns. 7.8 and 7.9, an output circular polarization of ∼10% and a threshold current reduction of ∼15% are estimated at room temperature. Hence, a spin-based edge-emitting laser has the potential to overcome the limitations of a spin-VCSEL. The output circular polarization can be controlled by changing the bias.

Electrically changing the sign of the output polarization (along with the magnitude) is another desirable feature for the spin-laser. The above edge-emitting spin-laser can be fabricated with the modified n-contact as shown in Fig. 9.8(a) to achieve this functionality.

The n-contact, in this case, consists of two distinct size pads having distinctly dif-

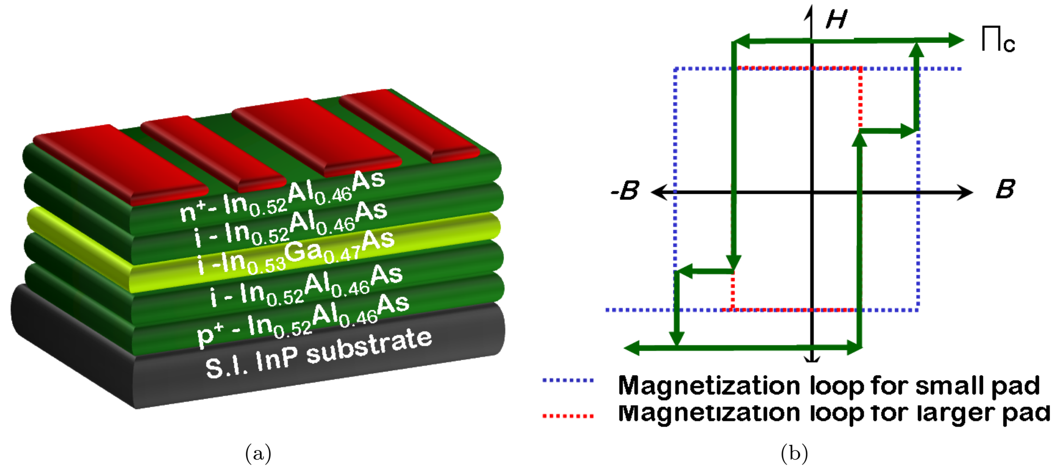

Figure 9.8: (a) A schematic of the edge-emitting laser for electrical switching of output polarization; (b) hysteresis characteristics of the n-contact pads.

ferent coercivities. The total magnetization of the n-contact is shown in Fig. 9.8(b). There are certain regions in the hysteresis where the two pads are magnetized in opposite directions. The device is operated in this anti-parallel configuration. A HEMT transmission gate can used to selectively inject currents through either of these two pads. The sign of $P_{contact}$ will change, which changes the sign of Π_c. The device will be able to do a high-speed polarization modulation in absence of magnetic field.

APPENDICES

APPENDIX A

Two-Channel Model for a Spin-Valve

The resistance $R_{\uparrow}$ ($R_{\downarrow}$) of the spin-up (spin-down) channel in Fig. 2.1 is given by,

$$\begin{aligned} R_{\uparrow} &= R_{\uparrow F} + R_{\uparrow TB} + 2R_n + R_{\uparrow TB} + R_{\uparrow F} \\ &= \frac{2\lambda_f}{W\left(1+\alpha_f\right)} R_{f\square} + R_{\uparrow TB} + 2\frac{L_{chan}}{W} R_{n\square} + R_{\uparrow TB} + \frac{2\lambda_f}{W\left(1+\alpha_f\right)} R_{f\square} \end{aligned} \quad (A.1)$$

$$\begin{aligned} R_{\downarrow} &= R_{\downarrow F} + R_{\downarrow TB} + 2R_n + R_{\downarrow TB} + R_{\downarrow F} \\ &= \frac{2\lambda_f}{W\left(1-\alpha_f\right)} R_{f\square} + R_{\downarrow TB} + 2\frac{L_{chan}}{W} R_{n\square} + R_{\downarrow TB} + \frac{2\lambda_f}{W\left(1-\alpha_f\right)} R_{f\square} \end{aligned} \quad (A.2)$$

where λ_f is the electron spin-flip length in MnAs, W is the channel width, α_f is the MnAs spin polarization, $R_{f\square}$ is the MnAs thin film resistance per square, $R_{n\square}$ is the channel resistance per square, $R_{\uparrow,\downarrow TB}$ is the tunnel barrier resistance, and L_{chan} is the channel length of the spin-valve. Similar equations can be written for the case when source and drain are magnetized in opposite directions. Hence, magnetoresistance $MR = \frac{R(\uparrow\downarrow)-R(\uparrow\uparrow)}{R(\uparrow\uparrow)}$ can be obtained in terms of known parameters. The tunnel barrier resistances are usually much larger than the ferromagnetic contact resistances ($R_{\uparrow,\downarrow TB} \gg R_{\uparrow,\downarrow f}$). Equations A.1 and A.2 simplify to,

$$R_{\uparrow,\downarrow} = 2\frac{L_{chan}}{W} R_{n\square} + 2R_{\uparrow,\downarrow TB} \quad (A.3)$$

Equation A.3 indicates that the tunnel barrier resistance dominates the spin dependent resistance for small channel length devices. The equivalent resistance of a small channel length spin-valve with analyzer and polarizer magnetized in the same direction is given by,

$$\begin{aligned} R(\uparrow\uparrow) &= \frac{R_\uparrow R_\downarrow}{R_\uparrow + R_\downarrow} \\ &= \frac{2\beta R}{1+\beta} \end{aligned} \tag{A.4}$$

where $R = R_{\uparrow TB}$, and $\beta = R_{\downarrow TB}/R_{\uparrow TB}$ is the tunnel barrier spin selectivity. A similar analysis with analyzer and polarizer magnetized in opposite directions results in,

$$R(\uparrow\downarrow) = \frac{R(1+\beta)}{2} \tag{A.5}$$

Hence the magnetoresistance of a small channel length spin-valve is given by,

$$MR = \frac{R(\uparrow\downarrow) - R(\uparrow\uparrow)}{R(\uparrow\uparrow)} = \frac{(\beta-1)^2}{4\beta} \tag{A.6}$$

Hence, magnetoresistance of an ideal spin-valve primarily depends on the spin selectivity of the tunnel barrier.

APPENDIX B

Modeling of a Spin-Current Amplifier

The spin-current amplifier (Chap. III) is divided into three regions – (I) the source region ($x < 0$), (II) the channel region ($0 < x < L_{chan}$), and (III) the drain region ($x > L_{chan}$). Solving the coupled spin-diffusion equations for region (I) we get the electrochemical potentials as,

$$\mu_{\uparrow(\downarrow)} = A + \frac{jxe}{\sigma_F} \tag{B.1}$$

where A is a constant to be determined from boundary conditions, j is the current density, e is the charge of an electron, and σ_F is the conductivity of the ferromagnet. It is assumed that the spin-diffusion length in the ferromagnet is very small. Hence, the currents through spin-up ($j_\uparrow$) and spin-down ($j_\downarrow$) channels are given by,

$$j_\uparrow = \frac{\sigma_\uparrow}{e}\frac{\partial \mu_\uparrow}{\partial x} = j\frac{\sigma_\uparrow}{\sigma_F} \tag{B.2}$$

$$j_\downarrow = \frac{\sigma_\downarrow}{e}\frac{\partial \mu_\downarrow}{\partial x} = j\frac{\sigma_\downarrow}{\sigma_F} \tag{B.3}$$

where $\sigma_\uparrow$ ($\sigma_\downarrow$) is the conductivity of the spin-up (spin-down) electrons in the ferromagnet. The electrochemical potentials in region (II) are given by,

$$\mu_\uparrow = B + \frac{jxe}{\sigma_N} + \frac{2E}{\sigma_N}\exp\left(-\frac{x}{\lambda_{sf}}\right) + \frac{2F}{\sigma_N}\exp\left(\frac{x - L_{chan}}{\lambda_{sf}}\right) \tag{B.4}$$

$$\mu_\uparrow = B + \frac{jxe}{\sigma_N} + \frac{2E}{\sigma_N}\exp\left(-\frac{x}{\lambda_{sf}}\right) + \frac{2F}{\sigma_N}\exp\left(\frac{x - L_{chan}}{\lambda_{sf}}\right) \tag{B.5}$$

where B, E and F are constants to be determined from boundary conditions, σ_N is the conductivity of the semiconductor channel, and λ_{sf} is the spin-diffusion length in the semiconductor. Similar to the region (I), currents through the two-channels in the region (III), with source and drain1 magnetized in the same direction, are given by,

$$j_{\uparrow} = \frac{j}{2}(1+\alpha_F) \tag{B.6}$$

$$j_{\downarrow} = \frac{j}{2}(1-\alpha_F) \tag{B.7}$$

where α_F is the spin-polarization of the ferromagnet. For the case when source and drain1 are magnetized in opposite directions, the currents are given by,

$$j_{\uparrow} = \frac{j}{2}(1-\alpha_F) \tag{B.8}$$

$$j_{\downarrow} = \frac{j}{2}(1+\alpha_F) \tag{B.9}$$

Using the boundary conditions that the spin-currents are continuous at $x = 0$ we get,

$$j\frac{\sigma_{\uparrow}}{\sigma_F} = \frac{j}{2}(1+\alpha_F) = \frac{G_{\uparrow}}{e}\left[\frac{2E}{\sigma_N} + \frac{2F}{\sigma_N}\exp\left(\frac{x-L_{chan}}{\lambda_{sf}}\right) - A\right] \tag{B.10}$$

$$j\frac{\sigma_{\downarrow}}{\sigma_F} = \frac{j}{2}(1-\alpha_F) = \frac{G_{\downarrow}}{e}\left[-\frac{2E}{\sigma_N} - \frac{2F}{\sigma_N}\exp\left(\frac{x-L_{chan}}{\lambda_{sf}}\right) - A\right] \tag{B.11}$$

Combining the above two equations we get,

$$E + F\exp\left(-\frac{L}{\lambda_{sf}}\right) = \frac{je\sigma_N}{8}\left(\frac{1+\alpha_F}{G_{\uparrow}} - \frac{1-\alpha_F}{G_{\downarrow}}\right) \tag{B.12}$$

Using the boundary condition that spin-currents are continuous at $x = L_{chan}$ for the case when source and drain1 are magnetized in the same direction we get,

$$E\exp\left(-\frac{L}{\lambda_{sf}}\right) + F = \frac{je\sigma_N}{8}\left(\frac{1+\alpha_F}{G_{\uparrow}} - \frac{1-\alpha_F}{G_{\downarrow}}\right) \tag{B.13}$$

Using the Eqns. B.12 and B.13 we get,

$$\frac{E}{F} = \gamma_{\uparrow\uparrow} = -1 \tag{B.14}$$

A similar derivation for the case when source and drain1 are parallel yields,

$$\frac{E}{F} = \gamma_{\uparrow\downarrow} = 1 \tag{B.15}$$

Combining Eqns. B.12-B.15 we get the Eqns. 3.6 and 3.7.

APPENDIX C

Spin-Dynamics in a Spin-Capacitor

C.1 Relation between Spin-Flip current and Spin-Carrier Density

The continuity equation for spin-up electrons is given by,

$$\frac{1}{e}\left[\nabla.\mathbf{J}_{\uparrow}\right] = \frac{\partial n_{\uparrow}}{\partial t} + \frac{n_{\uparrow} - n_{\downarrow}}{\tau_{\uparrow\downarrow}} \tag{C.1}$$

where e is the electronic charge, $\mathbf{J}_{\uparrow}$ is the spin-up electron current density, $n_{\uparrow}$ is the spin-up electron density, $n_{\downarrow}$ is the spin-down electron density, and $\tau_{\uparrow\downarrow}$ is the spin-relaxation time from spin-up to spin-down channel. Equation C.1 is integrated over the active volume of the channel region as,

$$\begin{aligned} \frac{1}{e}\int_V \left[\nabla.\mathbf{J}_{\uparrow}\right] dv &= \frac{\partial \left(A \int_x n_{\uparrow} dx\right)}{\partial t} + \frac{A \int_x \left(n_{\uparrow} - n_{\downarrow}\right) dx}{\tau_{\uparrow\downarrow}} \\ \Longrightarrow \frac{1}{e}\int_V \left[\nabla.\mathbf{J}_{\uparrow}\right] dv &= \frac{\partial N_{\uparrow}}{\partial t} + \frac{N_{\uparrow} - N_{\downarrow}}{\tau_{\uparrow\downarrow}} \end{aligned} \tag{C.2}$$

where A is the cross section of the channel. It is assumed that the variation of $n_{\uparrow}$ and $n_{\downarrow}$ in y direction is negligible (Fig. 5.1). The dimension along this direction is very small compared to the other parameters and the change is very small. Equation C.2 is simplified using the divergence theorem as,

$$\begin{aligned} \frac{1}{e}\oint_S \left[\nabla.\mathbf{J}_{\uparrow}\right].\mathbf{n} dS &= \frac{\partial N_{\uparrow}}{\partial t} + \frac{N_{\uparrow} - N_{\downarrow}}{\tau_{\uparrow\downarrow}} \\ \Longrightarrow \frac{1}{e}[I_{\uparrow,\mathrm{A}}(t) - I_{\uparrow,\mathrm{P}}(t)] &= \frac{\partial N_{\uparrow}}{\partial t} + \frac{N_{\uparrow} - N_{\downarrow}}{\tau_{\uparrow\downarrow}} \end{aligned} \tag{C.3}$$

Equation C.3 correlates the terminal spin-flip current with the spin-carrier density in the channel.

C.2 Time Dependent Spin Diffusion Equation

We again start with Eqn. C.1 as,

$$\frac{1}{e}\left[\left(\nabla_t + \hat{y}\frac{\partial}{\partial y}\right).\mathbf{J}_\uparrow\right] = \frac{\partial n_\uparrow}{\partial t} + \frac{n_\uparrow - n_\downarrow}{\tau_{\uparrow\downarrow}} \tag{C.4}$$

Integrating with respect to y, we get,

$$\frac{h}{e}\left[\nabla_t.\mathbf{J}_\uparrow\right] + \frac{1}{e}\left[J_{\uparrow,y}(y=h) - J_{\uparrow,y}(y=0)\right] = h\left[\frac{\partial n_\uparrow}{\partial t} + \frac{n_\uparrow - n_\downarrow}{\tau_{\uparrow\downarrow}}\right] \tag{C.5}$$

Since there is no current injection/extraction at $y = h$, we have,

$$\frac{1}{e}\left[\nabla_t.\mathbf{J}_\uparrow\right] = \left[\frac{\partial n_\uparrow}{\partial t} + \frac{n_\uparrow - n_\downarrow}{\tau_{\uparrow\downarrow}}\right] + \frac{1}{he}\left[J_{\uparrow,y}(y=0)\right] \tag{C.6}$$

We assume that the spin-current is continuous at $y = 0$ for low temperatures. Hence we have,

$$J_{\uparrow,y}(y=0) = \frac{G_\uparrow}{e}\left(\mu_\uparrow - eV\right) \tag{C.7}$$

where $G_\uparrow$ is the spin-up tunnel conductance, $\mu_\uparrow$ is the electrochemical potential for the spin-up electrons, and V is the applied voltage. Hence, Eqn. C.6 simplifies to,

$$\frac{1}{e}\left[\nabla_t.\mathbf{J}_\uparrow\right] = \left[\frac{\partial n_\uparrow}{\partial t} + \frac{n_\uparrow - n_\downarrow}{\tau_{\uparrow\downarrow}}\right] + \frac{G_\uparrow}{e^2 h}\left(\mu_\uparrow - eV\right) \tag{C.8}$$

We know that the current density for spin-up electrons is given by,

$$\begin{aligned}\mathbf{J}_\uparrow &= \sigma_\uparrow\mathbf{E} + eD\nabla n_\uparrow \\ \frac{1}{e}\nabla_t.\mathbf{J}_\uparrow &= \frac{1}{e}\left[\sigma_\uparrow\left(\nabla_t.\mathbf{E}\right) + \left(\nabla_t\sigma_\uparrow\right).\mathbf{E}\right] + D\nabla_t^2 n_\uparrow\end{aligned} \tag{C.9}$$

where μ is the effective mobility and D is the effective diffusion coefficient. Hence Eqn. C.8 simplifies to,

$$\frac{1}{e}\left[\sigma_\uparrow\left(\nabla_t.\mathbf{E}\right) + \left(\nabla_t\sigma_\uparrow\right).\mathbf{E}\right] + D\nabla_t^2 n_\uparrow = \frac{\partial n_\uparrow}{\partial t} + \frac{n_\uparrow - n_\downarrow}{\tau_{\uparrow\downarrow}} + \frac{G_\uparrow}{e^2 h}\left(\mu_\uparrow - eV\right) \tag{C.10}$$

The small contribution from electric field is neglected as drift is negligible due to high doping in the channel. Thus Eqn. C.10 simplifies to,

$$D\nabla_t^2 n_\uparrow = \left[\frac{\partial n_\uparrow}{\partial t} + \frac{n_\uparrow - n_\downarrow}{\tau_{\uparrow\downarrow}}\right] + \frac{G_\uparrow}{e^2 h}(\mu_\uparrow - eV) \tag{C.11}$$

Since $n_\uparrow$ and $n_\downarrow$ are approximately uniform along the z- direction, $\nabla_t^2 \approx \partial^2/\partial x^2$. Hence Eqn. C.11 is simplified as,

$$D\frac{\partial^2 n_\uparrow}{\partial x^2} = \left[\frac{\partial n_\uparrow}{\partial t} + \frac{n_\uparrow - n_\downarrow}{\tau_{\uparrow\downarrow}}\right] + \frac{G_\uparrow}{e^2 h}(\mu_\uparrow - eV) \tag{C.12}$$

C.3 Relation between Carrier Density and Fermi Level

The spin-up electron density ($n_\uparrow$) is related to the electrochemical potential ($\mu_\uparrow$) in a degenerate semiconductor as,

$$n_\uparrow = \int_0^\infty N_\uparrow(\epsilon)F(\epsilon)d\epsilon \tag{C.13}$$

where $N_\uparrow$ is the spin-up electron density-of-states and F is the Fermi-Dirac distribution, given by $F(\epsilon) = 1/[1 + \exp(\epsilon - \mu_\uparrow)]$. Figure C.1 shows the variation of $n_\uparrow$ as a

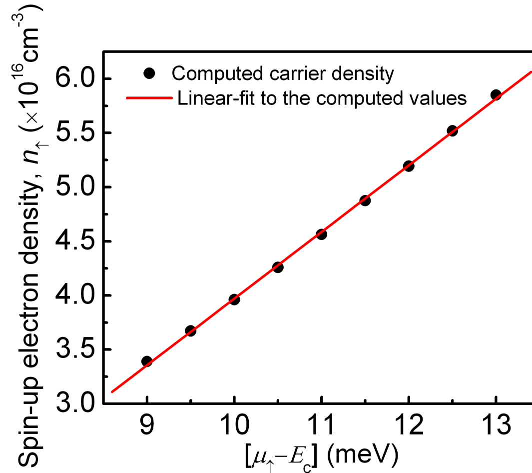

Figure C.1: Variation of $n_\uparrow$ as a function of $(\mu_\uparrow - E_c)$ determined from Eqn. C.13, where E_c is the conduction band edge. The solid line depicts a least-square linear fit to the calculated values.

function of $\mu_\uparrow$. It can be seen that the dependency is approximately linear over the

operating range for electron spin-polarization in the channel, $+30\% \leq \Pi_c \leq -30\%$. Hence, Eqn. C.13 can be approximated by Taylor series expansion (around $n_\uparrow = n_0/2$) and keeping only the linear term as,

$$n_\uparrow = \frac{n_0}{2} + (\mu_\uparrow - \mu_0)\left[\frac{\partial n_\uparrow}{\partial \mu_\uparrow}\right]_{n_\uparrow = n_0/2, \mu_\uparrow = \mu_0} \tag{C.14}$$

APPENDIX D

Modeling of Polarization Modulation

D.1 Definition of Laser Parameters

The laser parameters in Chap. VII are reproduced here:

1. Differential Gain - dg/dn
2. Radiative recombination rate - B_{sp}
3. Auger recombination rate - C
4. Carrier capture time - τ_{cap}
5. Spin-flip time in barrier - $\tau_{s,b}$
6. Spin-flip time in QD - τ_s
7. Photon group velocity - v_g
8. Optical confinement factor - Γ
9. Spontaneous emission factor - β
10. Photon lifetime - τ_{ph}
11. Volume of barrier - V_b
12. Volume of active region - V_{QD}
13. Threshold carrier density - n_{th}

14. Transparency carrier density - n_{tr}

15. Ferromagnetic contact polarization - $P_{contact}$

16. Spin diffusion length in AlGaAs - λ_{sf}

D.2 Coupled Laser Rate Equations

The coupled rate equations governing the dynamics of carrier and photon densities are given by (Chap. VII),

$$\frac{\partial n_b^{\pm}}{\partial t} = -\frac{n_b^{\pm}}{\tau_{cap}} + \frac{1 \pm P_{spin}}{2}\frac{I_{pump}}{qV_b} \mp \frac{n_b^{+} - n_b^{-}}{\tau_{s,b}} = 0 \quad \text{(D.1)}$$

$$\frac{\partial n^{\pm}}{\partial t} = \frac{V_b}{V_{QD}}\frac{n_b^{\pm}}{\tau_{cap}} - v_g g(n^{\pm}, S^{\pm})S^{\mp} \mp \frac{n^{+} - n^{-}}{\tau_s} - B_{sp}n^{\pm}(n^{+} + n^{-}) - Cn^{\pm}(n^{+} + n^{-})^2 = 0 \quad \text{(D.2)}$$

$$\frac{\partial S^{\pm}}{\partial t} = \Gamma v_g g(n^{\mp}, S^{\pm})S^{\pm} + \Gamma\beta B_{sp}n^{\mp}(n^{+} + n^{-}) - \frac{S^{\pm}}{\tau_{ph}} = 0 \quad \text{(D.3)}$$

All the equations are equated to zero to determine the final values of the laser output parameters.

D.3 Transport of Spin-Polarized Carriers in a Laser

The spin transport from ferromagnetic contact to the barrier region is diffusive in nature. The spin polarization at a distance x from the contact is governed by,

$$\frac{\partial^2(N^{+} - N^{-})}{\partial x^2} = \frac{N^{+} - N^{-}}{\lambda_{sf}^2} \quad \text{(D.4)}$$

It is to be noted $N^{+}(x)$ and $N^{-}(x)$ are functions of x (position dependent). These functions are valid from ferromagnetic contact up to the barrier region, *i.e.* $x = x_1$. For $x > x_1$, it is governed by the laser parameters. Also we know,

$$P_{contact} = \Pi(x = 0) = \frac{N^{+}(x = 0) - N^{-}(x = 0)}{N^{+}(x = 0) + N^{-}(x = 0)} \quad \text{(D.5)}$$

$P_{contact}$ is an external input parameter to the laser rate equations, which depends on the magnetic field H. We experimentally know the value of $P_{contact}$ for each and every value of H from the measured out of plane magnetization of MnAs.

D.4 Definition of Spin Polarization

We define the following parameters,

1. QD spin polarization,

$$\Pi_s = \frac{n^+ - n^-}{n^+ + n^-} \tag{D.6}$$

2. Carrier spin polarization at any point $0 \leq x \leq x_1$,

$$\Pi(x) = \frac{N^+(x) - N^-(x)}{N^+(x) + N^-(x)} \tag{D.7}$$

3. Average barrier spin polarization,

$$\Pi_{s,b} = \frac{n_b^+ - n_b^-}{n_b^+ + n_b^-} \tag{D.8}$$

4. It is to be noted that the P_{spin} is not an independent term. It is related to $\Pi_{s,b}$ as obtained from laser Eqns. D.1-D.3,

$$P_{spin} = \Pi_{s,b}\frac{\tau_{cap}}{\tau} = \Pi(x_1) = \frac{N^+(x_1) - N^-(x_1)}{N^+(x_1) + N^-(x_1)} \tag{D.9}$$

where $1/\tau = 1/\tau_{cap} + 2/\tau_{s,b}$.

It is to be noted that all of the above parameters are neither external input to the laser nor external output from the laser. These are all interim parameters and not visible to the external world.

The degree of output circular polarization is given by,

$$\Pi_c = \frac{S^+ - S^-}{S^+ + S^-} \tag{D.10}$$

It is to be noted that Π_c in a measurable external output quantity from the laser. The other measurable external output quantity from the laser is the light output, $L = S^+ + S^-$.

D.5 Operation of a Spin Laser

The spin-laser operation can be described in terms of external inputs, interim parameters and external outputs as:

$$\text{(Input) } P_{contact}, I_{pump} \Longrightarrow P_{spin} \Longrightarrow \Pi_{s,b} \Longrightarrow \Pi_s \Longrightarrow \Pi_c, L \text{ (Output)}$$

D.6 Barrier Spin Polarization and QD Spin Polarization

Here we are going to derive $\Pi_{s,b}$ and Π_c in terms of known laser parameters. Solving Eqn. D.4 we get,

$$\Pi = A \exp(x/\lambda_{sf}) + B \exp(-x/\lambda_{sf}) \tag{D.11}$$

Using the conditions that, $\Pi(x = 0) = P_{contact}$, $\Pi(x = x_1) = P_{spin}$ and $\partial\Pi(x)/\partial(x)$ is continuous at $x = x_1$ we get,

$$\begin{aligned} P_{contact} &= \frac{1}{2}\left[P_{spin} + \lambda_{sf}\frac{\Pi_s - P_{spin}}{x_2 - x_1}\right]\exp(-x_1/\lambda_{sf}) \\ &\quad + \frac{1}{2}\left[P_{spin} - \lambda_{sf}\frac{\Pi_s - P_{spin}}{x_2 - x_1}\right]\exp(x_1/\lambda_{sf}) \\ &= P_{spin}\cosh(x_1/\lambda_{sf}) - \lambda_{sf}\left(\frac{\Pi_s - P_{spin}}{x_2 - x_1}\right)\sinh(x_1/\lambda_{sf}) \end{aligned} \tag{D.12}$$

The above equation gives us a relation between $\Pi_{s,b}$ and Π_s in terms of transport parameters only. We need another relation between $\Pi_{s,b}$ and Π_s in terms of laser parameters to solve them independently. The above equation comes from the transport which correlates $\Pi_{s,b}$ and Π_s. They are also correlated through laser operation which we will use to find another relation.

Adding and subtracting Eqn. D.1 we get,

$$n_b = \frac{I_{pump}\tau_{cap}}{qV_b} \tag{D.13}$$

$$n_b^+ - n_b^- = \frac{I_{pump}P_{spin}\tau}{qV_b} \tag{D.14}$$

Adding and subtracting Eqn. D.2 we get,

$$\frac{V_b}{V_{QD}}\frac{n_b}{\tau_{cap}} = v_g\left[g(n^+,S^-)S^- + g(n^-,S^+)S^+\right] + B_{sp}n^2 + Cn^3 \tag{D.15}$$

$$\begin{aligned}\frac{V_b}{V_{QD}}\frac{n_b^+ - n_b^-}{\tau_{cap}} &= v_g\left[g(n^+,S^-)S^- - g(n^-,S^+)S^+\right] \\ &\quad +(n^+ - n^-)\left(B_{sp}n + Cn^2 + \frac{2}{\tau_s}\right)\end{aligned} \tag{D.16}$$

Adding and subtracting Eqn. D.3 we get,

$$v_g\left[g(n^+,S^-)S^- + g(n^-,S^+)S^+\right] = \frac{S}{\Gamma\tau_{ph}} - \beta B_{sp}n^2 \tag{D.17}$$

$$v_g\left[g(n^+,S^-)S^- - g(n^-,S^+)S^+\right] = -\frac{S^+ - S^-}{\Gamma\tau_{ph}} - \beta B_{sp}n(n^+ - n^-) \tag{D.18}$$

Substituting from Eqns. D.13-D.16 into Eqns. D.17 and D.18 we get,

$$\begin{aligned}\frac{I_{pump}P_{spin}}{qV_{QD}}\frac{\tau}{\tau_{cap}} &= -\frac{S^+ - S^-}{\Gamma\tau_{ph}} + (1-\beta)B_{sp}n(n^+ - n^-) + Cn^2(n^+ - n^-) \\ &\quad +\frac{2}{\tau_s}(n^+ - n^-)\end{aligned} \tag{D.19}$$

$$\frac{I_{pump}}{qV_{QD}} = \frac{S^+ + S^-}{\Gamma\tau_{ph}} + (1-\beta)B_{sp}n(n^+ + n^-) + Cn^2(n^+ + n^-) \tag{D.20}$$

$$-\frac{S^+ - S^-}{S^+ + S^-} = \frac{\frac{I_{pump}P_{spin}}{qV_{QD}}\frac{\tau}{\tau_{cap}} - (n^+ - n^-)\left[(1-\beta)B_{sp}n - Cn^2 - \frac{2}{\tau_s}\right]}{\frac{I_{pump}}{qV_{QD}} - (1-\beta)B_{sp}n(n^+ + n^-) - Cn^2(n^+ + n^-)} \tag{D.21}$$

Let us assume,

$$K = \frac{I_{pump}}{qV_{QD}} \tag{D.22}$$

$$a = (1-\beta)B_{sp}n(n^+ + n^-) + Cn^2(n^+ + n^-) \tag{D.23}$$

Hence Eqn. D.21 becomes,

$$\begin{aligned} -\Pi_c &= \frac{K\Pi_{s,b} - \left(a + \frac{2n}{\tau_s}\right)\Pi_s}{K - a} \\ &= \frac{\Pi_{s,b}\left[1 - \left(a + \frac{2n}{\tau_s}\right)\frac{1}{K}\frac{\Pi_s}{\Pi_{s,b}}\right]}{\left(1 - \frac{a}{K}\right)} \end{aligned} \quad (D.24)$$

We have derived earlier that,

$$-\Pi_c = \Pi_s \frac{1 + \Gamma v_g \tau_{ph}\frac{dg}{dn}n_{tr}}{1 + \Gamma v_g \tau_{ph}\frac{dg}{dn}n_{tr} - \Gamma v_g \tau_{ph}\frac{dg}{dn}n_{th}(1 - \Pi_s)} \quad (D.25)$$

Combining Eqns. D.24 and D.25 we get another relation between $\Pi_{s,b}$ and Π_s as,

$$\frac{\Pi_s(1 + \Gamma v_g \tau_{ph}\frac{dg}{dn}n_{tr})}{1 + \Gamma v_g \tau_{ph}\frac{dg}{dn}n_{tr} - \Gamma v_g \tau_{ph}\frac{dg}{dn}n_{th}(1 - \Pi_s)} = \frac{\Pi_{s,b}\left[1 - \left(a + \frac{2n}{\tau_s}\right)\frac{1}{K}\frac{\Pi_s}{\Pi_{s,b}}\right]}{\left(1 - \frac{a}{K}\right)} \quad (D.26)$$

Hence, solving Eqns. D.12 and D.26 we get $\Pi_{s,b}$ and Π_s in terms of laser parameters. It is to be noted that both $\Pi_{s,b}(H, I_{pump})$ and $\Pi_s(H, I_{pump})$ are functions of both $P_{contact}$ (hence, H) and I_{pump}. Both quantum dot spin polarization and barrier polarization are going to change for varying magnetic field and pump current.

During actual operation of the laser, Π_s is much smaller than unity. Hence we can write, $(1 + \Pi_s)^{-1} \approx 1 - \Pi_s$, $(1 + \Pi_s)^{-2} \approx 1 - 2\Pi_s$, and $(1 + \Pi_s)^{-3} \approx 1 - 3\Pi_s$. With these, Eqn. D.26 simplifies to,

$$\begin{aligned} \frac{\Pi_{s,b}}{\Pi_s} &= K_1 + \frac{1 - K_1}{K}\left[(1 - \beta)B_{sp}n_{th}^2 + Cn_{th}^3\right] + \frac{2n_{th}}{\tau_s K} \\ &\quad - \frac{\Pi_s}{K}\left[2(1 - K_1)(1 - \beta)B_{sp}n_{th}^2 + 3Cn_{th}^3(1 - K_1) + \frac{2n_{th}}{\tau_s}\right] \quad (D.27) \\ &= K_1 + \frac{1}{K}\left(K_2 - \Pi_s K_3\right) \quad (D.28) \end{aligned}$$

where,

$$K_1 \approx \frac{1 + \Gamma v_g \tau_{ph}\frac{dg}{dn}n_{tr}}{1 - \Gamma v_g \tau_{ph}\frac{dg}{dn}n_{th}} \quad (D.29)$$

$$K_2 = (1 - K_1)\left[(1 - \beta)B_{sp}n_{th}^2 + Cn_{th}^3\right] + \frac{2n_{th}}{\tau_s} \quad (D.30)$$

$$K_3 = \left[2(1 - K_1)(1 - \beta)B_{sp}n_{th}^2 + 3Cn_{th}^3(1 - K_1) + \frac{2n_{th}}{\tau_s}\right] \quad (D.31)$$

Assuming,

$$b_1 = \frac{\lambda_{sf}}{x_2 - x_1} \tag{D.32}$$

$$b_2 = \frac{\tau_{cap}}{\tau}\left[\cosh(x_1/\lambda_{sf}) + b_1 \sinh(x_1/\lambda_{sf})\right] \tag{D.33}$$

$$b_3 = b_1 \sinh(x_1/\lambda_{sf}) \tag{D.34}$$

Equation D.12 becomes,

$$P_{contact} = b_2\Pi_{s,b} - b_3\Pi_s \tag{D.35}$$

Combining Eqns. D.28 and D.35 we get the following quadratic expression for Π_s,

$$\Pi_s^2\left(\frac{b_2K_3}{K}\right) + \Pi_s\left(b_2K_1 - b_3 - \frac{b_2K_2}{K}\right) - P_{contact} = 0 \tag{D.36}$$

The above equation is solved to determine $\Pi_s(H, I_{pump})$. Once Π_s is known $\Pi_{s,b}$ is determined using Eqn. D.35.

It is to be noted that we have assumed an approximate expression for K_1. Using the exact expression will yield a cubic equation for Π_s. However, the error made is very small in the above case.

D.7 Threshold Current without Magnetic Field

From Eqn. D.3 we have,

$$S_{th} = \frac{\Gamma\beta B n_{th}^2}{1/\tau_{ph} - \Gamma v_g \frac{dg}{dn}(n_{th} - n_{tr})} \tag{D.37}$$

Hence, threshold current is obtained from Eqn. D.20 as

$$I_{th,0} = qV_{QD}\left[\frac{1}{\Gamma}\frac{S_{th}}{\tau_{ph}} + Bn_{th}^2(1-\beta) + Cn_{th}^3\right] \tag{D.38}$$

D.8 Threshold Current with Magnetic Field

We know $P_{contact}$ at a given magnetic field H. Hence using section D.6 we know $\Pi_s(I_{th})$ at that magnetic field. Hence, we have one equation relating Π_s with I_{th}. We also have from Eqn D.20,

$$I_{th}(H) = qV_{QD}\left[\frac{1}{\Gamma}\frac{S_{th}}{\tau_{ph}} + \frac{Bn_{th}^2(1-\beta)}{(1+\Pi_s)^2} + \frac{Cn_{th}^3}{(1+\Pi_s)^3}\right] \quad (D.39)$$

The above equation gives another relation between $I_{th}(H)$ and $\Pi_s(H)$. Hence, solving two equations we get $I_{th}(H)$.

D.9 Output Circular Polarization

Using section D.6, we know $\Pi_s(H, I_{pump})$ at a given H and I_{pump}. Hence Π_c is obtained from Eqn. D.25 as,

$$\Pi_c(H, I_{pump}) = -\Pi_s \frac{1+\Gamma v_g \tau_{ph}\frac{dg}{dn}n_{tr}}{1+\Gamma v_g \tau_{ph}\frac{dg}{dn}n_{tr} - \Gamma v_g \tau_{ph}\frac{dg}{dn}n_{th}(1-\Pi_s)} \quad (D.40)$$

D.10 Amplification of Spin Polarization

From Eqn. D.24 we have,

$$-\Pi_c = \Pi_{s,b}\left[1-\left(a+\frac{2n}{\tau_s}\right)\frac{1}{K}\frac{\Pi_s}{\Pi_{s,b}}\right]\Big/\left(1-\frac{a}{K}\right) \quad (D.41)$$

If spin relaxation τ_s is neglected we have,

$$-\Pi_c = \frac{K\Pi_{s,b} - a\Pi_s}{K-a} \quad (D.42)$$

$$= \Pi_{s,b}\left(1-\frac{a}{K}\frac{\Pi_s}{\Pi_{s,b}}\right)\Big/\left(1-\frac{a}{K}\right) \quad (D.43)$$

From Eqn. D.20 we know that, $a/K < 1$. Also, from the operation of the laser we know, $\Pi_s/\Pi_{s,b} \leq 1$ (for both positive and negative $\Pi_{s,b}$). Hence Eqn. D.43 leads to,

$$|\Pi_c| \geq |\Pi_{s,b}| \quad (D.44)$$

If $\tau_{s,b}$ is neglected with respect to τ_{cap} we have,

$$|\Pi_c| \geq |P_{spin}| \tag{D.45}$$

APPENDIX E

Fabrication Steps for MOEIC

The heterostructure for MOEIC in Fig. 8.2 is redrawn in Fig. E.1. Each epitaxial layer is sequentially numbered from the top for easy reference. The fabrication of the MOEIC is done in the following sequential steps:

1. Alignment layer

   - A thin film of Ti/Au (10/20 nm) is deposited and patterned using photolithography, PVD and lift-off techniques. Figure E.2(a) shows a micro-photograph of the alignment mark layer. All the remaining layers for photolithography are aligned with respect to this layer.

2. Fabrication of the spin-valve

   - Mesa formation for spin-valve by etching away the MnAs (1), n^+-GaAs (2), n-GaAs (3) layers and 100 nm of the first GaAs buffer layer (4) by using $H_3PO_4/H_2O_2/H_2O$ solution (Fig. E.2(b)). The layer numbers are shown in the parenthesis.

   - Formation of the analyzer and polarizer contacts by etching away the MnAs (1) and heavily doped n^+- GaAs (2) layers from the spin-valve mesa by dry etching (Cl_2 and Ar gas mixture). Figures E.2(c) and (d) show light-image and dark-image micro-photographs of the source and drain contacts.

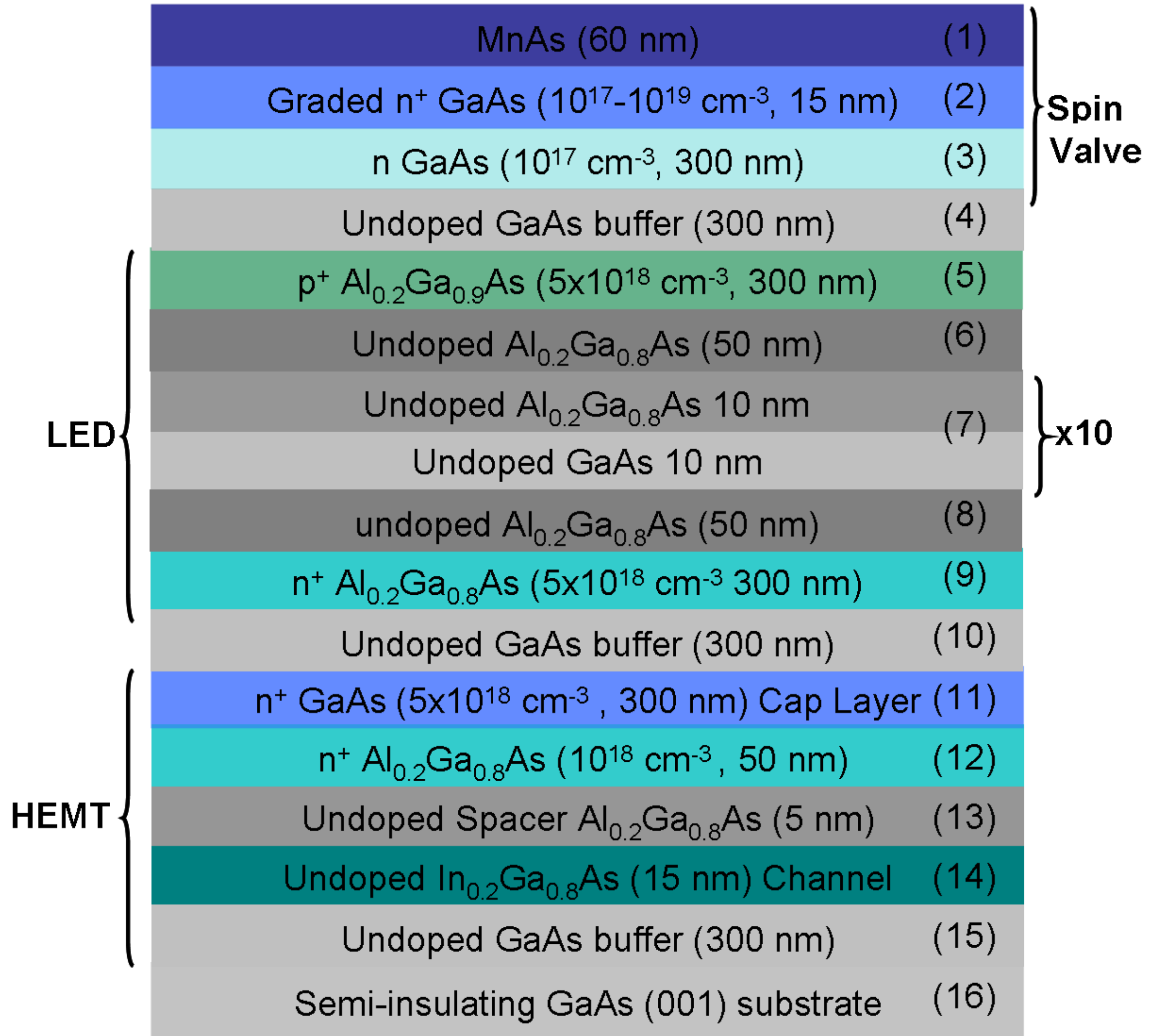

Figure E.1: A schematic of the MOEIC heterostructure grown by MBE. Each epitaxial layer is labelled with a number from the top.

3. Fabrication of the resistor R_1

   - A thin film of Ti is deposited on the first GaAs buffer layer (4) and patterned using photolithography and lift-off technique (Fig. E.2(e)). The nominal resistance of R_1 is designed to be 175 Ω.

4. Fabrication of the LED

   - Mesa formation for LED by etching away remaining 200 nm of the first GaAs buffer layer (4), and the p^+- $Al_{0.2}Ga_{0.8}As$ (5), undoped $Al_{0.2}Ga_{0.8}As$ (6), un-

doped GaAs/ $Al_{0.2}Ga_{0.8}As$ multi-quantum-well (7), undoped $Al_{0.2}Ga_{0.8}As$ (8) and 100 nm of n^+- $Al_{0.2}Ga_{0.8}As$ (9) layers (Figs. E.2(f) and (g)). The spin-valve and resistor R_1 are protected by photoresist.

- An annular LED p-contact (Pd/Zn/Pd/Au) is formed on top of the LED mesa (5) by photolithography, etching, metal deposition and lift-off techniques (Fig. E.2(h)).
- An annular LED n-contact (Pd/Zn/Pd/Au) is formed at the bottom of the LED mesa by photolithography, metal deposition and lift-off techniques (Fig. E.2(i)).

5. Fabrication of the HEMT

- Mesa formation for HEMT by etching away the remaining 200 nm of n^+-$Al_{0.2}Ga_{0.8}As$ layer (9), and the second undoped GaAs buffer (10), n^+ GaAs cap (11), n^+ $Al_{0,2}Ga_{0.2}As$ (12), undoped $Al_{0,2}Ga_{0.2}As$ spacer (13), undoped $In_{0,2}Ga_{0.2}As$ channel (14), and 100 nm of bottom undoped GaAs buffer (15) layers (Figs. E.2(j) and (k)). The spin-valve, resistance R_1 and LED are protected by photoresist.
- HEMT source and drain ohmic contacts (Ni/Ge/Au/Ti/Au) are formed on n^+-GaAs cap layer (11) by photolithography, etching, metal deposition, lift-off and annealing techniques (Figs. E.2(l) and (m)).
- HEMT gate contact (Ti/Pt/Au) is formed on n^+-$Al_{0.2}Ga_{0.2}As$ layer (12) after gate recess etching (citric acid/H_2O_2/H_2O) through SiO_2, which is deposited by low-temperature PECVD, patterned using photolithography and dry etching (Figs. E.2(n) and (o)).

6. Fabrication of the resistor R_2

- A thin film of Ti is deposited on the bottom undoped GaAs buffer layer (15) and patterned using photolithography and lift-off technique (Fig. E.2(p)). A magnified view of the resistor is shown in Fig. E.2(q). The nominal resistance of R_2 is designed to be 1 kΩ.

7. Interconnect and metallization

   - An SiO_2 layer is deposited by low temperature PECVD for surface passivation. Vias are formed by dry etching and Ti/Au is deposited for interconnect and contact metallization (Figs. E.2(r)–(t)).

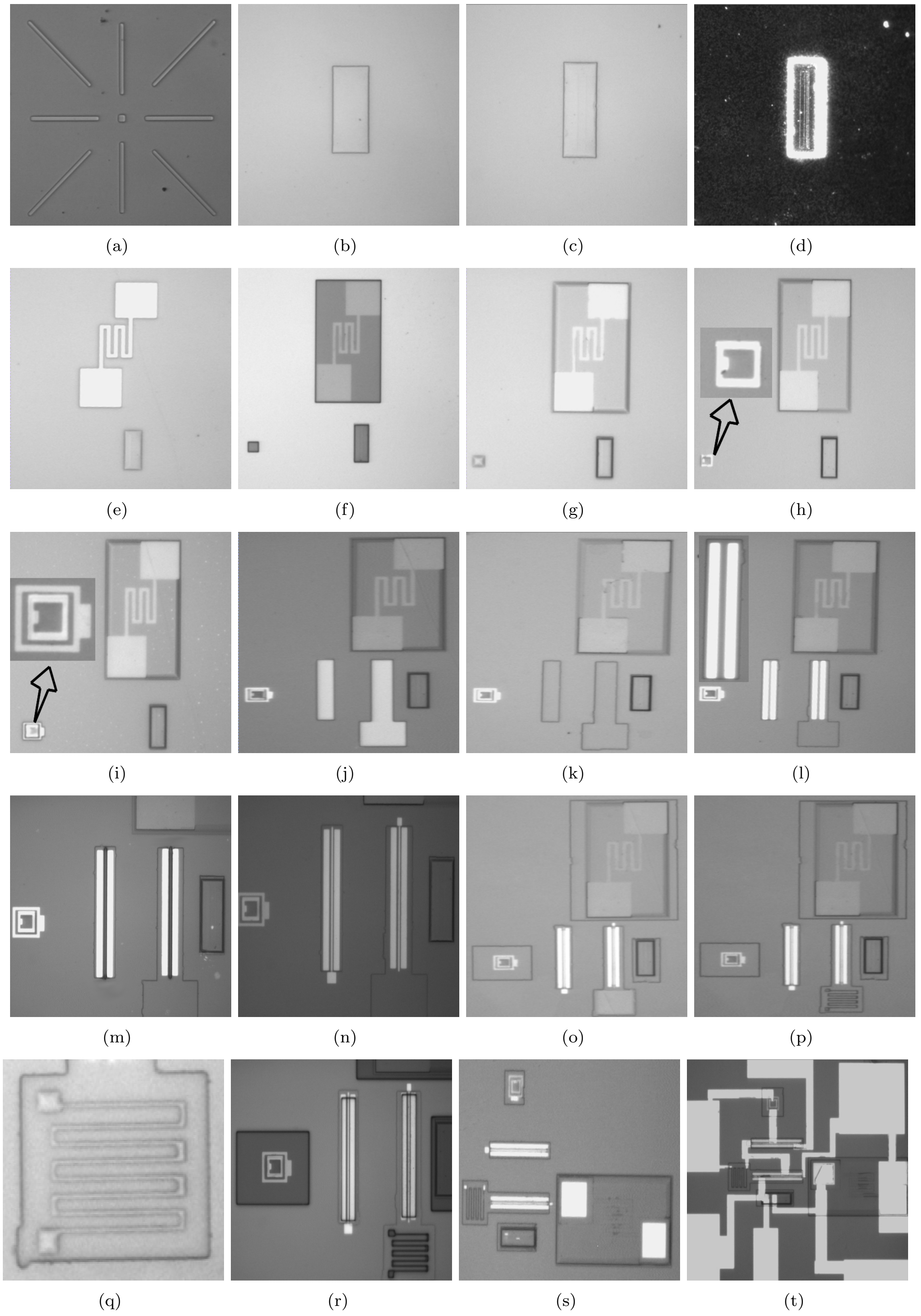

Figure E.2: Micro-photographs of the MOEIC after each fabrication step.

BIBLIOGRAPHY

BIBLIOGRAPHY

[1] G. E. Moore, *Electronics* **38**(8) (1965).

[2] http://www.itrs.net/reports.html (2007).

[3] C. Cohen-Tannoudji, B. Diu, and F. Laloë, *Quantum Mechanics* (Hermann and John Wiley & Sons Inc., 1977).

[4] P. M. Tedrow and R. Meservey, *Phys. Rev. Lett.* **26**, 192 (1971).

[5] M. Julliere, *Phys. Lett.* **54**, 225 (1975).

[6] J. S. Moodera, J. Nowak, and R. J. M. van de Veerdonk, *Phys. Rev. Lett.* **80**, 2941 (1998).

[7] M. N. Baibich, J. M. Broto, A. Fert, F. N. Van Dau, F. Petroff, P. Etienne, G. Creuzet, A. Friederich, and J. Chazelas, *Phys. Rev. Lett.* **61**, 2472 (1988).

[8] W. P. Pratt, S.-F. Lee, J. M. Slaughter, R. Loloee, P. A. Schroeder, and J. Bass, *Phys. Rev. Lett.* **66**, 3060 (1991).

[9] L. Berger, *Phys. Rev. B* **54**, 9353 (1996).

[10] J. C. Slonczewski, *J. Magn. Magn. Mater.* **19**, L1 (1996).

[11] J. A. Katine, F. J. Albert, R. A. Buhrman, E. B. Myers, and D. C. Ralph, *Phys. Rev. Lett.* **84**, 3149 (2000).

[12] J. Z. Sun, D. J. Monsma, D. W. Abraham, M. J. Rooks, and R. H. Koch, *Appl. Phys. Lett.* **81**, 2202 (2002).

[13] A. G. Aronov, *JEPT Lett.* **24**, 32 (1976).

[14] M. Johnson and R. H. Silsbee, *Phys. Rev. Lett.* **55**, 1790 (1985).

[15] F. J. Jedema, H. B. Heersche, A. T. Filip, J. J. A. Baselmans, , and B. J. van Wees, *Nature* **416**, 713 (2002).

[16] J. M. Kikkawa and D. D. Awschalom, *Phys. Rev. Lett.* **80**, 4313 (1998).

[17] G. Schmidt, D. Ferrand, L. W. Molenkamp, A. T. Filip, and B. J. van Wees, *Phys. Rev. B* **62**, R4790 (2000).

[18] E. I. Rashba, *Phys. Rev. B* **62**, R16267 (2000).

[19] D. Saha, M. Holub, P. Bhattacharya, and Y. C. Liao, *Appl. Phys. Lett.* **89**, 142504 (2006).

[20] X. Lou, C. Adelmann, S. A. Crooker, E. S. Garlid, J. Zhang, K. S. M. Reddy, S. D. Flexner, C. J. Palmstrom, and P. A. Crowell, *Nature Phys.* **3**, 197 (2007).

[21] A. T. Hanbicki, O. M. J. van 't Erve, R. Magno, G. Kioseoglou, C. H. Li, B. T. Jonker, G. Itskos, R. Mallory, M. Yasar, and A. Petrou, *Appl. Phys. Lett.* **82**, 4092 (2003).

[22] F. J. Jedema, A. T. Filip, and B. J. van Wees, *Nature* **410**, 345 (2001).

[23] H. Ohno, *Science* **281**, 951 (1998).

[24] D. J. Monsma, J. C. Lodder, T. J. A. Popma, and B. Dieny, *Phys. Rev. Lett.* **74**, 5260 (1995).

[25] I. Appelbaum, B. Huang, and D. J. Monsma, *Nature* **447**, 295 (2007).

[26] D. D. Awschalom and M. E. Flatté, *Nature Phys.* **3**, 153 (2007).

[27] F. J. Jedema, *Electrical Spin Injection in Metallic Mesoscopic Spin Valves* (Ph.D thesis, University of Groningen, 2002).

[28] X. Jiang, R. Wang, R. M. Shelby, R. M. Macfarlane, S. R. Bank, J. S. Harris, and S. S. P. Parkin, *Phys. Rev. Lett.* **94**, 056601 (2005).

[29] G. Salis, R. Wang, X. Jiang, R. M. Shelby, S. S. P. Parkin, S. R. Bank, and J. S. Harris, *Appl. Phys. Lett.* **87**, 262503 (2005).

[30] A. T. Hanbicki, B. T. Jonker, G. Itskos, G. Kioseoglou, and A. Petrou, *Appl. Phys. Lett.* **80**, 1240 (2002).

[31] C. H. Li, G. Kioseoglou, O. M. J. van 't Erve, M. E. Ware, D. Gammon, R. M. Stroud, B. T. Jonker, R. Mallory, M. Yasar, and A. Petrou, *Appl. Phys. Lett.* **86**, 132503 (2005).

[32] G. Itskos, E. Harbord, S. K. Clowes, E. Clarke, L. F. Cohen, R. Murray, P. V. Dorpe, and W. V. Roy, *Appl. Phys. Lett.* **88**, 022113 (2006).

[33] J. Fabian, A. Matos-Abiague, C. Ertler, P. Stano, and I. Žutić, *Acta Phys. Slovaca* **57**, 565 (2007).

[34] R. J. Elliott, *Phys. Rev.* **96**, 266 (1954).

[35] M. I. D'yakonov and V. I. Perel', *Sov. Phys. Solid. State* **13**, 3023 (1971).

[36] G. L. Bir, A. G. Aronov, and G. E. Pikus, *Sov. Phys. JETP* **42**, 705 (1976).

[37] R. I. Dzhioev, K. V. Kavokin, V. L. Korenev, M. V. Lazarev, B. Y. Meltser, M. N. Stepanova, B. P. Zakharchenya, D. Gammon, and D. S. Katzer, *Phys. Rev. B* **66**, 245204 (2002).

[38] M. Holub and P. Bhattacharya, *J. Phys. D: Appl. Phys.* **40**, R179 (2007).

[39] O. M. J. van 't Erve, A. T. Hanbicki, M. Holub, C. H. Li, C. Awo-Affouda, P. E. Thompson, and B. T. Jonker, *Appl. Phys. Lett.* **91**, 212109 (2007).

[40] S. A. Wolf, D. D. Awschalom, R. A. Buhrman, J. M. Daughton, S. von Molnar, M. L. Roukes, A. Y. Chtchelkanova, and D. M. Treger, *Science* **294**, 1488 (2001).

[41] J. S. Moodera, L. R. Kinder, T. M. Wong, and R. Meservey, *Phys. Rev. Lett.* **74**, 3273 (1995).

[42] T. Miyazaki and N. Tezuka, *J. Magn. Magn. Mater.* **139**, L231 (1995).

[43] F. J. Jedema, M. S. Nijboer, A. T. Filip, and B. J. van Wees, *Phys. Rev. B* **67**, 085319 (2003).

[44] T. Kimura, J. Hamrle, Y. Otani, K. Tsukagoshi, and Y. Aoyagi, *J. Magn. Magn. Mater.* **286**, 88 (2005).

[45] P. R. Hammar and M. Johnson, *Phys. Rev. Lett.* **88**, 066806 (2002).

[46] S. Hacia, T. Last, S. F. Fischer, and U. Kunze, *J. Supercond.* **16**, 187 (2003).

[47] J. D. Albrecht and D. L. Smith, *Phys. Rev. B* **68**, 035340 (2003).

[48] M. Tanaka, *Semicond. Sci. and Technol.* **17**, 327 (2002).

[49] M. Tanaka, J. P. Harbison, M. C. Park, Y. S. Park, T. Shin, and G. M. Rothberg, *Appl. Phys. Lett.* **65**, 1964 (1994).

[50] R. P. Panguluri, G. Tsoi, B. Nadgorny, S. H. Chun, N. Samarth, and I. I. Mazin, *Phys. Rev. B* **68**, 201307 (2003).

[51] M. Donahue and D. Porter, http://math.nist.gov/oommf.

[52] B. J. Jonsson-Akerman, R. Escudero, C. Leighton, S. Kim, I. K. Schuller, and D. A. Rabson, *Appl. Phys. Lett.* **77**, 1870 (2000).

[53] W. F. Brinkman, R. C. Dynes, and J. M. Rowell, *J. Appl. Phys.* **41**, 1915 (1970).

[54] S. T. Chui, *IEEE Trans. Magn.* **34**, 1000 (1998).

[55] Z. G. Yu and M. E. Flatté, *Phys. Rev. B* **66**, 235302 (2002).

[56] Y. Y. Wang and M. W. Wu, *Phys. Rev. B* **72**, 153301 (2005).

[57] F. J. Jedema, A. T. Filip, and B. J. van Wees, *Nature* **410**, 345 (2001).

[58] F. J. Jedema, H. B. Heersche, A. T. Filip, Baselmans, J. J. A., and B. J. van Wees, *Nature* **416**, 713 (2002).

[59] M. Holub, J. Shin, D. Saha, and P. Bhattacharya, *Phys. Rev. Lett.* **98**, 146603 (2007).

[60] S. Datta and B. Das, *Appl. Phys. Lett.* **56**, 665 (1990).

[61] W. Long, Q.-F. Sun, H. Guo, and J. Wang, *Appl. Phys. Lett.* **83**, 1397 (2003).

[62] J. Wang, K. S. Chan, and D. Y. Xing, *Phys. Rev. B* **72**, 115311 (2005).

[63] H. Dery, L. Cywinski, and L. J. Sham, *Phys. Rev. B* **73**, 161307 (2006).

[64] S.-W. Jung and H.-W. Lee, *Phys. Rev. B* **73**, 165302 (2006).

[65] C. Benjamin and R. Citro, *Phys. Rev. B* **72**, 085340 (2005).

[66] J. Fabian and I. Žutić, *Phys. Rev. B* **69**, 115314 (2004).

[67] P. C. van Son, H. van Kempen, and P. Wyder, *Phys. Rev. Lett.* **58**, 2271 (1987).

[68] V. Sih, W. H. Lau, R. C. Myers, V. R. Horowitz, A. C. Gossard, and D. D. Awschalom, *Phys. Rev. Lett.* **97**, 096605 (2006).

[69] H. Dery, L. Cywinski, and L. J. Sham, *Phys. Rev. B* **73**, 041306 (2006).

[70] J. Hamrle, T. Kimura, Y. Otani, K. Tsukagoshi, and Y. Aoyagi, *Phys. Rev. B* **71**, 094402 (2005).

[71] D. Saha, M. Holub, and P. Bhattacharya, *Appl. Phys. Lett.* **91**, 072513 (2007).

[72] S. Garzon, I. Žutić, and R. A. Webb, *Phys. Rev. Lett.* **94**, 176601 (2005).

[73] H. Dery and L. J. Sham, *Phys. Rev. Lett.* **98**, 046602 (2007).

[74] R. Godfrey and M. Johnson, *Phys. Rev. Lett.* **96**, 136601 (2006).

[75] I. Žutić, J. Fabian, and S. D. Sarma, *Rev. Mod. Phys.* **76**, 323 (2004).

[76] S. I. Kiselev, J. C. Sankey, I. N. Krivorotov, N. C. Emley, R. J. Schoelkopf, R. A. Buhrman, and D. C. Ralph, *Nature* **425**, 380 (2003).

[77] V. Garcia, H. Jaffrès, J.-M. George, M. Marangolo, M. Eddrief, and V. H. Etgens, *Phys. Rev. Lett.* **97**(24), 246802 (Dec. 2006).

[78] N. Almeleh and B. Goldstein, *Phys. Rev.* **128**, 1568 (1962).

[79] S. Datta, *Appl. Phys. Lett.* **87**, 013115 (2005).

[80] L. Childress, M. V. Gurudev Dutt, J. M. Taylor, A. S. Zibrov, F. Jelezko, J. Wrachtrup, P. R. Hemmer, and M. D. Lukin, *Science* **314**(5797), 281 (2006).

[81] S. Datta, *Proceedings of the International School of Physics "Enrico Fermi", Course CLX* **arXiv:0802.2067** (2005).

[82] G. Salis, D. T. Fuchs, J. M. Kikkawa, D. D. Awschalom, Y. Ohno, and H. Ohno, *Phys. Rev. Lett.* **86**, 2677 (2000).

[83] M. Tanaka, J. P. Harbison, and G. M. Rothberg, *J. Cryst. Growth* **150**, 1132 (1995).

[84] R. Moriya and H. Munekata, *J. Appl. Phys.* **93**, 4603 (2003).

[85] M. Kaminskai, A. Twardowski, and D. Wasik, *J. Mater. Sci.*, DOI: 10.1007/s10854-007-9486-z (2007).

[86] M. Xiao, I. Martin, E. Yablonovitch, and H. W. Jiang, *Nature* **430**, 435 (2004).

[87] S. Hallstein, J. D. Berger, M. Hilpert, H. C. Schneider, W. W. Rühle, F. Jahnke, S. W. Koch, H. M. Gibbs, G. Khitrova, and M. Oestreich, *Phys. Rev. B* **56**, R7076 (1997).

[88] T. Mukaihara, F. Koyama, and K. Iga, *IEEE Photonics Technol. Lett.* **5**, 133 (1993).

[89] H. Ando, T. Sogawa, and H. Gotoh, *Appl. Phys. Lett.* **73**, 566 (1998).

[90] C. Chang-Hasnain, J. Harbison, G. Hasnain, A. V. Lehmen, L. Florez, and N. Stoffel, *IEEE Journal of Quant. Electron.* **27**, 1402 (1991).

[91] T. H. Russell and T. D. Milster, *Appl. Phys. Lett.* **70**, 2520 (1997).

[92] C. J. Chang-Hasnain, J. P. Harbison, G. Hasnain, A. C. V. Lehmen, L. T. Florez, and N. G. Stoffel, *IEEE Journal of Quant. Electronics.* **27**, 1402 (1991).

[93] K. D. Choquette, D. A. Richie, and R. E. Leibenguth, *Appl. Phys. Lett.* **64**, 2062 (1994).

[94] M. Shimuzi, T. Mukaihara, F. Koyama, and K. Iga, *Electron Lett.* **27**, 1067 (1991).

[95] R. W. Martin, R. J. Nicholas, G. J. Rees, S. K. Haywood, N. J. Mason, and P. J. Walker, *Phys. Rev. B* **42**, 9237 (1990).

[96] S. A. Crooker, D. D. Awschalom, J. J. Baumberg, F. Flack, and N. Samarth, *Phys. Rev. B* **56**, 7574 (1997).

[97] J. Rudolph, D. Hägele, H. M. Gibbs, G. Khitrova, and M. Oestreich, *Appl. Phys. Lett.* **82**, 4516 (2003).

[98] J. Rudolph, S. Döhrmann, D. Hägele, M. Oestreich, and W. Stolz, *Appl. Phys. Lett.* **87**, 241117 (2005).

[99] Y. Ohno, R. Terauchi, T. Adachi, F. Matsukura, and H. Ohno, *Physica E* **6**, 817 (2000).

[100] A. Tackeuchi, R. Ohtsubo, K. Yamaguchi, M. Murayama, T. Kitamura, and T. Kuroda, *Appl. Phys. Lett.* **84**, 3576 (2004).

[101] D. V. Kuksenkov, H. Temkin, and S. Swirhun, *Appl. Phys. Lett.* **67**, 2141 (1995).

[102] N. Kirstaedter, O. G. Schmidt, N. N. Ledentsov, D. Bimberg, V. M. Ustinov, A. Y. Egorov, A. E. Zhukov, M. V. Maximov, P. S. Kopév, and Z. I. Alferov, *Appl. Phys. Lett.* **69**, 1226 (1996).

[103] I. Novikov, N. Y. Gordeev, M. Maksimov, Y. Shernyakov, E. Semenova, A.P.Vasil'ev, A. Zhukov, , V. Ustinov, and G. Zegrya, *Semiconductors* **39**, 481 (2005).

[104] L. V. Dao, M. B. Johnston, M. Gal, L. Fu, H. H. Tan, and C. Jagadish, *Appl. Phys. Lett.* **73**, 3408 (1998).

[105] R. Ram, E. Goobar, M. Peters, L. Coldren, and J. Bowers, *IEEE Photonics Technol. Lett.* **8**, 599 (1996).

[106] M.Shimuzi, T. Mukaihara, F. Koyama, and K. Iga, *Electron. Lett.* **27**, 1067 (1991).

[107] I. Sato, R. Yamashima, K. Kadowaki, J. Yamamoto, T. Shibata, , and K. Soai, *Angew. Chem., Int. Ed.* **40**, 1096 (2001).

[108] R. Fiederling, M. Keim, G. Reuscher, W. Ossau, G. Schmidt, A. Waag, and L. W. Molenkamp, *Nature* **402**, 787 (1999).

[109] A. Greilich, D. R. Yakovlev, A. Shabaev, A. L. Efros, I. A. Yugova, R. Oulton, V. Stavarache, D. Reuter, A. Wieck, and M. Bayer, *Science* **313**, 341 (2006).

[110] F. Meier and B. P. Zakharchenya, *Optical Orientation* (Elsevier Science, 1984).

[111] Z. G. Yu and M. E. Flatté, *Phys. Rev. B* **66**, 201202 (2002).

[112] D. Basu, D. Saha, C. C. Wu, M. Holub, Z. Mi, and P. Bhattacharya, *Appl. Phys. Lett.* **92**, 091119 (2008).

[113] S. Ghosh, P. Bhattacharya, E. Stoner, J. Singh, H. Jiang, S. Nuttinck, and J. Laskar, *Appl. Phys. Lett.* **79**, 722 (2001).

[114] D. Saha, L. Siddiqui, P. Bhattacharya, S. Datta, D. Basu, and M. Holub, *Phys. Rev. Lett.* **100**, 196603 (2008).

[115] H. Dery, P. Dalal, L. Cywinski, and L. J. Sham, *Nature* **447**, 573 (2007).

[116] F. Ali and A. Gupta, *HEMTs and HBTs: Devices, Fabrication, and Circuits* (Artech House Publishers, 1991).

[117] P. Bhattacharya, *Semiconductor Optoelectronic Devices* (Prentice Hall, 1996).

[118] J. Lou, R. E. Insignares, Z. Cai, K. S. Ziemer, M. Liu, and N. X. Sun, *Appl. Phys. Lett.* **91**, 182504 (2007).

[119] D. Saha, D. Basu, and P. Bhattacharya, *Appl. Phys. Lett.* (under review, 2008).